

ALMA MATER STUDIORUM - Università di Bologna

DOTTORATO DI RICERCA IN
ASTROFISICA

Ciclo 34

**Probing the innermost regions of AGN via
time-resolved spectral analysis**

Presentata da:
Deborah Costanzo

Supervisore:
Prof. **Cristian Vignali**

Coordinatore di Dottorato:
Prof. **Andrea Miglio**

Co-supervisore:
Dr. **Mauro Dadina**

Esame finale anno 2022

Settore Concorsuale: 02/C1 – ASTRONOMIA, ASTROFISICA, FISICA DELLA TERRA E DEI
PIANETI

Settore Scientifico Disciplinare: FIS/05 – ASTRONOMIA E ASTROFISICA

Hey, look on the bright side:
there's nowhere but up from a
canyon in hell.

Desperate Pleasures
Every Time I Die

Abstract

The dynamics and geometry of the material inflowing and outflowing close to the supermassive black hole (SMBH) in active galactic nuclei (AGN) are still largely uncertain; notably, ejection and accretion processes may be linked to each other. Furthermore, it is fundamental to understand the physical properties, the extent, and energetics of the outflows, as they may also have a fundamental role in AGN feedback processes on the host galaxies, influencing their evolution. The X-ray band is the most suitable to study AGN innermost regions because it includes the Fe K α fluorescence emission line at 6.4 keV, a fundamental proxy of the accretion flows onto the SMBH (Fabian et al., 2000), and possibly Fe resonant absorption lines (~ 7 -12 keV) produced by dense ($N_{\text{H}} \sim 10^{22-24} \text{ cm}^{-2}$) winds with a wide range of velocities (from a few $10^{2-3} \text{ km s}^{-1}$ up to $\sim 0.3c$; Tombesi et al. 2010) and ionization states ($0 \lesssim \log \xi \lesssim 3 \text{ erg cm s}^{-1}$, where $\xi = L/nr^2$ is the ionization parameter). Depending on their physical properties, winds have been typically classified either as Warm Absorbers (slow and mildly ionized, Blustin et al. 2005) or Ultra Fast Outflows (fast and highly ionized, Tombesi et al. 2010). An interesting case that has arisen in recent years is that of the so-called Obscurers (Kaastra et al., 2014), i.e. transient, optically thick winds typically located in the Broad Line Region that produce a strong spectral hardening in the X-rays, lasting from days to months. Both emission and absorption features in the X-ray spectra are observed to vary on time scales spanning from hours to years, probing phenomena at different distances from the SMBH.

In this work, we use time-resolved spectral analysis to simultaneously investigate the accretion flow and the outflows, hence to further characterize them individually and search for possible correlations that could help discovering the launching mechanisms of disk winds, which are not totally clear yet. In particular, we have analyzed a set of some among the X-ray brightest Seyfert 1 galaxies that went through an occultation event observed with XMM-Newton EPIC pn, i.e. the instrument with the largest collecting area in the Fe K energy band. They are NGC 3783 (Mehdipour et al., 2017), NGC 3227 (Mehdipour et al., 2021), NGC 5548 (Kaastra et al., 2014), and NGC 985 (Parker et al., 2014).

The aim of our analysis is to search for possible emission and/or absorption lines in short-duration spectra (~ 10 ks) extracted from the entire observations, in order to explore regions as close as the SMBH as the statistics allows for, and possibly catch transient phenomena happening in the first few gravitational radii around the black hole, that could be evened out in averaged spectra.

The analysis consists of two steps. The first one is running a blind search on the short time-scale spectra extracted in sequence from single pointings. This means that, upon finding a satisfactory model for the continuum emission (typically, a power law and some form of cold absorption) and the ubiquitous Fe $K\alpha$ emission line, we search for significant deviations from this model in the form of Gaussian lines, with either positive or negative normalization. The significance of these individual lines is further assessed via extensive MonteCarlo simulations. Then, we study the distribution in energy of the detections: this allows us to understand their physical origin and determine the frequency at which they appear. In fact, if some detected lines cluster in a specific energy range, we can assume a common origin for them and thus extrapolate a “global” significance, that includes not only the information of the significance of a single line, but also how many times it is detected. After assessing the statistical robustness of the results, the second part of the analysis consists in studying the evolution in time and energy of the detected features using the Residual Map technique. This is an upgrade of the Excess Maps technique that in the past gave many interesting results on variability patterns of emission lines (Iwasawa et al., 2004; De Marco et al., 2009). We visualize simultaneously the positive and negative residuals (i.e. the emission and absorption features) in the time-energy plane, looking for patterns and time intervals of particular interest. We used NGC 3783 as a test case for our analysis, as in the past it had been already studied with an approach similar to ours, and we used this to have a direct comparison and test our methodology. In this source we have been able to ascribe variations in the normalization of the Fe $K\alpha$ to resonant absorption lines at the same energy due to clumps in the obscuring medium, whose presence is detected at $> 3\sigma$ from the blind search, and to determine the dimensions of the clumps. The same procedure – blind search on each time-resolved spectrum and production of residual maps – is applied to the other sources. In NGC 3227 we detected at the $\sim 2\sigma$ significance level an ultra-fast outflow with velocity $\sim 0.2c$ appearing only in the first part of one observation, at the end of a temporary obscuration event. This feature was not detected in the past, when only the averaged spectrum of the whole pointing was analyzed. In NGC 5548 and NGC 985 we did not detect any significant feature, either in the obscured or unobscured phases of each source.

The analysis techniques we adopted not only can be applied to currently available X-ray datasets of bright AGN, but also holds strong potentiality for the future.

In fact, the *X-IFU* instrument on board *Athena* (Barret et al., 2018), with its unprecedented collecting area ($\sim 3 - 6$ times larger than the EPIC-pn at 7 keV), will allow us to have more statistically robust results on bright sources and to sample even shorter time-scales ($\sim 10^2$ s) on them, and to probe the innermost regions of fainter AGN, that are currently precluded.

Contents

1	Active Galactic Nuclei	11
1.1	The AGN Paradigm	11
1.2	AGN Structure	12
1.3	Outflows	16
1.4	Seyfert 1 X-ray spectrum	19
	1.4.1 Emission lines	21
	1.4.2 Absorption	26
1.5	Variability and analysis techniques	27
2	Sample and data reduction	31
2.1	<i>XMM-Newton</i>	32
	2.1.1 The on-board instruments	32
2.2	Sample selection	35
2.3	Data reduction	37
3	NGC 3783	39
3.1	Baseline model	41
	3.1.1 Fe $K\alpha$ line	42
3.2	Blind search	44
3.3	Simulations	46
3.4	Residual Maps	48
	3.4.1 Fe $K\alpha$ line residuals	52
3.5	Residual maps and Excess maps	53
3.6	Results and discussion	55
	3.6.1 Possible Fe $K\alpha$ broadening during O1 and O2	58
	3.6.2 Fe $K\alpha$ modulation in O2	59
4	NGC 3227	63
4.1	Fe $K\alpha$ line	65
4.2	Blind search and simulations	69
4.3	Residual maps	73

5	NGC 5548	77
5.1	Fe $K\alpha$ line	83
5.2	Blind search and simulations	83
5.3	Residual maps	89
6	NGC 985	91
6.1	Fe $K\alpha$ line	94
6.2	Blind search and simulations	94
6.3	Residual maps	98
7	Conclusions	99
7.1	General properties of the sample	100
7.2	Comparison among the individual sources	105
7.3	Future perspectives	108
	Bibliography	123

Chapter 1

Active Galactic Nuclei

About 10% of all galaxies show a large luminosity (up to $L_{\text{bol}} \approx 10^{48}$ erg s $^{-1}$, with typical values of $L_{\text{bol}} \approx 10^{44} - 10^{46}$ erg s $^{-1}$, where the bolometric luminosity L_{bol} represents the luminosity across all the electromagnetic spectrum; [Padovani et al. e.g. 2017](#)) over the whole electromagnetic spectrum, originated from highly energetic phenomena in the central regions. These sources are called Active Galactic Nuclei (AGN). The radiation produced in the nuclear regions of the AGN can exceed significantly that of the entire host galaxy, overcoming all the light from the galaxy stellar component.

1.1 The AGN Paradigm

The most recognized model to explain the large quantity of radiation observed in AGN postulates that the emission is due to material accreting onto a super massive black hole (SMBH) at the center of the galaxy, with a mass typically in the range $10^6 - 10^9 M_{\odot}$ (e.g. [Peterson, 1997](#)).

Accretion onto compact objects is the most efficient mechanism to convert mass into radiation. The conversion has an efficiency η , so the total available energy is $E = \eta M c^2$. The rate by which this energy is radiated is $L = dE/dt = \eta \dot{M} c^2$, where $\dot{M} = dM/dt$ is the mass accretion rate. The potential energy U of a mass m falling from a distance r onto an object of mass M can be converted to radiation at a rate of:

$$L = \frac{dU}{dt} = \frac{GM}{r} \frac{dm}{dt} = \frac{GM\dot{M}}{r} \quad (1.1)$$

Therefore $\eta \propto M/r$, which is a measure of the compactness of the source: the smaller the system, the higher the efficiency. For AGN, $\eta \approx 0.1$ ([Shakura and Sunyaev, 1973](#)).

A simple estimate of the mass of the central object can be made assuming

a completely ionized gas falling with spherical symmetry at a constant rate. To maintain the stability of the system, the outward radiation pressure force must be compensated by the inward gravitational attraction.¹ The module of the radiation force on a single electron, given the Thomson cross-section $\sigma_e = 6.65 \times 10^{-25} \text{ cm}^{-2}$ for the interaction with a photon, is:

$$F_{rad} = \sigma_e \frac{L}{4\pi r^2 c} \quad (1.2)$$

while for the gravitational force we have:

$$F_{grav} = \frac{GMm_p}{r^2} \quad (1.3)$$

The Eddington limit is the maximum luminosity for an accreting object above which the system would interrupt the accretion; for a central object of mass M expressed in solar masses we have:

$$L_{Edd} = \frac{4\pi G c m_p}{\sigma_e} M \approx 1.26 \times 10^{38} \left(\frac{M}{M_\odot} \right) \text{ ergs}^{-1} \quad (1.4)$$

The Eddington limit allows us to calculate the minimum mass to have accretion with a luminosity of the order of $10^{44} \text{ erg s}^{-1}$:

$$M_{Edd} = 8 \times 10^5 L_{44} M_\odot \quad (1.5)$$

Should a typical quasar have a luminosity of $10^{46} \text{ erg s}^{-1}$, the central object should have a mass of $\approx 10^8 M_\odot$. AGN present variability on different time scales, and some show significant flux variations on time scales of days, hours and even minutes. The variability time scale constrains the size of the regions that produce such variations, which can be as small as the Solar System. Such a mass contained in such a limited region indicates that the central object has to be a SMBH.

1.2 AGN Structure

The physical structure of AGN is still not completely determined, but the majority of models predicts a structure consisting, at least, the following components.

- **Accretion Disk**

The spherical symmetry for the infall of gas is a simplistic hypothesis and does not represent properly the reality: the material preserves its angular

¹The radiation force on a proton and the gravitational force on an electron are negligible, due to their different masses: $m_p/m_e \approx 10^3$.

momentum, so it will form an *accretion disk* around the black hole. Viscous forces transfer the angular momentum outward and the flow spirals inward, dissipating part of its gravitational potential energy into kinetic energy and heat. A complete description of the disk structure is hard to model, since it depends on many parameters (e.g. magnetic fields, viscosity, accretion rate, etc.), but it is possible to describe it as geometrically thin and optically thick disk (Shakura and Sunyaev, 1973), therefore the emission can be approximated as blackbody. From the virial theorem, the gravitation potential energy is released at the rate $dU/dt = GM\dot{M}/r$: half of it heats up the disk and half is radiated as luminosity L . Using the Stefan-Boltzmann law, the energy radiated is σT^4 for both sides of the disk, each with an area of πr^2 . Therefore we have:

$$L = \frac{GM\dot{M}}{2r} = 2\pi r^2 \sigma T^4 \quad (1.6)$$

Solving for the temperature at the distance r from the center:

$$T \propto \left(\frac{GM\dot{M}}{4\pi\sigma r^3} \right)^{1/4} \quad (1.7)$$

The temperature is in the range of $10^5 - 10^6$ K, grows towards the center of the disk and so does the emission frequency: for a blackbody we obtain $\nu_{\max} \propto kT/h \propto r^{-3/4}$. The most internal regions around a SMBH of about $10^8 M_\odot$ can reach frequencies in the extreme UV band ($\nu_{\max} \sim 10^{16}$ Hz). Integrating over all radii, we see a sum of blackbody spectra at different temperatures, called *Big Blue Bump*, in the optical/UV continuum (at wavelengths of a few thousands Å).

- **Hot Corona**

The disk is surrounded by a *corona* of hot, ionized, optically thin gas. The precise location of the corona is still unknown; it is reasonable to assume the corona very close to the accretion disk, probably above it. Microlensing and spectral timing studies locate it within $\sim 10 R_g$ from the SMBH (Chartas et al., 2009; Kara et al., 2016), where $R_g = GM_{\text{BH}}/c^2$ is the gravitational radius. Its high temperature ($T \sim 10^9$ K) is most likely due to magnetic reconnection phenomena.

- **Broad Line Region (BLR)**

It is composed by a number of gas clouds located in proximity of the central source. The gas reprocesses the optical/UV radiation through permitted emission lines from recombination and de-excitation. Forbidden lines are not produced because of the high electron density (10^9-10^{10} cm⁻³). The

temperature of the BLR is $\sim 10^4$ K. The lines are broadened by Doppler effect; widths span from $\Delta v_{\text{FWHM}} \sim 500 \text{ km s}^{-1}$ to $\Delta v_{\text{FWHM}} \gtrsim 10^4 \text{ km s}^{-1}$, with typical values of $\Delta v_{\text{FWHM}} \sim 5000 \text{ km s}^{-1}$. Motions in this region can be used as a probe of the dynamics in the SMBH gravitational well and to estimate the mass of the black hole.

- **Narrow Line Region (NLR)**

It consists of gas clouds at temperatures of 10000 – 25000 K. Densities are lower (10^4 cm^{-3}) than those of the BLR, thus allowing for the production of forbidden emission lines. The bulk velocities are also lower than in the BLR: $200 \leq \Delta v_{\text{FWHM}} \leq 900 \text{ km s}^{-1}$, with average values of $\Delta v_{\text{FWHM}} \sim 400 \text{ km s}^{-1}$. This region is spatially resolved in the optical band: it often manifests itself with an axis-symmetric morphology with two ionization cones centered in the nuclear source.

- **Torus**

It is composed mainly by molecular gas and dust. There are still many uncertainties about the geometry of the torus, in particular whether the material has a smooth or clumpy distribution, and whether there is actually a physical separation from the disk (the alternative hypothesis is that the torus is just the “continuation” of the disk) (Netzer, 2015). Furthermore, the physical extension of the torus is still matter of debate. The torus absorbs optical and UV radiation and reprocesses it via thermal emission in the mid-infrared band, peaking at wavelengths of few tens of micron.

- **Jets**

Relativistic jets are present in about 10% of AGN. The mechanism responsible for the jets is still uncertain, but is probably related to the magnetic fields of the black hole and/or of the disk. Jets originate in the central region and are expected to be aligned with the symmetry axis of the system. They are formed of charged particles and emit mostly via synchrotron mechanism, from the radio to the γ -ray band. In face-on AGN (where the observer has potentially a direct view of the nucleus), relativity effects boost the brightness of the approaching jet with respect to the receding one.

In Figure 1.1 we can see a representation of the overall AGN structure and its components, whose indicative sizes are reported in Tab. 1.1.

The AGN is typically represented as an axis-symmetric system, so observing it from different directions (i.e., along different lines of sight) allows to see different parts, each with its characteristic emission. Even though the classes of objects identified as AGN may appear very heterogeneous, most of their differences can be explained as due to changes in just a few of these parameters: orientation (see Fig.

Component	Size
SMBH	$R_s \sim 0.01 - 10 \text{ AU}$
Accretion disk	$R_{in} \sim 0.01 - 60 \text{ AU}$ $R_{out} \sim 1 - 1000 \text{ AU}$
Broad line region	$R_{BLR} \sim 0.01 - 1 \text{ pc}$
Torus	$R_{torus} \sim 1 - 10 \text{ pc}$
Narrow line region	$R_{NLR} \sim 10^2 - 10^4 \text{ pc}$
Jet	$R_{jet} \sim 10^2 - 10^3 \text{ kpc}$

Table 1.1: Extents of AGN components. $R_s = 2GM_{BH}/c^2$ represents the Schwarzschild Radius.

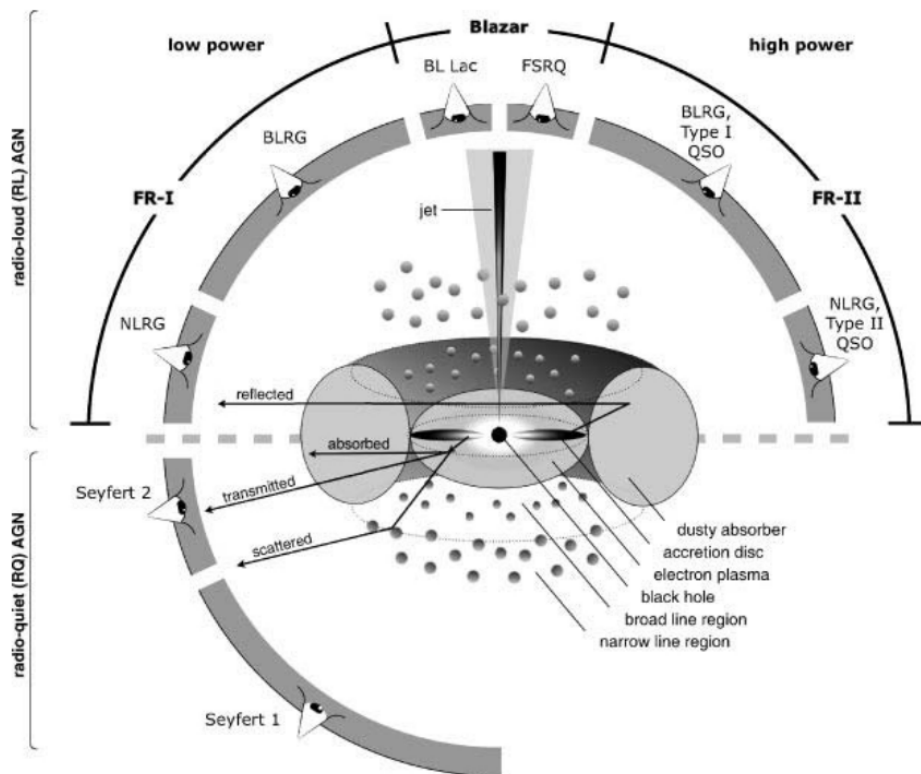


Figure 1.1: Representation of the AGN structure and its components. It is shown how the line of sight can affect the view of the internal regions and so the classification of the object. Image from Beckmann and Shrader (2013).

1.1), accretion rate, presence - or absence - of jets and, possibly, the environment and the host galaxy (Padovani et al., 2017). The so-called Unification Model of AGN is based on the fact that the AGN engine (i.e., accretion onto a SMBH) is the same for most AGN, but orientation effects play a major role in their classification. Orientation is the main discriminant in the classification between type 1 AGN and type 2.

Type 1 objects show broad optical/UV permitted emission lines (FWHM $\sim 1500 - 15000 \text{ km s}^{-1}$) and narrow forbidden lines (FWHM $\sim 500 - 1000 \text{ km s}^{-1}$). The broad lines arise from material with density $n \geq 10^9 \text{ cm}^{-3}$. In type 2 objects both permitted and forbidden lines are narrow, and are produced by gas at lower density, $n \geq 10^{3-5} \text{ cm}^{-3}$ (Beckmann and Shrader, 2013). As shown in Fig. 1.1, this difference is ascribed to the presence of the torus in the line of sight. A similar distinction is made in the X-rays, based on the intrinsic absorption at energies below a few keV, due to matter close to the SMBH (Beckmann and Shrader, 2013). The absorption is typically measured as a column density of hydrogen N_{H} in the line of sight. Objects with lower absorption $N_{\text{H}} \lesssim 10^{22} \text{ cm}^{-2}$ are categorized as type 1, and more obscured sources as type 2.

1.3 Outflows

Winds arising from the accretion disk are a phenomenon observed quite commonly in AGN (e.g Laha et al., 2014; Igo et al., 2020). Their study is of key importance, as they provide a way for the SMBH to influence the host galaxy and explain the observed scaling relations, such as the correlation between the black hole mass and the mass of the bulge (Håring and Rix, 2004), and between the black hole mass and the velocity dispersion of the bulge (Kormendy and Ho, 2013). It has been shown that outflows possessing mechanical energies $\geq 0.5 - 5\%$ of the bolometric AGN luminosity have enough power to imprint the host galaxy (Hopkins and Elvis, 2010). The AGN feedback acts enriching the interstellar medium, quenching (or suppressing) the star formation (King and Pounds, 2015).

The physical properties of winds are observed to cover a wide range of values, and are used to classify them. Warm absorbers are observed in at least 50% of Seyfert galaxies (Reynolds, 1997; Laha et al., 2014). The ionisation parameter of the warm absorbing gas spans almost four orders of magnitude ($\xi \sim 10^{0-4} \text{ erg cm s}^{-1}$), and the column density three orders of magnitude ($N_{\text{H}} \sim 10^{20-23} \text{ cm}^{-2}$), velocities are of the order of 10^3 km s^{-1} (Blustin et al., 2005). The most extreme outflows, the so called Ultra-Fast Outflows (UFOs, Tombesi et al., 2010), are observed in up to 60% of AGN (Tombesi et al., 2010; Gofford et al., 2013; Igo et al., 2020), show velocities up to $\sim 0.2 - 0.4 c$, high ionization, $\xi \sim 10^{3-6} \text{ erg cm s}^{-1}$, and column

densities as large as $N_{\text{H}} \sim 10^{20-23} \text{cm}^{-2}$.

These two types of winds are shown to coexist in multiple sources (Tombesi et al., 2013). Comparative studies of their physical parameters indicate that they could be unified in a single, large scale, stratified outflow, observed at different locations along the line of sight (Tombesi et al., 2013; Serafinelli et al., 2019).

From the velocity of the outflow, it is possible to estimate the distance of the launching region from the SMBH, as the wind velocity has to be higher than the escape velocity, and so the closer the region the faster the wind (Proga, 2007). The fastest winds, UFOs, can be ejected from distances as small as few tens gravitational radii. It is still not clear what the launching mechanisms of winds are. Thermal pressure can be the accelerator for the slowest outflows ($100 - 1000 \text{ km s}^{-1}$; Krolik and Kriss 2001). For more powerful ones, magnetic forces (Fukumura et al., 2015) or radiation force on spectral lines (line-driven winds; Proga 2007) should be invoked.

A key parameter to understand the wind acceleration process is the accretion rate, that can be re-scaled for the SMBH mass via the Eddington ratio $\dot{m} = \dot{M}/\dot{M}_{\text{Edd}} = L/L_{\text{Edd}}$. In fact, it is likely the main physical driver of physical differences in the accretion flow that lead to different observed phenomena in AGN. \dot{m} is proportional to the density of the accretion flow, that in turn regulates the heating and cooling of the matter and through this the emitted radiation and the physical structure of the flow (Giustini and Proga, 2019). An increasing value of \dot{m} promotes the acceleration of stronger winds, ejected from regions closer to the SMBH. If the accretion rate has such a key role in the production of winds, it may be that the canonical classification of AGN does not depend only on geometric factors, but also on the conditions of the accretion flow at the moment of the observation, meaning that we can expect to observe an evolution in some objects (Giustini and Proga (2019) and references therein).

An interesting case is that of sources that, after being observed for years as Seyfert 1 galaxies - i. e. unobscured objects - are caught during obscured phases, with imprints of absorption in the X-rays and in the UV lasting for period as long as years (for example NGC 5548, Kaastra et al. 2014) or as short as weeks (NGC 3783 Mehdipour et al. 2017; NGC 3227 Mehdipour et al. 2021). Examples of striking changes in the spectra of these objects are reported in Fig. 1.2. The obscured state of these sources was determined to be caused by outflows quite different from typical WAs or UFOs, with intermediate characteristics between the two: these winds have high column densities and moderate ionization states, and are flowing at velocities of few 10^3 km s^{-1} , typical of the BLR.

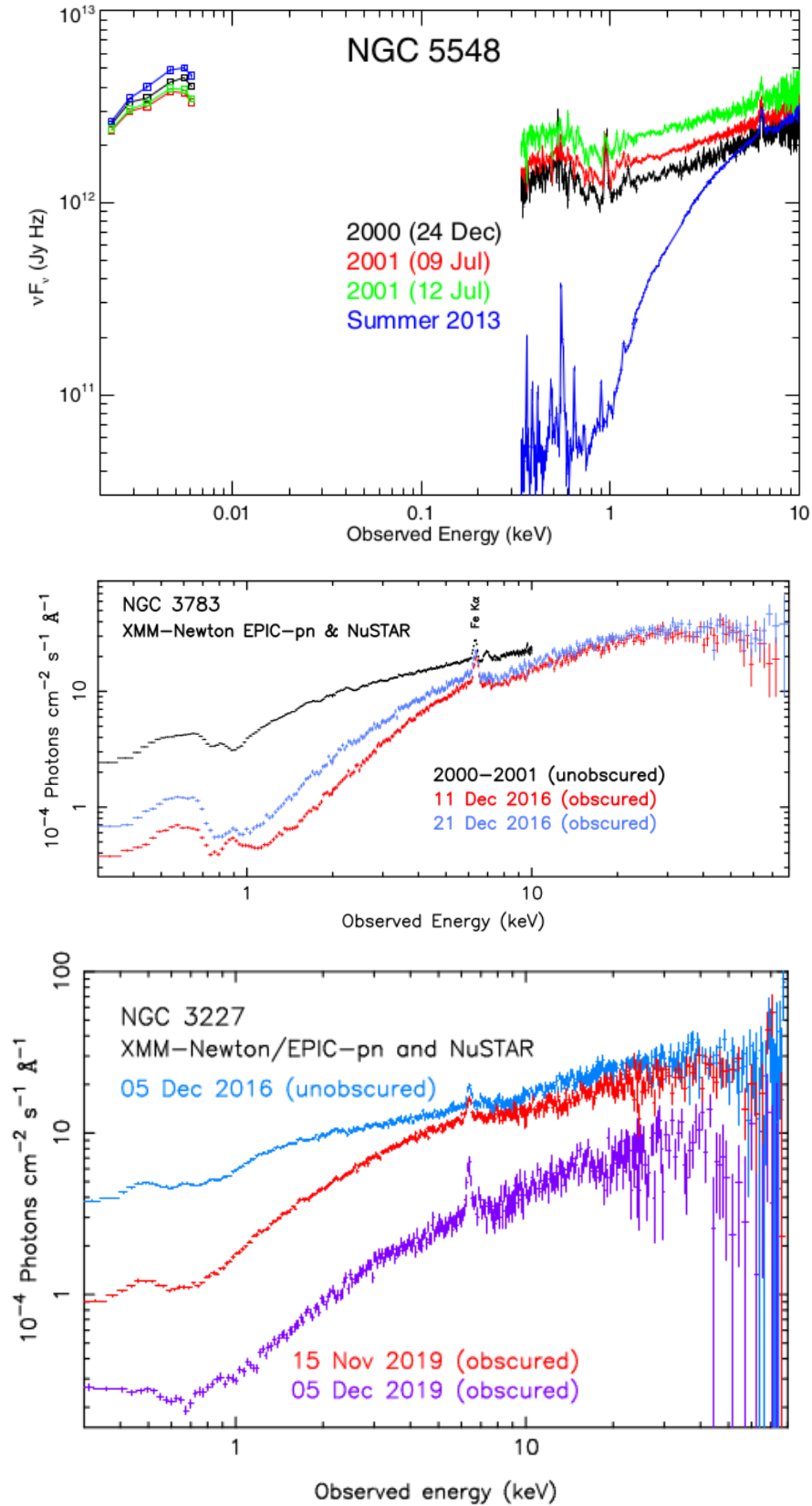


Figure 1.2: Spectra of NGC 5548 (top panel), NGC 3783 (middle), NGC 3227 (bottom) during their unobscured and obscured phases. Credit: [Mehdipour et al. \(2015, 2017, 2021\)](#).

1.4 Seyfert 1 X-ray spectrum

The X-ray spectrum of radio-quiet type 1 AGN (i.e. Seyfert 1 galaxies), in the energy band 0.1–100 keV, can be modeled at a first order as a power law, such as:

$$F(E) \propto E^{-\Gamma} \quad (1.8)$$

where $F(E)$ is the flux in units of photons $\text{cm}^{-2} \text{s}^{-1} \text{keV}^{-1}$. The photon index Γ assumes typical values of $\sim 1.7 - 1.9$ (Mushotzky et al., 1993).

However, a deeper investigation indicates the presence of additional components, in excess or absorption with respect to the primary power law. They are easily detectable in type 1 objects because the X-ray emission from the innermost region is only mildly absorbed. These components arise from specific structures, whose properties can be derived using X-ray spectral analysis. The typical X-ray spectrum of these sources is shown in Fig. 1.3.

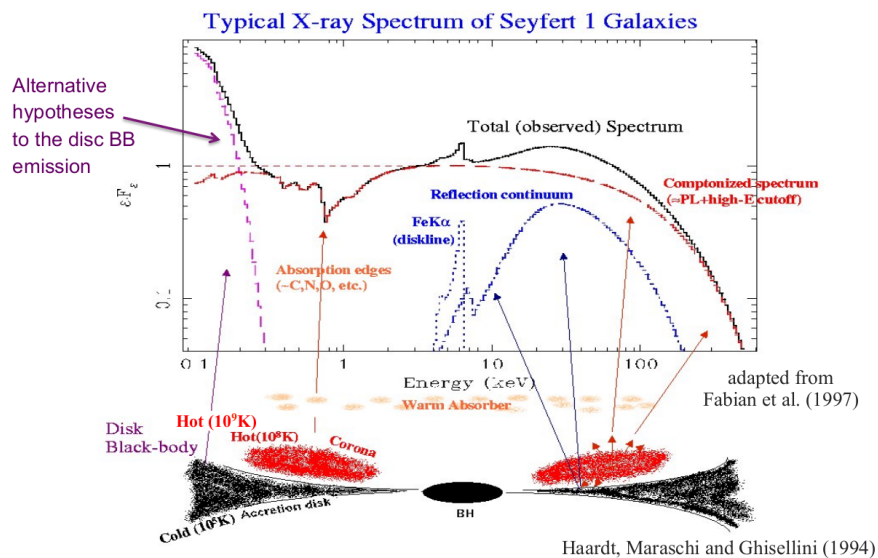


Figure 1.3: The X-ray spectrum of a Seyfert 1 galaxy, in which all the typical features are highlighted with different colors and linked to the component that produces them, in the simplified structure pictured below.

The typical features that we can observe in unobscured type 1 AGN are:

- The **Compton reflection component**, characterized by a flattening of the spectrum for energies above 10 keV, with a peak between 30 and 50 keV (the *Reflection Hump*) and fluorescence lines between 0.1–8 keV from the most abundant elements, such as Fe, C, O, Mg, Cr, Ni. The most prominent features are due to Fe: the Fe $K\alpha$ line at ~ 6.4 keV, the absorption edge

at ~ 7.1 keV and, possibly, the $K\beta$ line at ~ 7.05 keV. The lines are due to fluorescence and are thought to be directly connected with the reflection hump. The physical origin is Compton reflection from an optically thick gas that should be relatively cold, probably associated with the accretion disk or the molecular torus, illuminated by the primary source of X radiation (i.e. the power law).

- A **Cut-off** on power law at energies around $\sim 100 - 200$ keV, that causes a sudden decrease in the flux. This is ascribed to the thermal Comptonization which is responsible for the primary power law emission.
- The **Soft excess** is a strong emission in excess of the power law continuum, at energies of $\sim 0.1 - 2.0$ keV. Its origin is still unclear: some models attribute it to the thermal emission of the inner and hotter part of the accretion disk, other invoke the presence of either a warm corona (Petrucci et al., 2018) or an ionized, possibly relativistic reflection component. Its peculiarity is that for different sources, if fitted with a thermal model, it shows a notably constant temperature, despite differences in the central object masses and in luminosities, suggesting that it is most likely not directly ascribed to accretion disk emission.
- **Photoelectric absorption** due to neutral material. It can be ascribed to gas contained in our galaxy, with typical column densities of $N_H \approx 10^{20}$ cm^{-2} , as well as to gas contained in the source, with column densities up to $N_H \sim 10^{22}$ cm^{-2} (in type 1 Seyferts) and up to $N_H \sim 10^{24}$ cm^{-2} (in type 2 Seyferts), likely related to the torus.
- The **Warm absorber** (introduced above in the outflow context) is composed of partially ionized, optically thin material along the line of sight. It causes the relatively strong absorption features observed in about half of the Seyfert galaxies in the energy range $\sim 0.1 - 2.0$ keV. Its column density can reach $N_H \gtrsim 10^{23}$ cm^{-2} . The precise location and geometry of this gas are not completely clear, although it is supposed to be formed of distinct components, with different densities and properties as a function of the distance from the black hole (Reynolds, 1997).

Two-phase model The most accepted model to explain the production of the power law component observed in AGN is the *two-phase model* (Haardt and Maraschi 1991; Haardt and Maraschi 1993), which provides explanations for the AGN components already described in Sect. 1.2. This model predicts an emission region formed by two distinct structures: the accretion disk, geometrically thin and optically thick ($\tau > 1$) and relatively cold ($T_d \sim 10^5 - 10^6$ K), and above

it the corona, being optically thin ($\tau < 1$), hot ($T_c \sim 10^9$ K, $kT_c \sim 100$ keV) and ionized. From the equipartition of the kinetic energy among the electrons $\frac{m_e v_e^2}{2} = \frac{3kT}{2}$, we have $\beta = \frac{v}{c} = \sqrt{\frac{3kT}{m_e c^2}} \sim 0.7$, corresponding to a Lorentz factor $\gamma = 1/\sqrt{1-\beta^2} \sim 1.4$.

The interaction of these two "phases" leads to a rather complex emission mechanism that we summarize in the following three points:

- The inner regions of the accretion disk produce a black body emission peaking in the optical/UV for reasonably high black hole masses, as observed in AGN.
- Part of this low-energy radiation ($E_{phot} \ll kT_c$) interacts via Inverse Compton with the electron population in the corona and is upscattered towards higher energies. This represents the most efficient cooling process in the corona. The resulting spectral profile follows a power law with $\Gamma \sim 1.9$, up to energies higher than 10 keV. The cut-off is then determined by the electron temperature: when $E_{phot} \sim kT_c$ the energy transfer is no longer efficient and the process stops, producing the observed decrease at $\sim 100 - 200$ keV.
- Assuming an isotropic emission from the corona, about half of the light is radiated towards the observer and about half towards the disk. The interaction of high-energy photons with this colder, optically thick material happens via absorption, Compton scattering and fluorescence. This process is referred to as Compton Reflection. Qualitatively, X-ray photons of energies in the range $\sim 1 - 100$ keV impact on the disk and produce a reflection continuum directed towards the observer, added up to the corona's continuum (the power law). The reflection component shows various emission and/or absorption features, which contain information about the accreting material, as detailed below.

1.4.1 Emission lines

The incidence of the radiation from the corona on the accretion disk produces a reflection continuum and fluorescence lines of the most abundant elements. The most prominent lines are produced by iron (Fe), but the same arguments detailed below apply to all elements.

Fe K lines are originated when the absorption of an X-ray photon with an energy above the threshold of 7.1 keV (iron edge) causes the ejection of one of the two electrons in the K-shell, ionizing the atom. The electronic configuration is in an excited state and the subsequent redistribution can occur in two ways. In one case, an electron from the L-shell transits in the K-shell, releasing a photon at energy 6.4 keV that has a 34% probability of exiting the atom; in such a case,

this photon contributes to the $K\alpha$ line. In the remaining 66% of the cases, the photon is absorbed internally by another electron, which is, in turn, ejected from the atom (Auger effect). The second possibility is that the electronic transition is from the M-shell to the K-shell, producing a photon at an energy of 7.05 keV that we associate with the iron $K\beta$ line. The flux ratio between the Fe $K\beta$ and the Fe $K\alpha$ is $\sim 1 : 8$.

The above considerations are valid when the iron atom is neutral. At higher ionization states, the energies increase accordingly. In particular, the $K\alpha$ line can reach 6.97 keV for H-like iron (i.e., only one electron is left) (Kallman et al., 2004) (Fig.1.4). The energy of the fluorescence line observed in AGN is typically 6.4 keV rest-frame (Mushotzky et al., 1993). This value is consistent with the hypothesis of reflection from cold, neutral material with low velocity, in the disk or in the molecular torus.

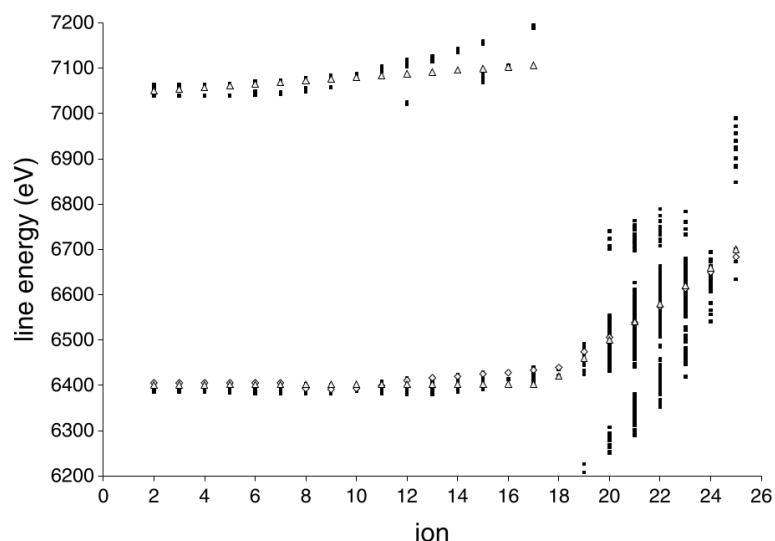


Figure 1.4: Ionization states of the Fe atom vs. energy expressed in eV. The points show the increase of the energy of the Fe $K\alpha$ and Fe $K\beta$ fluorescence lines at increasing ionization levels. Credit: Kallman et al. (2004).

The strength of the line with respect to the continuum is measured by the equivalent width (EW)². In Seyfert 1 galaxies the Fe $K\alpha$ EW spans in the range 50–350 eV, being typically of ~ 150 eV.

²The equivalent width gives the line flux in terms of how much continuum flux one has to integrate in order to get the same flux value. Assuming the continuum intensity f_c is constant over the wavelength range λ_1 to λ_2 and $f(\lambda)$ is the total flux (line plus continuum) at wavelength λ , $EW = \int_{\lambda_1}^{\lambda_2} \frac{f(\lambda) - f_c}{f_c} d\lambda$.

An emission line is intrinsically narrow and can be broadened by several effects, for example thermal agitation or collisions. In the Compton reflection model, it is assumed that the emitting material is the rotating accretion disk, located in the proximity of the SMBH: in this case, the principal distorting effects on the line are due to orbital motion and Relativity. The combination of these factors can then induce a strong profile deformation, as described in the following:

- Classic Doppler effect, due to the motion around the black hole, causing an energy shift. This can be expressed as $E_{obs} = E_{em}(1 \pm \beta)$, where E_{obs} is the measured energy, E_{em} is the emission energy, $\beta = |v|/c$. This effect, depending on the relative velocity between the material and the observer, causes a double-peaked profile, where the receding gas produces the red peak and gas moving toward the observer produces the blue peak (first panel in Fig.1.5). An estimate of the broadening can be derived as follows: matching the centripetal and gravitational forces, $\frac{v^2}{r} = \frac{GM_{BH}}{r^2}$, it is possible to find a relation between the velocity and the distance r from the center of a Keplerian orbit: $\beta^2 = r_s/2r$, being $r_s = 2GM_{BH}/c^2$ the Schwarzschild radius. Using this β in the Doppler effect equation, we find:

$$\Delta E = E_{blue} - E_{red} = E_{em}(1 + \beta) - E_{em}(1 - \beta) = 2E_{em}\beta \propto (r_s/r)^{1/2} \quad (1.9)$$

- The rotational velocity of the accretion disk for an annulus with radius $r \gtrsim r_s$ can be estimated as the velocity of a Keplerian circular orbit: $v \sim (GM_{BH}/r)^{1/2}$, so $\beta \propto (r_s/r)^{1/2}$. In the inner regions, velocities are higher and relativistic effects no more negligible. In Special Relativity the Doppler effect equation can be written as $E_{obs} \simeq E_{em} \sqrt{\frac{1 \pm \beta}{1 + \beta}}$. The line profile is deformed by relativistic beaming, which boosts the blue peak and decreases the red one. The transversal Doppler effect, $E_{obs} \simeq E_{em} \sqrt{1 - \beta^2}$, shifts the whole structure at lower energies (second panel in Fig.1.5).
- When the accreting matter reaches the inner regions ($r \leq 10r_g$), General Relativity effects become important. Gravitational redshift induces a global shift to lower energies, which is larger at smaller distances: $\nu_{obs} = \nu(1 - r_s/r)^{1/2}$ (third panel in Fig.1.5).

All these effects act on the matter producing Fe photons and the dominant effect is determined by the distance from the SMBH. The overall shape of the emitted Fe lines is obtained by integrating from the the internal radius, r_{int} , to the end of the disk, r_{end} . By doing so, we obtain the broadened and asymmetric profile shown in the last panel of Fig. 1.5.

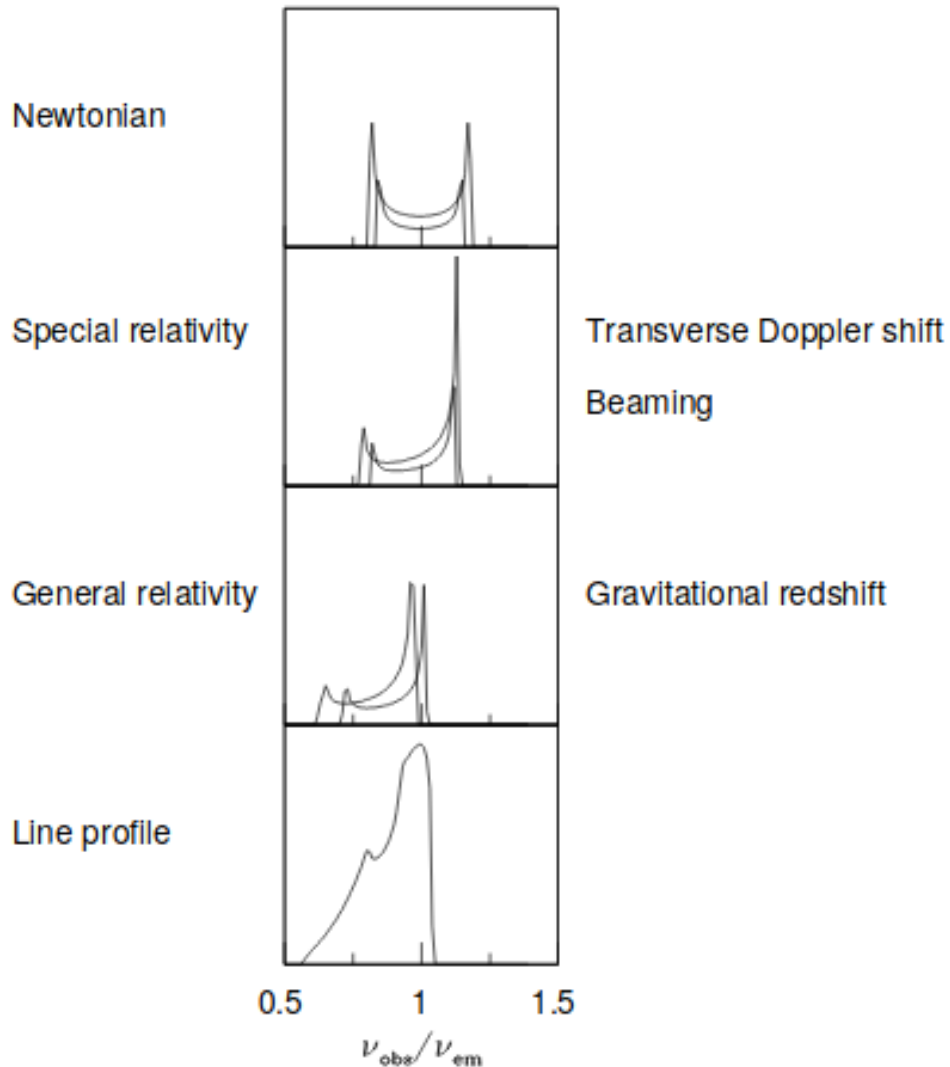


Figure 1.5: Deformations of the Fe K α line shape in AGN spectra due to different effects: in the first panel Doppler shifting due to the rotation; in the second panel, the beaming of the blue-shifted peak and the decrease of the red-shifted one due to special relativity; in the third panel the global shift at lower energies due to general relativity; in the fourth panel the final profile obtained summing all the effects and integrating on the radius of the disk region where the line is emitted. Credit: [Fabian et al. \(2000\)](#).

Many parameters of the disk and the disk-observer system can affect the resulting line shape: the inclination, the internal and external integration radii, the emissivity of each annulus, the ionization state, the density profile, etc. Grossly speaking, however, the extent of the red peak depends on the distance of the innermost part of the disk from the SMBH. In case of a non-rotating black hole, the spacetime metric is described by the Schwarzschild metric and the innermost stable orbit is at $6 r_g$, while for a rotating one in a Kerr metric, the inner radius is located at $1.25 r_g$. The line profiles (shown in the left panel of Fig. 1.6) are different in the two cases, since in presence of a Kerr black hole the profile reaches lower energies. In principle and for a limited number of AGN in the local Universe, these differences in the observed AGN line profiles can be used to infer the spin of the SMBH when compared to models.

The extent of the blue peak is mainly due to the inclination: the line stretches blue-ward when the angle increases, as seen in the right panel of Fig. 1.6.

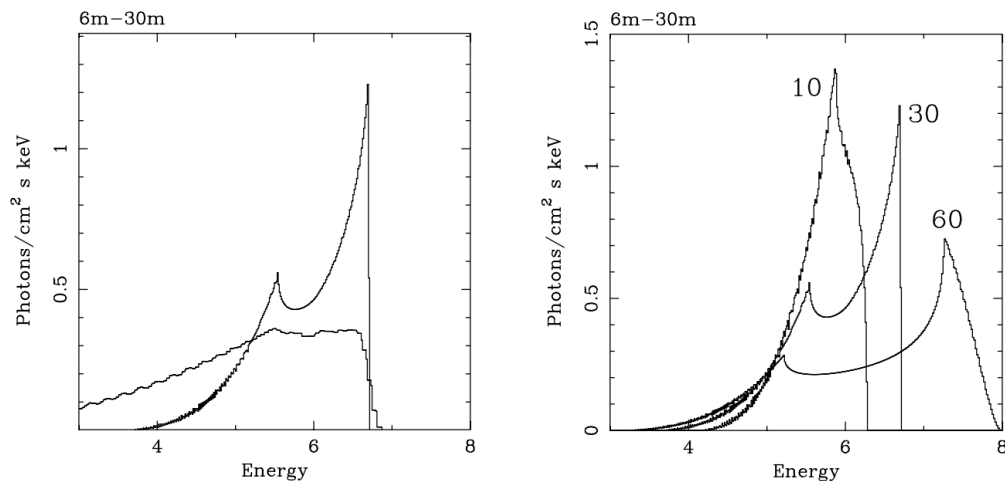


Figure 1.6: On the left panel: comparison of relativistic iron line profiles from an accretion disk around a Schwarzschild black hole (narrower, peaky line) and a near-extremal Kerr black hole (broader line). The line emission is assumed to extend down to the radius of marginal stability which is $6r_g$ and $1.25r_g$, respectively. The difference in the width and redshift of the line is principally a result of the difference in the position of the radius of marginal stability. On the right panel: relativistic iron line profiles for the case of an accretion disk around a Schwarzschild (non-rotating) black hole. It is assumed that the region of the disk producing fluorescence extends from $6r_g$ to $30r_g$. Three inclination angles for the disk are shown: 10° , 30° , and 60° . The main effect of increasing the inclination is to broaden the line by increasing its high-energy extent. Credit: [Fabian et al. \(2000\)](#).

1.4.2 Absorption

Winds are observed in the X-ray as absorption features. Warm absorbers produce a plethora of narrow lines. They can be resolved only in observations made with high spectral resolution instruments (i.e., gratings or microcalorimeters) and are seen altogether as a curvature in the spectrum in imaging exposures. Several Seyfert 1 and RQ AGN show evidence for discrete absorption features in the range $\sim 4 - 10$ keV. They are interpreted as Doppler shifted resonant absorption lines due to highly ionized (H-like, He-like) iron (Cappi, 2006).

In the energy range 4–6 keV these lines are red-shifted and are most likely due to infalling flows with velocities up to 0.1–0.4 c , column densities $\gtrsim 10^{22}$ cm^{-2} and very large ionization parameters ($\xi \sim 1000$ $\text{erg s}^{-1} \text{cm}$) (Dadina et al., 2005). An example is shown in Fig.1.7.

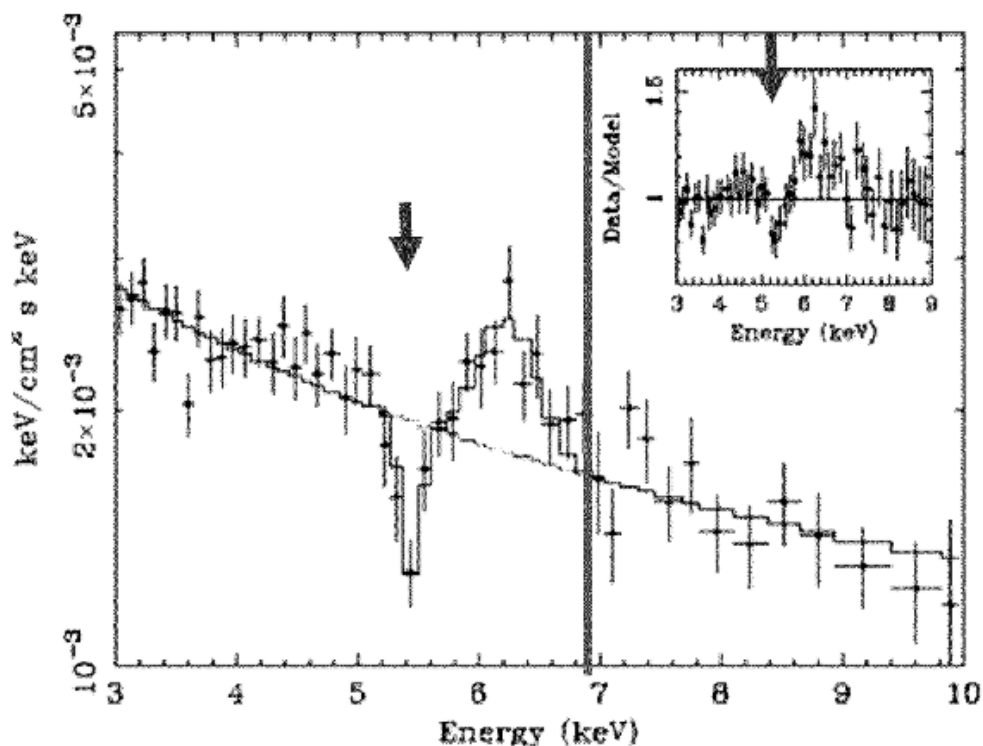


Figure 1.7: BeppoSAX unfolded spectrum of Mrk 509 showing an absorption structure (indicated by the arrow) redward of the Fe K emission line visible at ~ 6.2 keV. The energy at 6.9 keV, corresponding to H-like Fe, is marked by a vertical line. Credit: Dadina et al. (2005), Cappi (2006).

Absorption Fe features blue-shifted at energies above 7 keV are due to gas

moving outwards. Outflows are quite common in AGN and have been studied since a long time, as detailed in Sect. 1.3. An example of absorption due to a UFO is shown in Fig. 1.8.

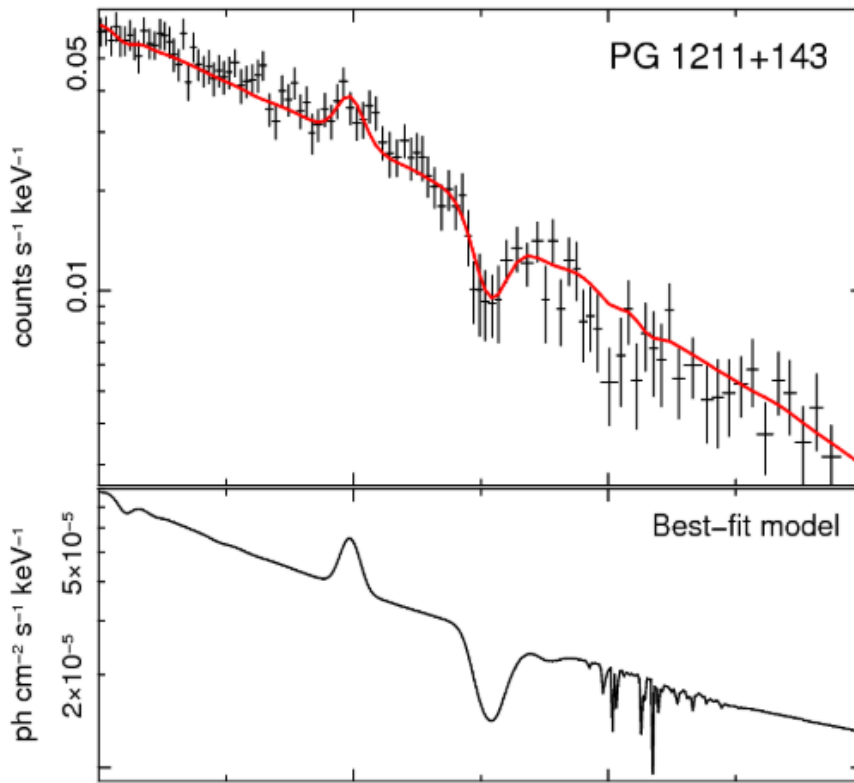


Figure 1.8: XMM-Newton EPIC pn spectrum of PG 1211+143 in the 4–10 keV band, in which a UFO with $v \sim 0.15 c$ has been detected. Upper panel: background-subtracted source spectrum with superimposed the best-fit model. Lower panel: best-fit model. Credit: Tombesi et al. (2010).

1.5 Variability and analysis techniques

AGN display erratic, aperiodic flux variability over a wide range of timescales (from years to minutes; Padovani et al. 2017). The main property of AGN variability is its “red noise” character, namely the occurrence of larger amplitude variations on longer timescales.

Much faster variability is observed in the X-ray band than in any other. In Fig. 1.9 an example of the X-ray light curve of the Seyfert 1 galaxy NGC 3227 is shown.

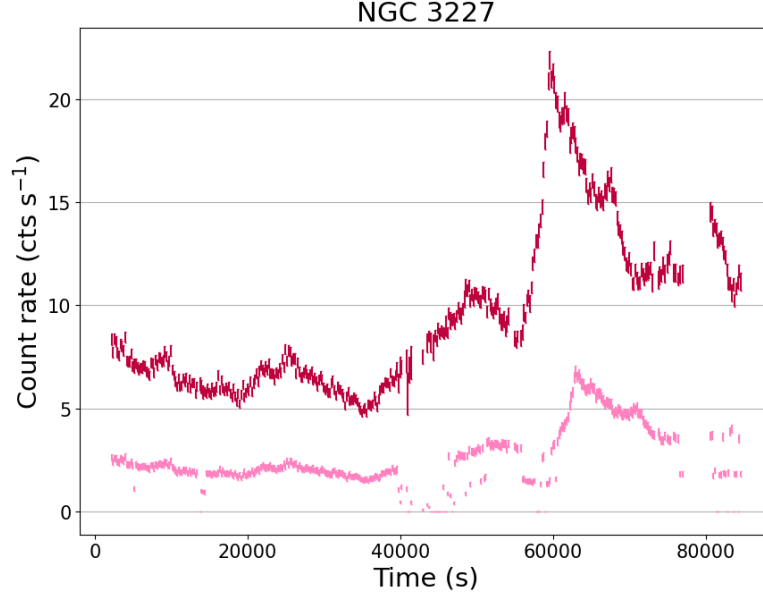


Figure 1.9: Light-curve of NGC 3227 (Obs ID 0782520401) in the energy band 0.3–10.0 keV, with the corresponding background; every time bin has 200s-length. A variation of a factor ~ 4 can be observed in the count rate, on time-scales shorter than ~ 50 ks.

The minimum timescale of variability measured in a given waveband allows us to infer an upper limit for the size of the emitting region. By imposing $R \leq \Delta t c$ (casuality), we find the most rapidly varying regions ($t_{var} \sim \text{few } 10 \text{ ks}$) to have sizes smaller than $\sim 10^{15} \text{ cm} \sim 10^{-3} \text{ pc}$ (Mushotzky et al., 1993). This short variability is thought to originate in the innermost regions of the accretion flow (corona and inner disk). Moreover, it is responsible for driving (at least part of) the variability from the outer accretion disk, observed at longer wavelengths (UV and optical) and over longer periods. Observing diverse timescales for variability in distinct parts of the spectrum can help us to distinguish separate processes in act and understand where they are possibly originated.

In this regard, the variability of the Fe $K\alpha$ lines is particularly interesting, because from the time evolution of their profile we can recognize directly changes due to motions or modifications of the emitting material in the very central regions. For example, by investigating on the geometry and dynamics at small distances from the black hole we can test variations in the Fe $K\alpha$ line originated by orbital motions, analyzing the time scale of the Keplerian orbital period at a distance of $10 r_g$, where $r_g = GM_{BH}/c^2$. It is estimated by Bardeen et al. (1972):

$$T_{orb} = 310 \left[a + \left(\frac{r}{r_g} \right)^{3/2} \right] M_7 \text{ s} \quad (1.10)$$

where a is the black hole spin: $a = 0$ corresponds to a non-rotating black hole, with the surrounding spacetime being described by the Schwarzschild metric, whereas for a maximum rotating black hole with $a = 1$ the Kerr metric is used. M_7 is the SMBH mass expressed in units of $10^7 M_\odot$. The masses of the black holes in AGN typically span in an interval of $10^6 - 10^9 M_\odot$. For a medium value of $\sim 10^7 M_\odot$, we find $T_{orb} \sim 10$ ks.

A practical way to analyze the temporal evolution of this emission feature is the Excess Maps technique, introduced in [Iwasawa et al. \(2004\)](#) and later used in [Turner et al. \(2006\)](#), [Tombesi et al. \(2007\)](#) and [De Marco et al. \(2009\)](#). This time-resolved spectral analysis is based on the representation of excess residuals against a spectral continuum in the time-energy domain. This method allowed [Iwasawa et al. \(2004\)](#) to spot sinusoidal variations of the excess in band 5.7–6.2 keV with a period of ~ 25 ks for the Seyfert 1 galaxy NGC 3516, shown in Fig. 1.10. These results were interpreted as Doppler modulations of a Fe $K\alpha$ line broadened by gravitational redshift. Studying its profile, it was possible to place constraints on the emitting region, limiting it to the range of 7–16 r_g , thus allowing an estimate of the black mass of $(1 - 5) \times 10^7 M_\odot$.

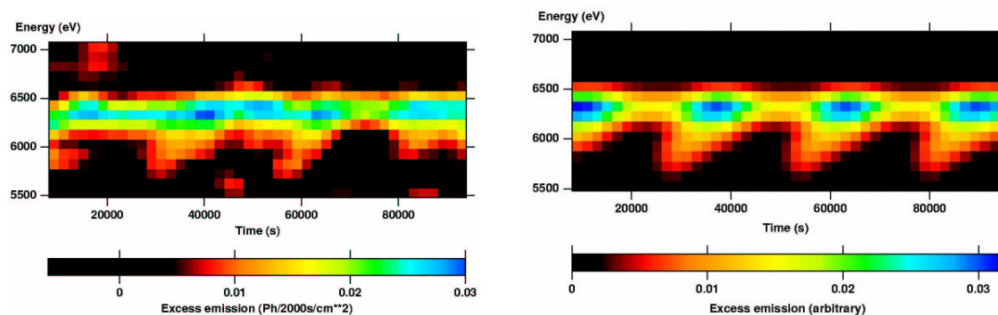


Figure 1.10: Left panel: excess map obtained from a XMM-*Newton* observation of NGC 3516, in which there are recurrent red-ward features. Right panel: a simulated excess map replicating the emission of a flare rotating above the disk: this represents a possible explanation for the data. The y-axis represents the energy, and the x-axis the time. The colour shows the intensity of the residuals against a smooth continuum. Credit: [Iwasawa et al. \(2004\)](#).

Using the same method, [Turner et al. \(2006\)](#) found in Mrk 766 a modulation in the Fe $K\alpha$ emission with period of ~ 165 ks, interpreted as due to orbiting material at distance $\lesssim 100 r_g$ from the black hole, as shown in Fig. 1.11.

In this work we present an “updated” version of the excess maps, the *residual* maps. We consider simultaneously positive and negative residuals, with the aim

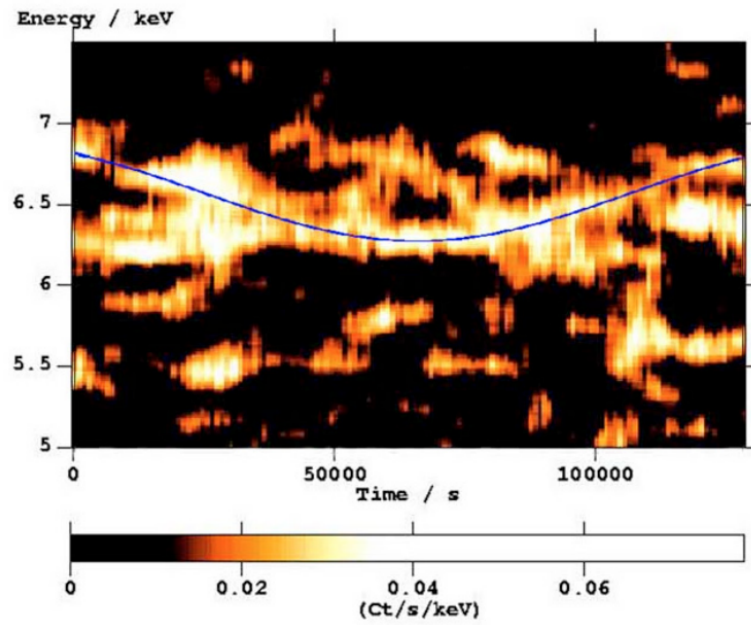


Figure 1.11: Smoothed excess map obtained by a XMM-*Newton* observation of Mrk 766. The blue line follows the periodic energy-shift of the Fe $K\alpha$ peak. Credit: [Turner et al. \(2006\)](#).

of following the variations of both emission and absorption lines.

Chapter 2

Sample and data reduction

In this work we are interested in analyzing objects that underwent an obscuration event. In particular, we want to study them via time-resolved spectral analysis. In fact, it is possible that phenomena happening in the region closest to the SMBH may produce emission/absorption features that would appear only for a limited amount of time or show a variability that would be evened out in long exposures, as they are expected to be transient (Giustini and Proga, 2019). By using time-resolved spectral analysis on short times, we aim at detecting such features and characterizing their variations, then to make a comparison between the obscured and unobscured state of the sources.

To sample short-time scales means to probe regions close to the SMBH, but it requires a high photon statistics: we have to reach a compromise between sampling short time-scales and acquiring a number of photons per time bin that allows us to find significant results in the spectral analysis. We need objects that have been observed both in the obscured and unobscured state by the instrument with the highest collecting area in the Fe K band, which is the EPIC pn on-board *XMM-Newton*.

2.1 *XMM-Newton*

XMM-Newton (X-ray Multi-Mirror Mission) is the ESA cornerstone X-ray observatory, launched in December 1999. On-board there are three X-ray telescopes, each composed of 58 gold-coated shells, nested in a co-axial and co-focal Wolter I configuration (Fig. 2.2). Each shell consists of a paraboloid and an associated hyperboloid grazing incidence mirror. This configuration is necessary to reflect high-energy radiation: on a material with density ρ , photons are reflected if the incidence angle is lower than a critical angle $\theta_{crit} \propto \sqrt{\rho}/E$. The focusing optics grant a good angular resolution: the Point Spread Function (PSF, the distribution on the focal plane of a point-like source) has a Full Width at Half Maximum (FWHM) of $\sim 6''$ at the center of the Field of View, and Half Energy Width (HEW, the PSF diameter that includes 50% of the total energy of the source) of $\sim 15''$, since the PSF has not a Gaussian shape (see Fig. 2.1).

There is also an optical/UV telescope, used to observe counterparts of the X-ray sources.

2.1.1 The on-board instruments

The three main scientific instruments on-board *XMM-Newton* (see Table 2.1) are:

- The European Photon Imaging Camera (EPIC): three CCD cameras, *pn*, *MOS 1* and *MOS 2*, each on the focal plane of one of the three X-ray tele-

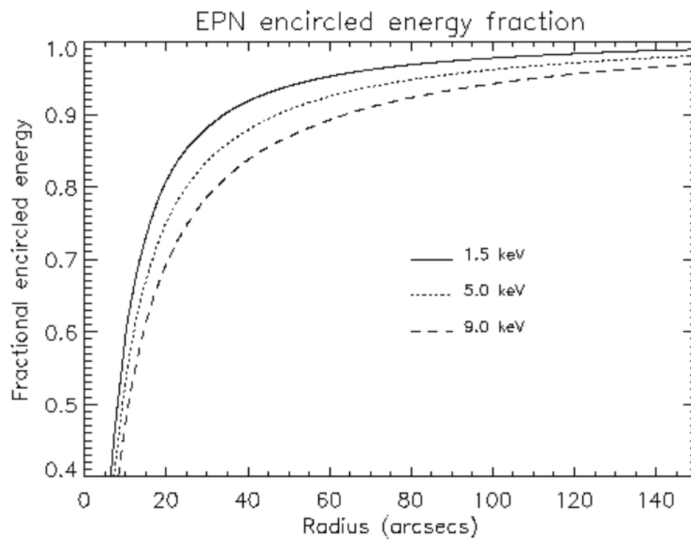


Figure 2.1: The pn fractional encircled energy as a function of the spectral extraction radius at different energies. This plot shows what is the fraction of photons contained in a given extraction radius for a point-like source at a given energy. The curves are calculated integrating the PSF. Credit: ESA's *XMM-Newton* Users Handbook.

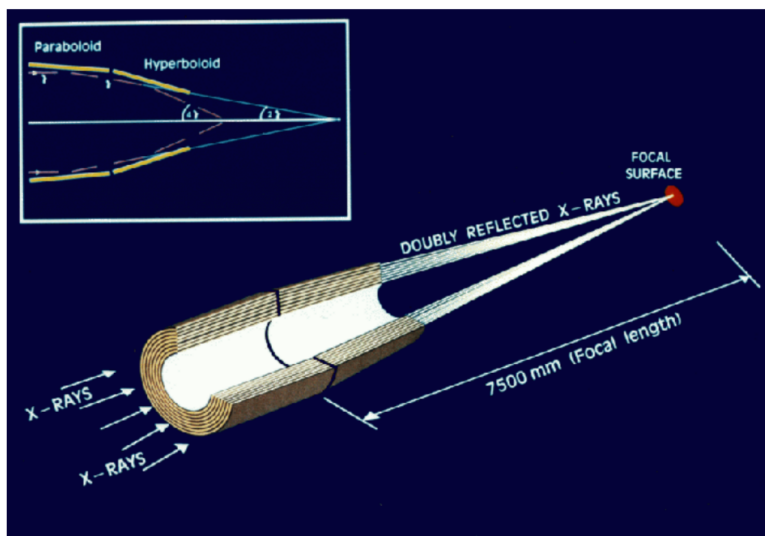


Figure 2.2: Light path in the *XMM-Newton* telescope with EPIC pn camera in its primary focus. The grazing incidence optics are in Wolter I configuration. The double reflection, first on a paraboloid and then a hyperboloid surface, optimizes the collection of high-energy photons. Credit: ESA's *XMM-Newton* Users Handbook.

scopes. The EPIC CCDs produce images and offer medium-quality spectroscopy, with a resolving power $E/\Delta E \sim 20\text{-}50$; around the Fe $K\alpha$ line ($E \simeq 6.4$ keV) this corresponds to a spectral resolution of ~ 150 eV.

- The Reflection Grating Spectrometer (RGS): two identical spectrometers, which grant an excellent spectral resolution, with $E/\Delta E \sim 200 - 800$, for energies from ~ 0.3 keV up to 2.5 keV. They are mounted on the same telescopes of the MOS: the incident light is split by a grating (RGA): $\sim 40\%$ of the photons are diverted towards the RGS and $\sim 44\%$ reach the MOS directly, while a small fraction is lost.
- The Optical Monitor (OM): it produces optical and UV images and spectra in different filters between 170 nm and 650 nm.

Instrument	EPIC pn	EPIC MOS	RGS	OM
Bandwidth	0.15 - 15 keV	0.15 - 12 keV	0.35 - 2.5 keV	180 - 600 nm
Sensitivity ^a	$\sim 10^{-14}$	$\sim 10^{-14}$	$\sim 8 \times 10^{-5}$	20.7
Field of view	30'	30'	$\sim 5'$	17'
FWHM	6"	5"	5"	1.4"-1.9"
HEW	15"	14"	14"	-
Pixel	150 μm (4.1")	40 μm (1.1")	81 μm	$\sim 0.48''$
Time resolution ^b	0.03 ms	1.5 ms	16 ms	0.5 s
Spectral resolution	~ 80 eV ^c	~ 70 eV	0.04/0.025 \AA ^d	350 ^e

Table 2.1: Technical characteristics of the detectors on XMM-Newton.

(a) Expressed in $\text{erg s}^{-1} \text{cm}^{-2}$ for pn, MOS and RGS.

(b) In timing mode for EPIC, high time-resolution mode for RGS and fast mode for OM (the fastest data acquiring modality for each detector).

(c) At 1 keV, it becomes 150 eV at 6.4 keV for both EPIC cameras.

(d) 3.2 eV at 1 keV.

(e) Resolving power expressed as $\lambda/\Delta\lambda$.

Data from ESA's XMM-Newton Users Handbook.

In Fig. 2.3 the effective areas of the three EPIC instruments are shown, compared to the two ACIS (Advanced CCD Imaging Spectrometer) onboard NASA's Chandra X-ray Observatory: we note that XMM-Newton sensitivity is considerably higher at all energies. In particular, the pn camera has the highest response, reaching a maximum of $\sim 1270 \text{ cm}^2$ at $E \simeq 1.5$ keV and about $700\text{-}800 \text{ cm}^2$ in the Fe K energy band ($E \sim 6\text{-}7$ keV). The EPIC MOS cannot achieve such a high sensitivity, not even if MOS 1 and 2 are added together: this is to be ascribed to the partition of the light with the RGS spectrometers.

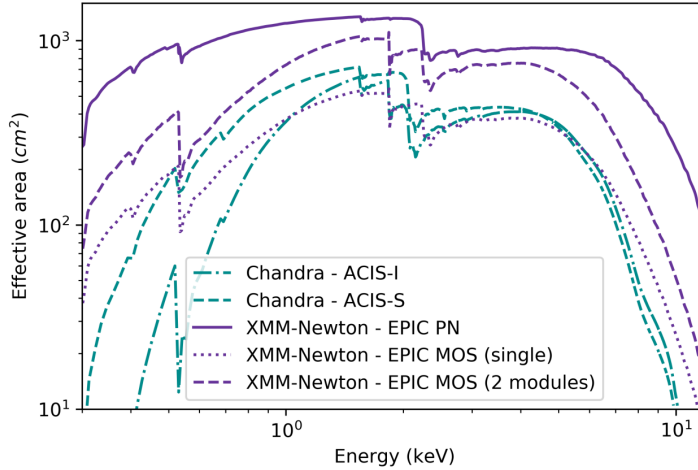


Figure 2.3: Comparison of the effective areas of instruments onboard *Chandra* and *XMM-Newton*. The pn instrument onboard *XMM-Newton* is the most suitable for the kind of investigation described in this thesis, since it guarantees the collection of a large number of counts up to high energies, including the iron line spectral interval.

2.2 Sample selection

We selected sources classified as Seyfert 1 galaxies in the SIMBAD astronomical database (Wenger et al., 2000) and matched this sample with the 4XMM-DR11 catalogue (Webb et al., 2020). We imposed a lower limit for the flux of the pn exposures in the Fe K band, that corresponds to band 5 (4.5-12 keV) in the catalogue. The threshold we set is 10^{-11} erg cm $^{-2}$ s $^{-1}$. Among the sources that resulted from this cut, we hand-picked those that have an obscuration event already reported in literature, to the best of our knowledge. This selection process led us to four objects: NGC 3783, NGC 3227, NGC 5548, NGC 985 (also known as Mrk 1048). Thus the number of sources is not large enough to allow us to draw strong and general conclusions, and we expect that the results will be most probably driven by the single cases. We think, however, that such study is important to pave the way for the opportunities that will be opened by the new instrumentation such as the incoming *Xrism/Resolve* (XRISM Science Team, 2020), and *Athena/X-IFU* (Barret et al., 2018), that will be launched in the next decade.

The observations available at that time of NGC 3783, NGC 5548 and NGC 3227 have been studied with the time-resolved spectral analysis technique of the Excess Maps (see Sect. 1.5) by De Marco et al. (2009) and, in particular, NGC 3783 have been thoroughly analyzed with the same method by Tombesi et al. (2007). Part of our analysis consists in visualizing the evolution in time and energy of discrete emission and absorption features via Residual Maps, that are an update of Excess

Source	M_{BH} $10^7 M_{\odot}$	$T_{\text{orb}} 10 R_g$ ks	Min rate cts s^{-1}	Δt ks	Sampling $10 R_g$	Light path R_g
NGC 3783	3 ⁽¹⁾	29.4	1.21	5	0.17	34
NGC 3227	0.5 ⁽²⁾	4.9	1.04*	5	1.02	204
NGC 5548	4.8 ⁽²⁾	47.0	0.74	7	0.15	30
NGC 985	20 ⁽³⁾	196.1	0.37	13.5	0.07	14

Table 2.2: In this table we report the black hole masses of the sources in our sample as found in literature ((1) [Peterson et al. 2004](#), (2) [Bentz and Katz 2015](#), (3) [Vasudevan et al. 2009](#)), second column, and the corresponding orbital period at a distance of $10 R_g$ calculated using equation 1.10, third column. The minimum count rate value for the 4.5-12 keV energy band is from the 4XMM-DR11 catalogue ([Webb et al., 2020](#)), fourth column, and we use this value to determine the time bin size Δt we are going to use in our time-resolved analysis in order to have a minimum of 5000 photons in each sliced spectrum, fifth column. Lastly we show what fraction of the $T_{\text{orb}} 10 R_g$ is sampled in each extracted spectrum, sixth column, and the light path covered in our bin size, seventh column.

Maps: for this reason, we decided to start our work with NGC 3783, in order to have a direct comparison with literature and test the validity of our approach. In Chapter 3 we will present our method, using NGC 3783 as a test case.

To determine the physical scales we can probe, we calculate with Eq.1.10 the Keplerian orbital period at the nominal distance of $10 R_g$ for each of the sources. We chose this distance as it is where the most powerful winds are supposed to be launched from the accretion disk ([Giustini and Proga, 2019](#)). Then we check for the minimum count rate in band 5 for the pn, reported in the catalogue, and calculate the size of the time bins we need to reach a decent photon statistics in each extracted spectrum in order to have meaningful results. We set this threshold at 5000 photons for spectrum. By comparing these two time-intervals we determine how much of the orbit we can sample in our time bins. Moreover, we measure the time bins in terms of light travel time in order of gravitational radii, so to understand the physical scales on which we observe variability. The results are shown in Tab. 2.2.

Among the observations of NGC 3227, two have a particularly low flux, namely OBS ID 0101040301 and 0844341401, with count rates less than half than in the others. We chose to use larger time bins (13.5 ks) only for these two pointings, in order to maintain a short time resolution for the majority of the observations.

2.3 Data reduction

Table 2.3 reports all of the observations used in our analysis.

All datasets were reduced using the same procedure. Source photons were collected from a circular region of 40 arcsec, that correspond to $\sim 90\%$ of the encircled energy at on-axis position (Snowden et al., 2004). The background regions were selected to be on the same CCD, but far enough from the source to prevent contamination. We selected good time intervals by checking the lightcurve at energies above 10 keV and excluded time of high background; for this reason, we excluded an entire observation of NGC 985 (OBS ID 0743830601), too badly affected by flares to be used. We checked for pile up and did not find it for any observation.

CHAPTER 2. SAMPLE AND DATA REDUCTION

Obs ID	Count rate $_{4.5-12 \text{ keV}}$ (ct s^{-1})	Exposure (s)
NGC 3783		
0112210101	2.257 ± 0.009	25468
0112210201	1.806 ± 0.005	81538
0112210501	2.353 ± 0.005	86125
0780860901	1.215 ± 0.005	47058
0780861001	1.463 ± 0.009	19356
NGC 3227		
0101040301	0.453 ± 0.005	29642
0400270101	1.439 ± 0.004	89256
0782520201	1.386 ± 0.006	46012
0782520301	1.042 ± 0.006	27046
0782520401	1.257 ± 0.006	38491
0782520501	1.496 ± 0.007	37201
0782520601	1.638 ± 0.005	57358
0782520701	1.570 ± 0.006	41807
0844341301	1.339 ± 0.005	58738
0844341401	0.368 ± 0.004	26356
NGC 5548		
0109960101	1.307 ± 0.009	15821
0089960301	1.596 ± 0.006	41272
0089960401	1.982 ± 0.011	17824
0720110301	0.745 ± 0.005	33927
0720110301	1.440 ± 0.007	36200
0720110501	1.090 ± 0.005	37559
0720110601	1.560 ± 0.007	36609
0720110701	1.362 ± 0.006	35923
0720110801	1.372 ± 0.006	36678
0720110901	1.205 ± 0.006	36711
0720111001	1.298 ± 0.006	36834
0720111101	1.478 ± 0.007	32485
0720111201	1.465 ± 0.007	37106
0720111301	1.325 ± 0.006	34919
0720111401	1.217 ± 0.006	35857
0720111501	1.147 ± 0.007	25434
0720111601	1.173 ± 0.006	28703
0771000101	1.008 ± 0.008	15223
0771000201	1.087 ± 0.007	22334
NGC 985		
0690870501	0.373 ± 0.003	61256
0743830501	0.475 ± 0.003	70412
0743830601	0.615 ± 0.003	63426

Table 2.3: All observations analyzed in this work. All values are taken from 4XMM-DR11 catalogue (Webb et al., 2020).

Chapter 3

NGC 3783

NGC 3783 is a Seyfert 1 galaxy at redshift $z = 0.0097$ (Theureau et al., 1998), with a SMBH mass of $M = 3.0 \pm 0.5 \times 10^7 M_{\odot}$, as estimated via reverberation mapping studies in optical and UV bands (Peterson et al., 2004). Analyzing the *XMM-Newton* observation taken in 2001 (Reeves et al., 2004, hereafter R04) identified several features: a strong Fe K α at 6.4 keV, an emission line at ~ 7 keV due to a blend of neutral Fe K β and H-like Fe, and absorption at ~ 6.6 keV due to highly ionized Fe, plus an absorption edge at ~ 7.1 keV. In the same dataset, Tombesi et al. (2007) found a modulation of the flux and a correlated variation of the Fe K α with a broad redshifted component on time-scales of ~ 27 ks. In December 2016, during a *Swift*/XRT monitoring program, NGC 3783 showed heavy X-ray absorption produced by an obscuring outflowing gas (Mehdipour et al., 2017, M17 hereinafter). As a result, new absorption lines from Fe XXV and Fe XXVI appeared in the *XMM-Newton* spectrum. From their analysis, M17 found for the outflow a column density of a few 10^{23} cm^{-2} and a velocity of few 1000 km s^{-1} , and interpreted it as a clumpy, inhomogeneous medium consistent with clouds at the base of a radiatively-driven disk wind located in the outer broad line region of the AGN. A similar but less intense obscuration event was revealed by Kaastra et al. (2018) in a *Chandra*/HETG observation taken in August 2016, with a column density of one order of magnitude lower than the one derived in December 2016. Using all the X-ray observations of NGC 3783, from 1993 (*ASCA*) to 2016 (*Chandra*), it was clear that the source displayed an absorption column density larger than 10^{22} cm^{-2} in roughly 50% of the observing time. De Marco et al. (2020, hereafter DM20) constrained the short time scales (from about one hour to ten hours) variability properties of the obscurer in the 2016 *XMM-Newton* dataset. Their spectral-timing analysis showed that the observed fast variations in the soft X-rays were consistent with changes in the ionization parameter. This study allowed inferring a recombination time of $\lesssim 1.5$ ks, corresponding to a lower limit on the electron density of $n_e \sim 7.1 \times 10^7 \text{ cm}^{-3}$. This value is consistent with M17 results and places the obscurer at a distance between 7 and 10 light days. There are seven observations of NGC 3783 in the *XMM-Newton* Science Archive, but two of them (OBS ID 0112210401 and OBS ID 0112210601) were excluded from our analysis because of their short duration (~ 4 ks). The remaining observations we analyzed are listed in Table 2.3. Following M17 and DM20 we identify two epochs, corresponding to the state of the source: observations from 2000 and 2001 caught the source in an unobscured state, and are hereafter identified as U1, U2 and U3, while during the observations taken in 2016 the source was in an obscured state, so they are named as O1 and O2.

As detailed in Sect. 2.2, we set the size of the time bins for this source at 5 ks, obtaining a total of 88 spectra, 56 for the unobscured dataset and 32 for the obscured one.

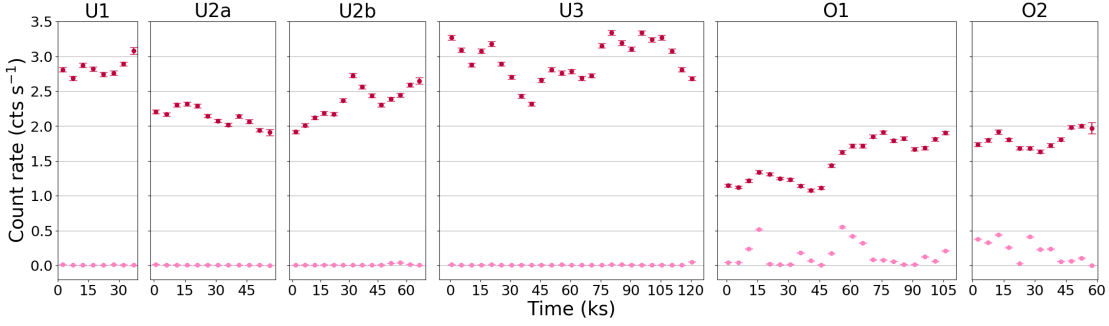


Figure 3.1: Background-subtracted light curve of NGC 3783 (red points) with the corresponding background (pink points), extracted in the 4-10 keV band. The time bins are 5ks. The identifiers of each observation (U1-3, O1-2) refer to the state of the source (Unobscured, Obscured), as pointed in Sect. 3

As already reported, the mass of the SMBH NGC 3783, as estimated by [Peterson et al. \(2004\)](#) via reverberation mapping, is $3 \times 10^7 M_{\odot}$. In the non-spinning case, $a = 0$, we find that that 5 ks corresponds to the orbital period at $\sim 3 R_g$. Therefore, using this time-scale we can over-sample periodicities or variations occurring at larger radii, meaning that we may probe and map regions just outside of the event horizon. In terms of light travel time, 5 ks correspond to a few tens (~ 35) R_g .

3.1 Baseline model

The blind search for features basically consists in finding significant deviations from a baseline model, so the choice of it is particularly important.

We limit the energy band of the analysis between 4 and 10 keV, and this allows us to use a simple model, including only a power law, an absorption component (intrinsic to the source, as the Galactic absorption effects are only visible at lower energies), and a narrow Gaussian emission line for the neutral Fe $K\alpha$ line, that is always present in Seyfert 1 galaxies.

NGC 3783 has shown a combination of cold and mildly ionized absorbers throughout the years (R04, [Yaqoob et al. 2005](#), M17, [Mao et al. 2019](#)). In 2016 the source was under a monitoring campaign made through *Swift*, and in December a change in the hardness ratio triggered *XMM-Newton* observations, that revealed an increase on the column density and the presence of a low-ionization component (M17). Trying to model such a complex combination of media would not give any significant result when fitted on spectra with exposures as short as 5 ks, so it is necessary to simplify. Moreover, we are not trying to thoroughly analyze the variations of the whole system, but only trying to isolate discrete features. With

this in mind, we have to choose a model that, even if not physically accurate, can reproduce the shape of the continuum. On the one hand, the simplest possible absorption (cold and totally covering) introduce some systematics (as detailed in Sect.3.5); on the other hand, a more complex model including ionized matter would reproduce the discrete features we aim at finding and studying individually, therefore it cannot be used. We choose to use a partial covering cold absorption absorber, that should mimic well enough the continuum shape and also intrinsically contains the possibility of a totally covering medium. We also include a narrow emission line in the model, to account for the Fe $K\alpha$ line which is known to be present and is typically sufficiently strong ($EW \sim 100 - 150$ eV) to alter the 4–10 keV continuum fit if not properly taken into account. The baseline model in XSPEC is `pcfabs × (power law + gauss)`.

3.1.1 Fe $K\alpha$ line

Following the results of M17, we assume the Fe $K\alpha$ to be narrow, with a frozen width of 10 eV. The other line parameters (energy and normalization) are left free to vary.

In Fig. 3.2 we show the energy, normalization, and equivalent width (EW) of the narrow Fe $K\alpha$ as obtained from the fits of each time-resolved spectrum, and their average values in individual observations. We do not report major variability in none of the line parameters, except for a shift in the centroid energy (~ 50 eV) between unobscured and obscured datasets. We checked if a similar change is detected also in the MOS data using the average spectra for each of the six observations but we did not find any evidence for such a shift. We therefore conclude that the observed variations is most probably due to uncorrected charge transfer inefficiency (CTI) evolution that translates into a poor gain calibration, as described in [Ponti et al. \(2013\)](#), [Mehdipour et al. \(2015\)](#), and [Zoghbi et al. \(2019\)](#). In addition, the energy of the narrow Fe K line displays some short episodes of significant variation (see U3, O1 and O2 in the upper panels of Fig. 3.2) on time-scales of tens of ks.

The EW of the line appears to be constant within each single pointing, as shown in the lowest row of Fig. 3.2, despite the almost 30% variability in continuum flux for the most extreme cases (Fig. 3.1, U2b, U3, O1). This is not expected when assuming that the narrow Fe $K\alpha$ emission line is produced far from the origin of the primary X-rays. In this case, we would expect a decoupling between the normalization of the line and the continuum flux, thus variations in the EW which is their ratio, due to the time-delays introduced by the distance of the reprocessor. The easiest way to explain this is to associate this emission component with a feature produced in the vicinity (i.e. fast responding) of the SMBH. Under this assumption, one would expect it to be related to a relativistically modified iron

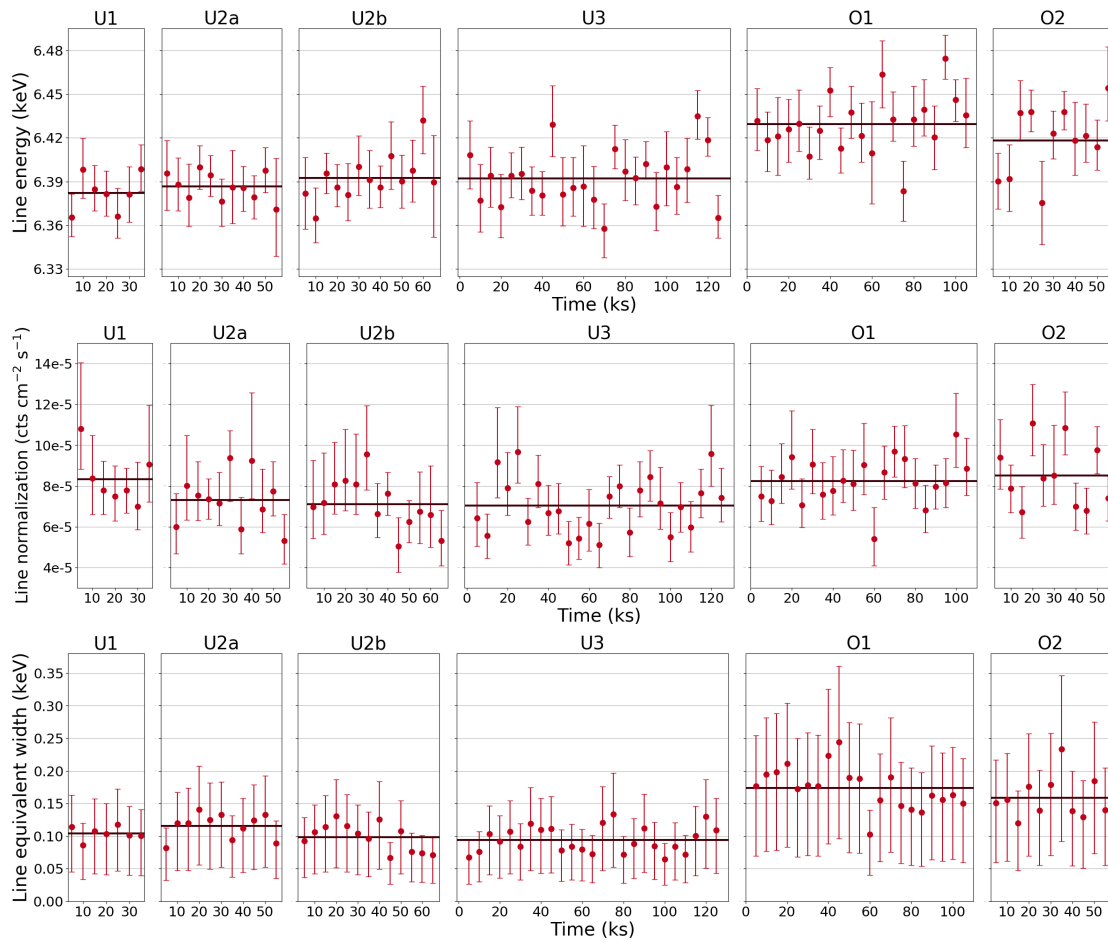


Figure 3.2: Rest-frame energy (top panel), normalization (middle panel), and EW (bottom panel) of the narrow Fe K α line included in the baseline model; errors are reported at 1σ .

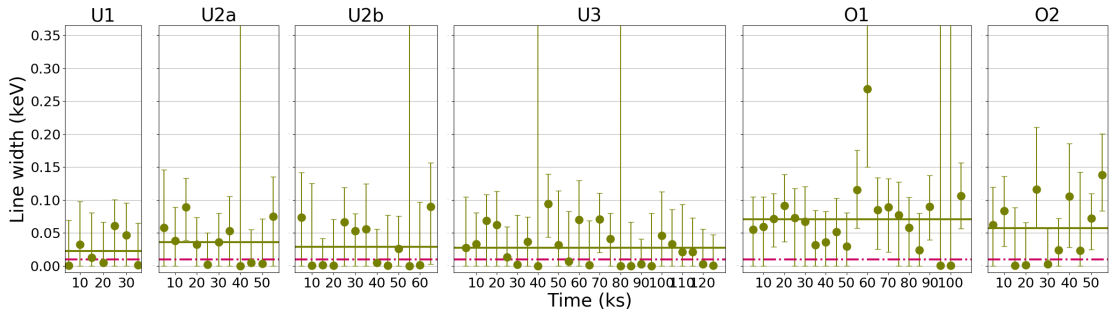


Figure 3.3: Width of the Fe $K\alpha$ line. The magenta dotted line marks the frozen 10 eV width used in the baseline model. All errors are reported at 1σ .

emission line. On the one hand, if this were the case, we would expect some variability in line shape on short time-scales, as predicted for example in light-bending scenarios (Miniutti and Fabian, 2004). On the other hand, D20 demonstrated that the variability of the source is strongly influenced by changes in the absorber characteristics also at small time-scales ($\sim 1500s$). This is in agreement with the apparent steadiness of the EW of the emission feature. Overall, we stress here that the 1σ error on the Fe $K\alpha$ line normalization is of the order of 25 – 30% (middle row of Fig. 3.2). This impacts on our capability to deeply investigate the iron line intensity variability on these time-scales. We cannot claim strong evidences for variation but, at the same time, we cannot exclude them if they are of the order of $\sim 10\%$.

On larger time-scales, from 2001 to 2016 observations, we may appreciate an increase in the average value of Fe $K\alpha$ EW of the order of 70 eV. Assuming that the energy of the line remains the same between the two sets of observation, this increase in EW is consistent with the rise of the absorber column density and decrease in flux (M17).

In order to verify whether the assumption of a narrow line (width fixed at 10 eV) was correct, we left its width free to vary. The average values we obtained for its width is of ~ 30 eV for the unobscured state and ~ 70 eV for the obscured state (Fig. 3.3). The width was, however, always consistent with 0 to within 2σ . We thus decided to keep the width frozen to 10 eV for the following steps of the analysis.

3.2 Blind search

After fitting the baseline model described in Sect. 3.1, we carry out a blind search for additional emission/absorption features. Since the only discrete component present in the baseline model is the Fe $K\alpha$, we may expect to detect also features

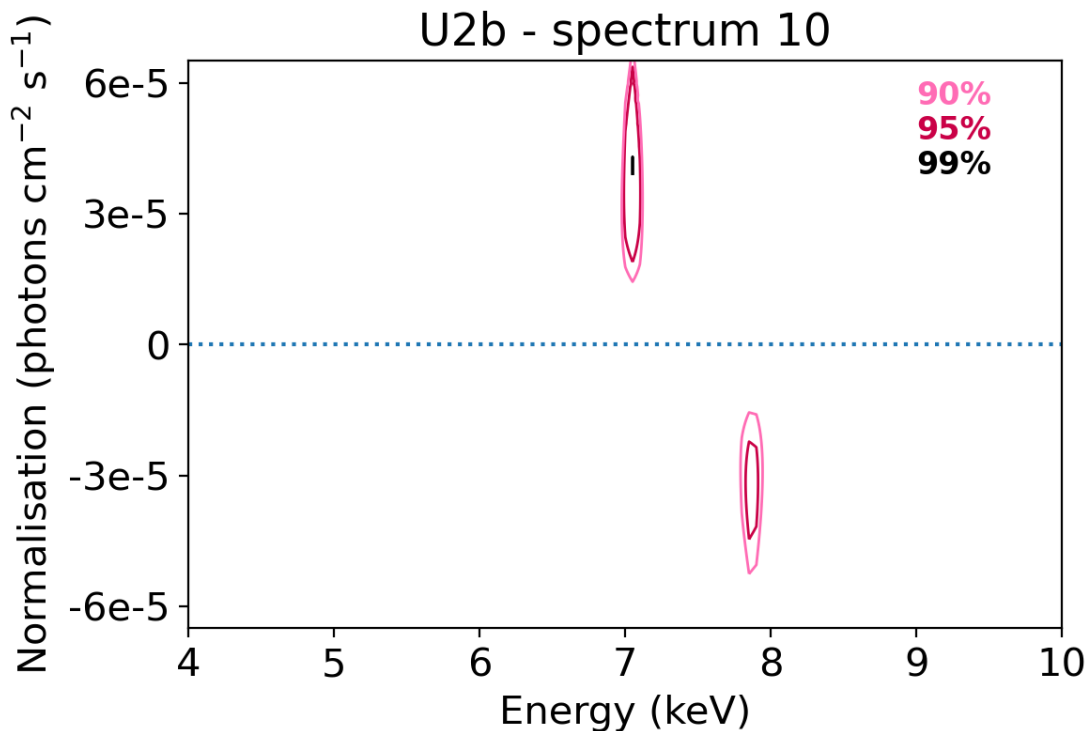


Figure 3.4: An example of the significance contours found with the blind search in a single 5 ks spectrum. An emission line is detected at $\sim 3\sigma$ (99%, i.e. $\Delta\chi^2 \leq -11.34$, $\Delta\text{d.o.f.} = 3$) at ~ 6.9 keV and an absorption line is detected at $\sim 2\sigma$ (95%, i.e. $-7.81 \geq \Delta\chi^2 > -11.34$, $\Delta\text{d.o.f.} = 3$) at ~ 7.9 keV.

(like the Fe $K\beta$ /ionized Fe $K\alpha$ blend and the absorption lines described in R04 and M17) that appear in the average spectrum. Our purpose is to verify whether they are present at all times or do show some variations that get evened out, and are therefore unnoticed, in the average spectra. We apply a procedure similar to that adopted in Tombesi et al. (2010): a second Gaussian component is added to the model, allowing for both positive and negative values of the normalization, and with width in the range 0.01–0.5 keV. Then the `steppar` command is launched simultaneously on the line energy parameter (which can vary from 4 to 10 keV, with increments of 5 eV) and the normalization parameter (from -6.5 to $+6.5 \times 10^{-5}$ photons/s/cm $^{-2}$, with increments of 6.5×10^{-7} photons/s/cm $^{-2}$). We then plot the significance contours corresponding to $\Delta\chi^2$ of -6.25, -7.81, -11.34 that, for three free parameters, represent a significance of the line of 1.6 ($\geq 90\%$), 2 ($\geq 95\%$), and 3 ($\geq 99\%$) σ , respectively. An example of these contour plots is shown in Fig. 3.4, where an emission line is detected at $\sim 3\sigma$ at $E \sim 6.9$ keV and an absorption line is found at $\sim 2\sigma$ at ~ 7.9 keV.

This procedure is repeated for all the 5ks-long, time-resolved spectra. Since the obscured/unobscured state of the X-ray source may influence the number and type (i.e. emission vs absorption) of lines, we analyzed separately the features detected in the two states. In Fig. 3.5 the distributions of the detected emission and absorption features as a function of their observed-frame energy are reported; each bin is 0.2 keV wide. The vertical dotted line represents the nominal energy of the Fe K α emission and is shown only as a visual reference, since in the current analysis this feature is already included in the model as a narrow emission line (see Sect. 3.1.1). The occurrences of the features are normalized to the number of analyzed spectra, 56 for the unobscured case and 32 for the obscured case. Interestingly, the energy of the detected emission and absorption lines seems to cluster around certain values. Starting with the emission lines, in the unobscured data we recognize a small peak in the distribution (corresponding to a total of 8 detections in time-resolved spectra) at the energy of the K β /ionized K α line, corresponding to the K β /ionized K α blend. In the obscured state (Fig. 3.5, bottom-left), most of the detected lines are clustered between ~ 5.6 keV and ~ 6.4 keV. For the absorption features, most of the detections cluster between ~ 6.4 keV and ~ 7 keV. While no major difference is observed in the distribution of clustered features in unobscured and obscured observations, there seems to be a slight shift towards higher energies in the obscured datasets.

3.3 Simulations

To assess the statistical significance of the individual lines, we followed the indications reported by Protassov et al. (2002) and Vaughan and Uttley (2008). In particular, after a preliminary assessment by evaluating the $\Delta\chi^2$ for the 3 Δ d.o.f. of the detected line (energy, normalization, width), we used Monte Carlo techniques to compute the number of times a line at a given energy and significance is found by chance in simulated, featureless spectra. In doing so, we took advantage of what we found in real data: in fact, the detected features we are looking for in the simulations do not appear to be random fluctuations, that could be positive or negative, but lines clustered in determined regions of the spectrum, bound to be strictly positive or negative. We thus tested separately emission and absorption lines.

To probe the different source states, we analyzed separately the unobscured and obscured epochs, because of their intrinsic diversity, and for each epoch we made a selection in X-ray flux, identifying low, medium and high-flux states. For the 2000/2001 datasets, the flux ranges are 2.50–3.09, 3.09–3.68, 3.68–4.27 $\times 10^{-11}$ erg s $^{-1}$ cm $^{-2}$, while for the 2016 dataset the three flux intervals are 1.42–1.80, 1.80–2.19, 2.19–2.57 $\times 10^{-11}$ erg s $^{-1}$ cm $^{-2}$, respectively. We determined a best-fit

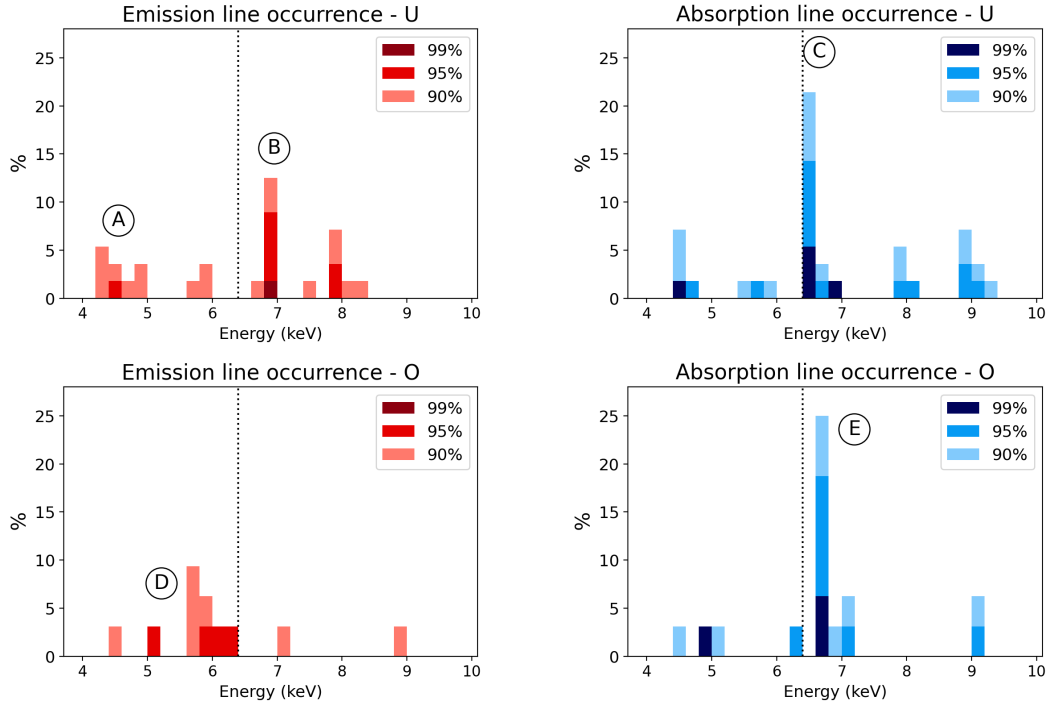


Figure 3.5: The distribution in energy (observed frame) of the features detected via blind search. The energy bins are 0.2 keV wide. The top panels show the results of the unobscured dataset (U1, U2a, U2b, U3), while the bottom panels refer to the obscured datasets (O1, O2). On the left panels, detections of emission lines are reported (red), while the right panels report detections of absorption lines (blue): in both cases, the darker the color the higher the significance, i.e. the measured $\Delta\chi^2$. The percentage on the y axes is the ratio between the number of detections in each bin and the total number of spectra for the two sets of observations (56 in total for the unobscured, and 32 in total for the obscured). The dotted line reported in all four figures is the nominal energy of the Fe $K\alpha$ and is shown purely as a visual reference. The letters A-E indicate the clusters of lines that globally reach a significance $\gtrsim 3\sigma$, as indicated in Table 3.1 and described in Sect. 3.3.

baseline model (using the same continuum model defined in Sect. 3.1) for each of these groups of spectra (six in total), and used it to simulate 1000 spectra for each group. Simulated spectra are grouped at 1/5 of the instrument energy resolution. We first apply and fit the baseline model and record the obtained best fit χ^2 . Then a second Gaussian component is added. Since in real data the detected lines appear to cluster at specific energies, we analyzed the energy bands 4-6 keV, 6-8 keV, and 8-10 keV separately in simulated spectra. In particular, the fitted line energy is forced to vary within each of these intervals, and its width is free to vary in the range 0.01–0.5 keV. Emission and absorption features are searched separately. To adopt a conservative approach, for each cluster of features we finally counted how many of the 1000 trials show a $\Delta\chi^2$ higher than the lowest value found in the actual data. This does automatically translate into a robust estimate of the significance of each of the detected lines. Results are shown in Table 3.1.

We find that both emission and absorption lines do not reach a high significance in the unobscured dataset and that they tend overall to be more significant during the obscured phase. We also find that the flux state does not seem to have a direct effect on the significance of the features. If we take into account their occurrences and calculate the binomial probability, their significance increases sensibly, as shown in Tab. 3.1, where the most significant groups of features are identified with the A-E letters in the last column. The global probability that the absorption lines detected in the 6-8 keV range are not fluctuations is $\gtrsim 4\sigma$ for both source states (C, E). As for the emission lines, their estimated significance is $\gtrsim 3\sigma$ in the 4-6 keV range in all the observations (A, D), and 4σ in the 6-8 keV band during the unobscured state (B).

The transient/variable nature of the detected features is naturally inferred from the fact that they are detected only in a fraction of our time-resolved spectra.

3.4 Residual Maps

The blind search can accurately detect features in each time bin and provides information about their possible repeated appearances at different times during the entire observations. It is not immediate, though, to understand the evolution in time of such features just from the blind search results: an easy way to trace it is to represent these features in a time-energy plane. This approach was first introduced by Iwasawa et al. (2004) and later used in several studies (e.g. Turner et al. 2006; Tombesi et al. 2007; De Marco et al. 2009; Nardini et al. 2016; Marinucci et al. 2020). Since we have studied the presence of emission and absorption features simultaneously, we decided to visualize them altogether (hence the passage from *excess* to *residual* maps in the denomination).

In order to visualize the data uniformly, we have to choose first an energy

Energy keV	$\Delta\chi^2$ $\sigma_{single}^{(1)}$ %	MC $\sigma_{single}^{(2)}$			$\sigma_{group}^{(3)}$ %	
		Low %	Mid %	High %		
Unobscured						
Emission						
4-6	91	94	92	92	99.3	A
6-8	91	94	93	93	>99.9	B
8-10	91	92	90	91	91.0	
Absorption						
4-6	92	90	91	88	87.0	C
6-8	91	90	88	89	99.9	
8-10	90	87	83	80	91.0	
Obscured						
Emission						
4-6	95	97	96	96	>99.9	D
6-8	96	99	99	98	99.0	
8-10	94	96	96	95	65.0	
Absorption						
4-6	97	97	96	97	93.0	E
6-8	92	91	93	92	>99.9	
8-10	96	96	95	95	74.0	

Table 3.1: Significance of detected variable features: (1) significance of single features calculated from the $\Delta\chi^2$ for 3 Δ d.o.f. measured after the addition of a Gaussian line in emission/absorption; (2) significance of single features from MonteCarlo simulations (Low/Mid/High refer to the different selected flux levels, defined in Sect. 3.3); (3) global significance of detected features (i.e. calculated from a binomial distribution, and assuming the total number of spectra in each state as the number of trials, the number of detections obtained via the blind search as the number of successes, and the mean value from MC simulations as the success probability for each trial). The letters A-E refer to the groups of features with a significance $> 3\sigma$, as indicated in Sect 3.3 and displayed in Fig. 3.5. Their nature is discussed in Sect. 3.6.

resolution for the maps. To have sufficient statistics, we impose a minimum of 20 photons in each $\Delta t \cdot \Delta E$ pixel. Having already selected $\Delta t = 5$ ks (see Sect. 2.2), we can adopt $\Delta E = 100$ eV, which is approximately equal to the EPIC pn energy resolution at high energies and allows us to collect >20 photons per time-energy pixel at all times, except for energies higher than 9 keV in the first half of O1 (where the flux is at its minimum, as shown in Fig. 3.1). However, with the blind search we already found that we are not able to detect significant features in this range for the obscured dataset, therefore we decided to limit our analysis to the data below 9 keV for the RM analysis.

Fig. 3.6 shows the RM produced applying the baseline model described in Sect. 3.1 fitted in the total energy range. This procedure is fairly different from what is usually done in excess maps (e.g. Iwasawa et al., 2004; De Marco et al., 2009), where the continuum is typically modeled using only narrow energy bands of the spectrum where no major discrete features are expected to be observed (see Sect. 3.5). As for the blind search, however, we found that the oversimplification of the modeling/fitting may introduce too strong systematics also in the production of the maps (see, for example, the differences between the maps shown in Fig. 3.6 and in Fig. 3.9).

From a visual inspection of the RM, it is possible to see that the features detected in Sect. 3.2 (and listed with A-E letters in Table 3.1) are present also in the maps, and evidently exhibit intensity variability on short time-scales probed by the RM. Nevertheless, we do not find any clear/obvious macro pattern of variability.

The most evident features in the RM are, of course, those that are most conspicuous in the histograms in Fig. 3.5. The recurrent absorption feature detected via the blind search is clearly recognizable as a blue stripe at ~ 6.5 keV in the unobscured datasets (C), with a varying intensity on short (~ 10 ks) time-scales. This absorption line gets wider and shifted in energy up to ~ 6.7 - 6.9 keV in the obscured dataset (E). It is interesting to see that, in the RM, this feature seems to appear far more often than in the histograms, where it reaches a maximum frequency of $\sim 25\%$: this is because in the blind search we set the detection threshold at 90%, whereas the maps show all the residuals with $|\Delta\chi| > 1$, that correspond to a lower significance, approximately 68%.

The emission features related to the neutral Fe $K\beta$ /ionized Fe $K\alpha$ are visible in the 2000/2001 observations as an irregular sequence of shallow red spots around ~ 7 keV (B). The recurrent emission features in the lower energy band (4-6 keV) also appear shallow and irregularly distributed in the unobscured dataset (A), while in the obscured one they are mostly clustered above 5 keV (D), as especially clear in O1. These results will be discussed in Sect. 3.6.

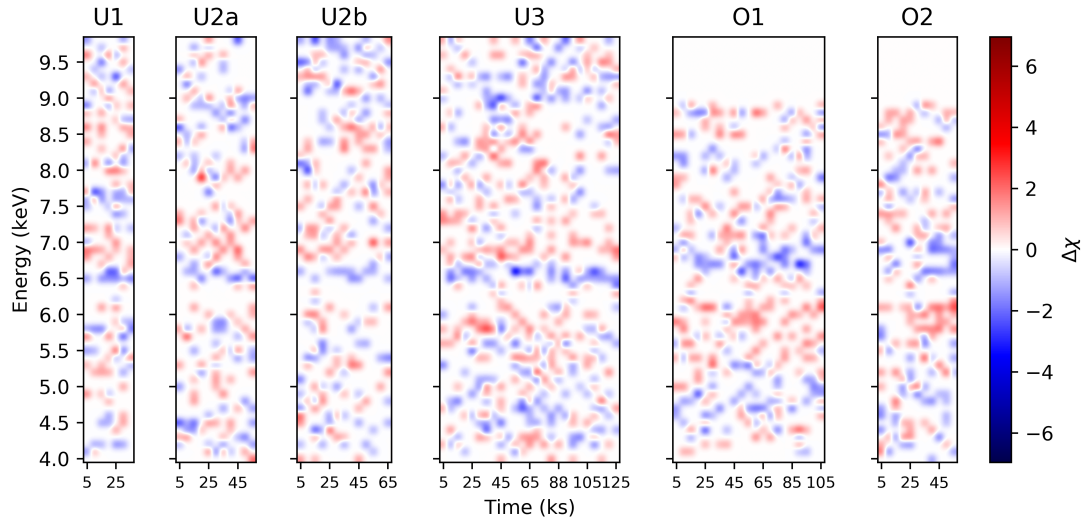


Figure 3.6: Residual maps produced with the baseline model `pcfabs × (power law + gauss)`. The time bin size is 5 ks, while the energy resolution is 0.1 keV. Each pixel shows the value of $\Delta\chi$ (i.e. residual/data error, in red for the positive and in blue for the negative residuals) to give an estimate of the significance, even though the RM are meant to be used here as a qualitative way to identify patterns, rather than a tool to estimate the significance of each feature. A Gaussian interpolation is applied to the pixels to highlight the features and facilitate the identification of possible patterns. The area at $E > 9$ keV of both O1 and O2 are purposely left blank as the threshold of 20 photons per pixel is not met because of the low flux (see Sect. 3.4). The horizontal lines highlight the energy bands of most significant groups of features, indicated in Fig. 3.5 and in Tab. 3.1.

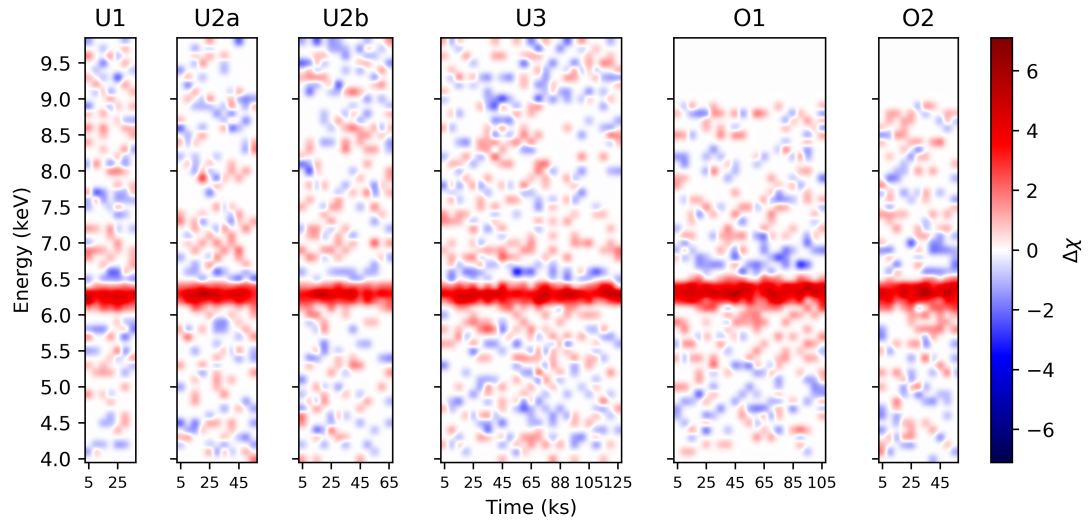


Figure 3.7: Residual maps including the narrow Fe $K\alpha$ component, produced as described in Sect. 3.4.1. These residuals are produced by fixing the baseline model at its best fit values for each spectrum and then removing the Gaussian component.

3.4.1 Fe $K\alpha$ line residuals

The RM shown in Fig. 3.6 provide information about all possible lines in the 4–10 keV band except for the narrow component of the Fe $K\alpha$, as it is fitted in each spectrum, so the residuals are null by default. Even though its variations in energy, EW, and width are already shown in Fig. 3.2 and Fig. 3.3, it would still be interesting to see them along with the other features, to highlight possible relations. Hence we produced a new set of RM, where we fitted the baseline model described in Sect. 3.1, froze all the parameters of the absorber and of the power law at their best values, then removed the line component, and finally plotted the $\Delta\chi$. These RM are shown in Fig. 3.7. The strong emission feature at ~ 6.4 keV is always present, but the darker and lighter spots seem to indicate some variability. Given the results obtained from the fits of our baseline model (Sect. 3.1), the observed variations in the RM can be ascribed to a combination of the variations of EW and width of the Fe $K\alpha$ emission line (Fig. 3.2, bottom panel; Fig. 3.3). Indeed, the energy binning is different between the spectra and the maps (with a nominal ratio of $\sim 1/5$), therefore also the width can influence the value of the $\Delta\chi$ in the maps. This is evident when considering the four Fe K peaks in the RM of O2, which coincide with the increase of line width as seen in Fig. 3.3. The possible origin of this behaviour will be discussed in Sect. 3.6.2.

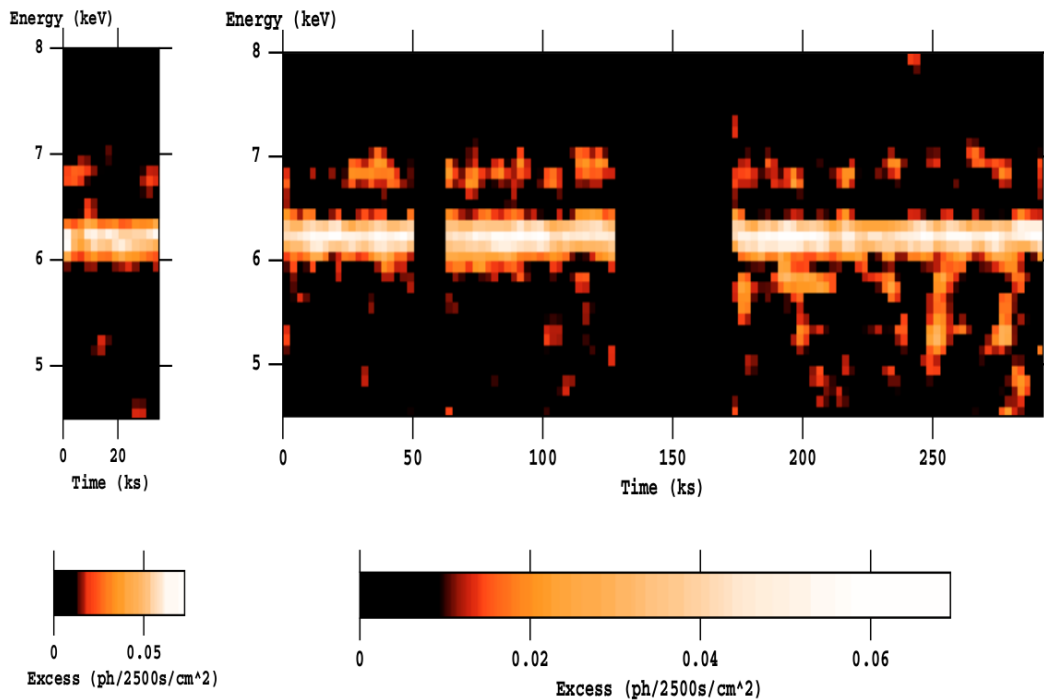


Figure 3.8: Excess maps of observation U1-3. Credit: Tombesi et al. (2007).

3.5 Residual maps and Excess maps

Our residual maps have been produced in a slightly different fashion than those described by Tombesi et al. (2007). Aside from the major step of employing all of the residuals, positive and negative, and not only the positive ones, we used a different fitting procedure.

To study the emission features, Tombesi et al. (2007) modelled the continuum as a power law plus a cold absorption component fixed to be equal to the value measured in analysing the average spectrum. Then they fitted the continuum considering the 4–5 keV and 7–9 keV band to avoid the Fe $K\alpha$ line. Their original maps are shown in Fig. 3.8. In order to make a direct comparison, we produced a set of residual maps following their procedure. They are shown in the top row of Fig. 3.8. Since we were actually interested in following the variations of the absorption features, produced indeed by the absorber, we produced another set of RM with the same fitting band and model, this time leaving the column density free to vary in each spectrum. They are displayed in the bottom panel of Fig. 3.9.

While these two sets of maps do not show significant divergences between each other, as indeed predicted by Tombesi et al. (2007), the difference among them and those we presented in Fig. 3.7 is quite evident. The absorption features we found at ~ 6.6 – 6.9 keV are only marginally present in the RM in Fig. 3.9. Instead,

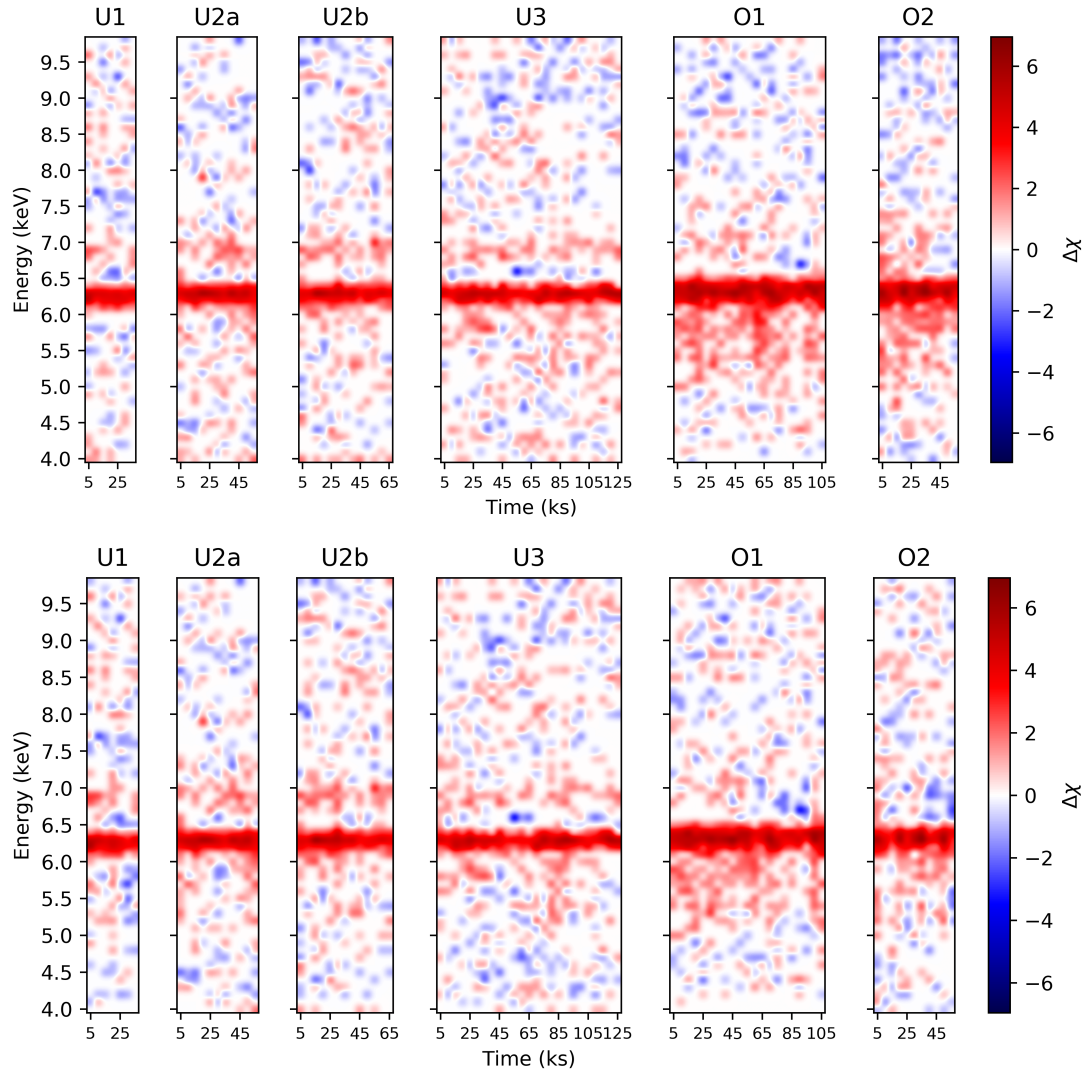


Figure 3.9: RM produced using a power law plus total covering cold absorption fitted only in the 4–5 keV and 7–10 keV energy bands, following the indications of Tombesi et al. (2007). The value of the column density of the absorber is fixed to the value measured in average spectra in top panel maps and free to vary in the bottom panel ones.

the excess at energies below the Fe $K\alpha$ line appear to be far more intense and, in particular, in U3 we find the strong feature discussed by Tombesi et al. (2007). It is to be noted that the normalisation (colour) of the residual maps is the same for all sets.

The first difference between the production of the maps shown in Fig. 3.7 and those in Fig. 3.9 is the energy band used to fit the model. The use of the complete 4–10 keV range, without excluding the Fe $K\alpha$ band, allows for a better anchorage of the continuum, and this could be at the base of the divergence of the sets of maps. Then we analysed the continuum parameters: in the top left panel of Fig. 3.10 we plotted the best fit parameters for the absorber column density and the power law photon index. To quantify the relation among them, we calculated the Pearson Correlation Coefficient ρ for the two epochs, and obtained $\rho_U = 0.78$ and $\rho_O = 0.88$, both corresponding to a correlation probability higher than 5σ . This degeneracy between these two parameters disappears when using the partial covering baseline model, described in Sect. 3.1. Its best fit parameters are plotted in the top right panel of Fig. 3.10, and the correlation probability calculated for these data drops at 21% for the unobscured epoch ($\rho_U = -0.04$) and 17% for the obscured one ($\rho_O = 0.04$). On the one hand, it is worth considering that we are in any case dealing, by construction, with limited statistics. That means that also our approach is prone to introduce some systematics, as seen in the bottom panels of Fig. 3.10. This is somehow inevitable given the experimental condition that we are using. On the other hand, we already knew that our baseline model provides a limited description of the complex absorption that is known to occur in NGC 3783 (M17; Mao et al. 2019). Far from our scopes, we are not investigating here in detail the characteristics of the various ionized absorbers that have been previously reported in literature; we want to stress here is that at least part of excesses recorded between 5–6 keV are possibly explained by the simplified absorption scheme used in producing RM. A significant step forward in time-resolved spectral studies will be possible with X-ray telescopes with larger effective area, which would allow us to probe short timescales (i.e., by using short time slices) without losing energy resolution. Specifically, the X-IFU on-board Athena (Nandra et al., 2013; Barret et al., 2018) in the foreseeable future will provide a major advance in the research field described in this work.

3.6 Results and discussion

Through our analysis, we searched for and identified absorption and emission features in the interval 4–10 keV that are variable on short time scales in NGC 3783. We investigated how these features change between the two states of the source.

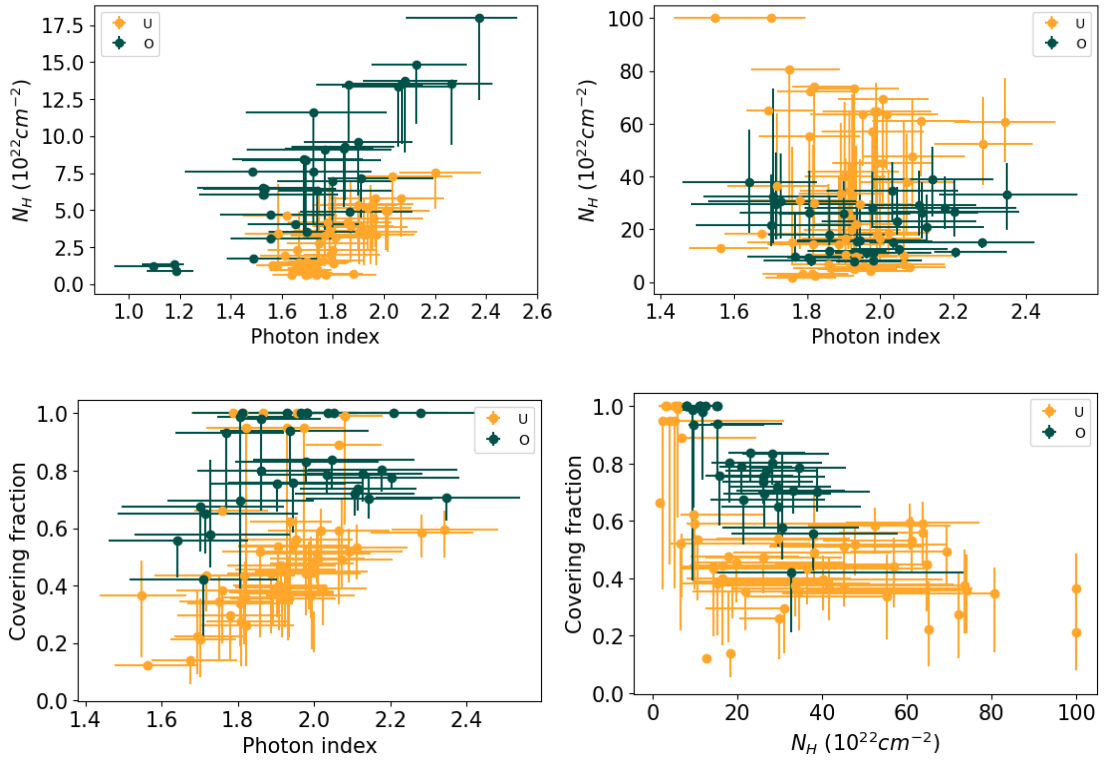


Figure 3.10: Top left panel: column density of the total covering cold absorption vs power law photon index, fitted only in the 4–5 keV and 7–10 keV energy bands. The correlation among the values is assessed at $\gg 5\sigma$ for both the unobscured and obscured epoch. Top right panel: column density of the partial covering cold absorption vs power law photon index, fitted in the 4–10 keV energy range. The degeneracy between the two parameters is not present in this case, with a correlation probability $\lesssim 20\%$. Bottom left panel: covering fraction of the partial covering absorber vs power law photon index. Bottom right panel: covering fraction vs column density of the absorber. Data relative to unobscured and obscured epoch are reported in yellow and green, respectively.

Features in emission: As displayed in the top left panel of Fig. 3.5 (B), about 15% of the spectra during the unobscured epochs (2000/2001) show the presence of emission features with a significance $\geq 90\%$ around 7 keV. This corresponds to a global statistical significance of the detections of $\sim 4\sigma$ (Table 3.1). Conversely, during the obscured epochs the number of detections and their significance drops: we observe only one feature, detected at a significance of $< 3\sigma$. This cluster of emission lines in the unobscured epoch can be identified as either the neutral Fe K β line or an additional ionized Fe component found at ~ 6.9 –7 keV. This identification is supported by the ratio between the residuals at ~ 7 keV and those at ~ 6.4 keV, that is about a factor 3 larger than what we would expect in the case of a pure Fe K β ($\sim 1/9$; Molendi et al. 2003). The additional contribution to the emission features at ~ 7 keV may come from the same ionized medium producing the absorption features. The same conclusion is given in R04. This excess is far less visible, if not absent, in the obscured dataset, as we would expect from the results of M17, who suggested that a juxtaposition with a Fe XXVI Ly α absorption line cancels out the emission feature.

The other notable cluster of emission features (though individually less significant) is seen in the obscured observations at 5–6 keV (A, Fig. 3.5, bottom-left panel), is clearly visible in the corresponding RM (see Fig. 3.6). This is detected to be more variable/sporadic in the 2000/2001 dataset (D). The nature of these features will be discussed in Sect. 3.6.1. The U3 data were previously analyzed using the excess map technique by Tombesi et al. (2007) with a different fitting procedure (described below). They report variability and modulation of a putative red and relativistically broadened wing of the Fe K line. In their scenario, the modulation was possibly due to the formation of spiraling arms within the accretion flow. It is worth noting, however, that the presence of this broad feature is not strongly supported by the analysis of the time averaged spectrum (R04). The recurrent, red-shifted feature reported in Tombesi et al. (2007) appears less prominent in our RM. This is probably due to the difference in the assumed baseline model (we assume a partial covering model for the continuum, rather than a totally covering one). Moreover, when fitting the continuum, we include a narrow Fe K α line in the model, rather than excluding the energy range where it contributes the most.

Features in absorption: The most recurrent features measured in almost $\sim 25\%$ of all the spectra are seen in absorption, between 6.7–6.9 keV (C and E in Fig. 3.5). This absorption component is clearly visible also in the RM (see Fig. 3.6). This is in agreement with results of R04 and M17. We also confirm that the feature’s energy shifted by ~ 200 eV, from ~ 6.7 to ~ 6.9 keV, between the unobscured and obscured datasets (see Fig. 3.5). Taking into account

the calibration problems highlighted in Sect. 3.1.1, the net energy shift of the absorption line is more likely of ~ 150 eV. The absorption line at 6.7 keV is observed throughout all the unobscured observations, which span a period of about one year. Nonetheless, R04 reported a change in the EW between U2 and U3. However, it is worth noting that their analysis is most probably more sensitive to slight variations of the average values, while our analysis is more focused on searching variability on shorter time scales. Interestingly, we confirm the absence of UFOs in this source (Tombesi et al., 2010). The results of the blind search in the energy band 8-10 keV are, in fact, consistent with what expected for pure casual events (see Table 3.1).

3.6.1 Possible Fe $K\alpha$ broadening during O1 and O2

To explain the origin of the group of emission features detected at $\geq 4\sigma$ in the obscured epoch in the 5-6 keV energy range (bottom-left panel of Fig. 3.5) and clearly visible in the corresponding RM (last two panels of Fig. 3.6), we propose two different scenarios.

The first one ascribes it to the presence of the absorber. It may be an effect of the oversimplification of the fitted continuum model, meaning that ignoring the absorption lines and absorption edges due to the presence of an ionized absorber alters the whole continuum, occasionally resulting in excess emission redward of the Fe $K\alpha$ line. Another possibility in the same scenario is that the bump is produced by variations in the partial covering fraction happening on times shorter than our time resolution (Iso et al., 2016). This scenario is furthermore supported by the fact that in the unobscured epoch, where the absorber has a lower column density and is less ionized (R04) the features are detected at a lower significance and at lower energies (top left panel of Fig. 3.5).

The other scenario is that these features are real, and associated with a relativistic wing of the neutral Fe $K\alpha$ line. To explore this option, we tested a relativistic model on the emission line detected at 6 keV in the 12th 5ks spectrum O1, which we use as a test because of its significant broadening of $\sigma = 260^{+130}_{-120}$ eV (Fig. 3.3). We added a `laor` component (Laor, 1991) to our baseline model, that already accounts for the narrow Fe $K\alpha$. The outer radius and emissivity index are unconstrained, so they are fixed to their default values of $400R_g$ and 3, respectively. The excess is well reproduced ($\Delta\chi^2 = 18.3$ for 3 Δ d.o.f.) by a signal emitted from $R_{in} = 99 \pm 52 R_g$. At such distance, the Keplerian velocity is ~ 30000 km/s, corresponding to a FWHM of ~ 0.64 keV for the neutral Fe $K\alpha$ line at 6.4 keV. Thus, we do not expect to see much significant emission associated with it below ~ 6 keV, were we indeed detect the majority of emission lines (group D, bottom-left panel Fig. 3.5). If those features were real, they could be emitted from the base of the obscuring wind, as it could be expected following the models in Dehghanian et al. (2020).

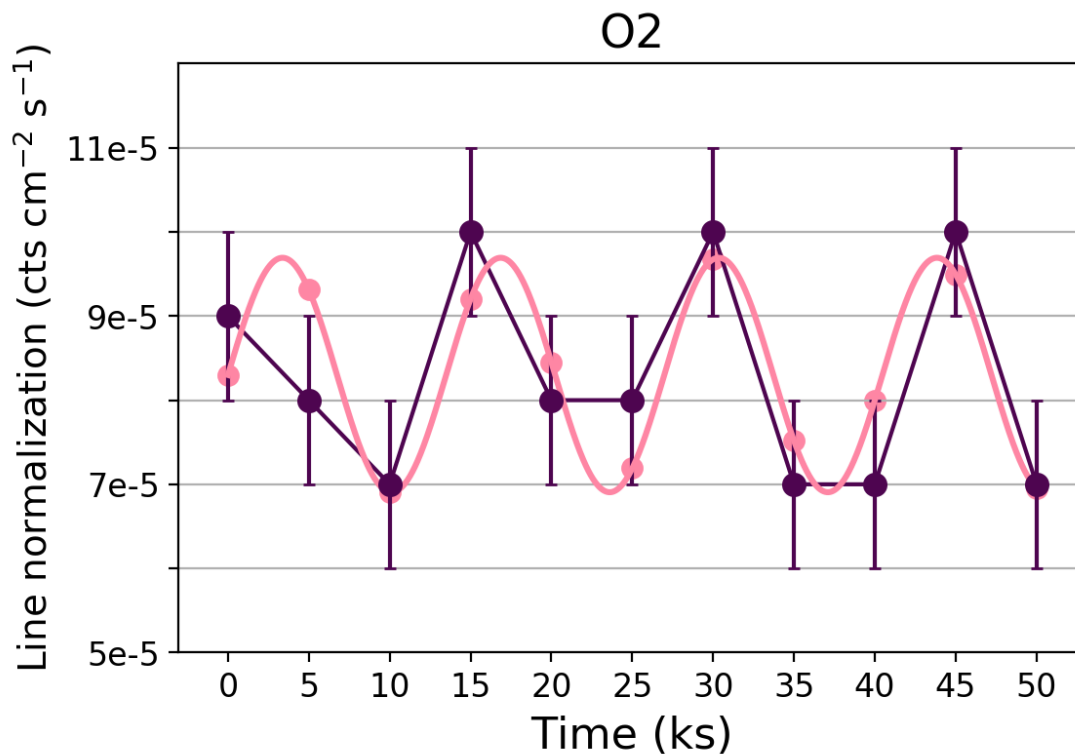


Figure 3.11: Tentative fitting of a sinusoid to the variations of the normalization of the Fe $K\alpha$.

3.6.2 Fe $K\alpha$ modulation in O2

In the residual maps of the latest observation (O2; Fig. 3.7) there are four quite evident peaks in the principal Fe $K\alpha$ line component. It is to be noted that their presence does not show a correlation with the 4 – 10 keV light curve (last panel in Fig. 3.1), so the line is not simply following an intrinsic continuum variation. The normalization of the narrow Fe $K\alpha$ line, as obtained from time-resolved spectral fitting of O2, is plotted in Fig. 3.11. This is tentatively fit with a sinusoidal function. The fit yields $\chi^2 = 5.3$ for 9 dof (11 data-points and 2 free parameters, period and normalization). This corresponds to a significance of 90%, thus not supporting the detection of a modulation. However, it is worth noting that even if a modulation is indeed present, the small number of sampled variability cycles (~ 4) would significantly reduce the significance of the signal.

The sinusoidal fit yields a best-fit value of 13 ± 8 ks for the putative period. This would correspond to a Keplerian orbit at ~ 6 R_g. At such small distances we would expect prominent relativistic effects on the Fe $K\alpha$ line, which are not observed. Therefore, we conclude that the observed variations are most likely not

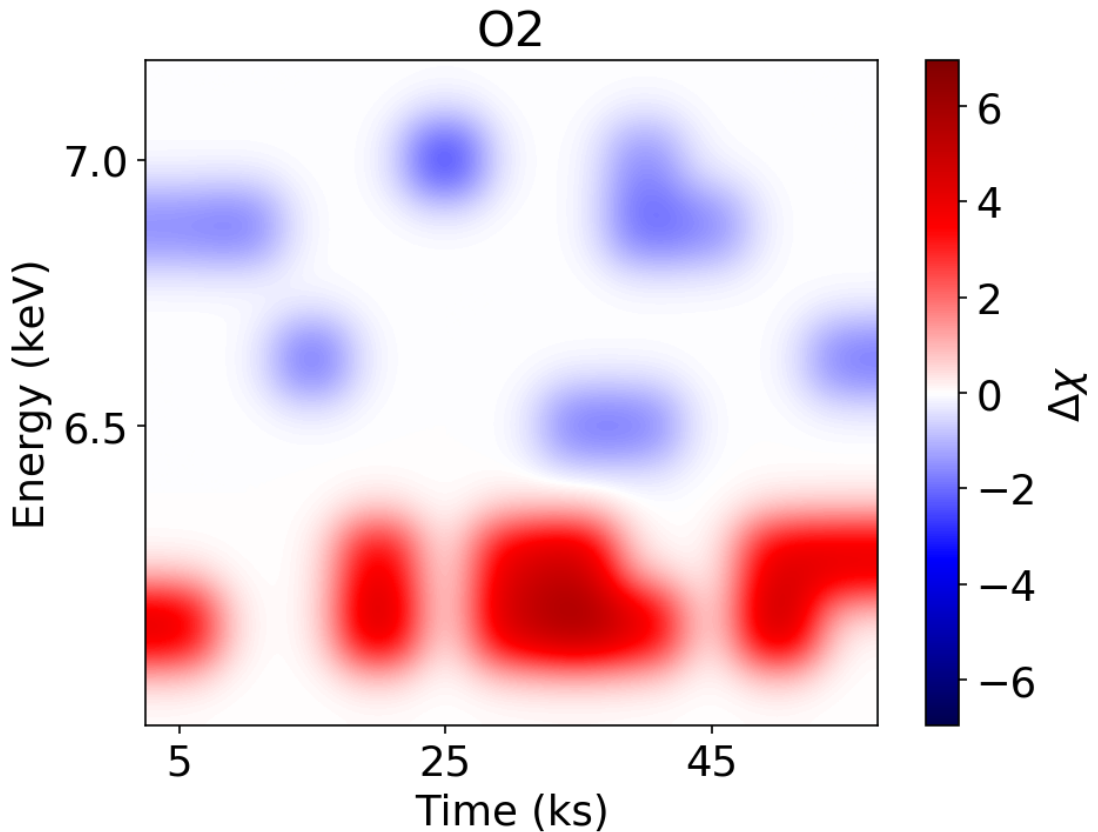


Figure 3.12: Residual map of O2 where we set a higher threshold in terms of $\Delta\chi$ to qualitatively highlight the possible link between the peaks of the Fe $K\alpha$ emission line (in red) and the most intense absorption dips (in blue).

associated with a modulation of the Fe $K\alpha$.

Interestingly, the intensity of the narrow Fe $K\alpha$ line seems to decrease simultaneously with the appearance of the absorption features at 6.7-6.9 keV, as highlighted in Fig. 3.12. This suggests a relation between the two. In M17 the absorption features are ascribed to a highly ionized ($\log \xi \cong 3.8$) clumpy medium outflowing at few thousand of km s^{-1} in the broad line region. This high-ionization component is likely associated and spatially coexistent with the obscurer producing the eclipsing event, which has a lower ionization parameter of $\log \xi \cong 1.8$. A gas with this value of ξ could actually produce resonant absorption lines at energies consistent with the Fe $K\alpha$ for ionized species from Fe X up to Fe XX (Kallman et al., 2004). In this case, the dips observed in the emission line would correspond to a partial absorption at that energy. This explanation is similar to that reported in M17 for the disappearance of the Fe $K\beta$ emission line; the main difference is

that in the case of the Fe $K\alpha$ line the emission feature is not completely suppressed because of its intrinsically higher normalization. In this scenario we can use the duration of the dips (and the absorption features at higher energy) to constrain the size of the clumps of the obscurer. If each clump has a large opacity, we can assume an "on/off" effect due to their passage through the line of sight. Using the distance and velocity values found in M17 for the obscurer, $\sim 7-10$ light days from the X-ray source (few $10^3 R_g$), with an orbital velocity of $\sim 3500 - 4200 \text{ km s}^{-1}$, and considering the duration of the dips to be from 5ks to 10 ks, we can estimate the clumps extent to be in the range $\sim 1.7 - 4.2 \times 10^{13} \text{cm}$.

While the peaks in O2 are the most evident, Fig. 3.7 shows that the intensity of the neutral Fe $K\alpha$ emission line varies also in other observations. For O1 we can assume that the lower ionization component is the same as in O2 (M17), and since the Fe $K\alpha$ line dips have the same duration of 5-10 ks we obtain the same results on the clumps sizes.

In the unobscured epoch, R04 reports the presence of three different absorbing components at different ionization levels. Among them, the medium with $N_H \cong 4.4 \times 10^{22} \text{ cm}^{-2}$ and $\log \xi \cong 3$ can possibly absorb part of the neutral Fe $K\alpha$ emission line. The entity of this absorption is actually consistent with the variations we measure in the normalization of the line (a few percents of its value), it is to be noted though that this quantity is also of the same order of magnitude of the error of the parameter. However if we hypothesize the variations to be real, we measure dips with a duration between 5 ks and 20 ks. With a distance of $\sim 2 \times 10^{17} \text{cm}$ (R04), assuming a keplerian orbit we find the size of the clouds in the range $0.7 - 2.8 \times 10^{11} \text{cm}$. The dimensions of the clouds in both epochs are consistent with those found in the BLR of NGC 1365 by Risaliti et al. (2009).

Chapter 4

NGC 3227

NGC 3227 is a Seyfert 1.5 galaxy at redshift $z=0.00386$ (de Vaucouleurs et al., 1991). This source has been showing evidence for variability in the X-rays since the first observations with *HEAO1* (Tennant and Mushotzky, 1983), and again when observed with *EXOSAT* (Turner and Pounds, 1989) and *ASCA* (Ptak et al., 1994). It was subject to a sustained monitoring with RXTE from January 1999 to December 2004 (Uttley and McHardy, 2005). During this campaign the source underwent two distinct eclipsing events: the first one, in 2000-2001, lasted ~ 80 days (Lamer et al., 2003), and the second one, in 2002, lasted $\sim 2 - 7$ days (Markowitz et al., 2014). The hardness ratio measured during the entire RXTE monitoring is shown in Fig. 4.1, adapted from Markowitz et al. 2014. The yellow shadows highlights the two eclipsing events.

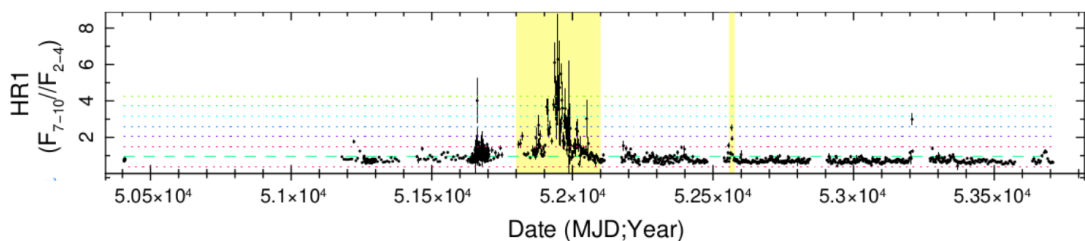


Figure 4.1: Hardness ratio measured during the RXTE monitoring of NGC 3227, lasting from January 1999 to December 2004. The areas shaded in yellow highlight the two eclipsing events in 2000-2001 (Lamer et al., 2003) and in 2002 (Markowitz et al., 2014). Credit: Markowitz et al. 2014.

In 2016 NGC 3227 was the target of a joint campaign of *XMM-Newton* and NuSTAR, that observed the source simultaneously six times during a period of one month. In that period, NGC 3227 showed yet another eclipsing event that lasted approximately one day, and was attributed to a partially covering, ionized cloud outflowing from the inner BRL at few $\sim 10^2$ km s $^{-1}$ (Turner et al., 2018). Spectral-timing studies of the same observations found a strong variability, which could be most likely ascribed to changes in the primary X-ray source, and a typical softer-when-brighter behaviour (Lobban et al., 2020). A monitoring program, started in 2015 with *Swift*, detected an intense spectral hardening lasting a few weeks from November 2019 and triggered two *XMM-Newton* observations that revealed the source to be in a heavily obscured phase (Mehdipour et al., 2021).

We analyzed all the observations of NGC 3227 available in the *XMM-Newton* archive, for a total of 10; the OBS ID of each pointing and the corresponding denomination are reported in Table 4.1. Among them, five show the source in an unobscured state (and are indicated with an “U”) and 3 in an obscured one

Obs ID	Start date	Label
0101040301	2000-11-28 18:15:41	O1
0400270101	2006-12-03 01:53:31	O/U1
0782520201	2016-11-09 12:51:03	U1a,U1b
0782520301	2016-11-25 10:25:35	U2
0782520401	2016-11-29 13:10:38	U3
0782520501	2016-12-01 09:58:49	U4
0782520601	2016-12-05 09:42:23	U5
0782520701	2016-12-09 09:24:49	O/U2
0844341301	2019-11-15 09:15:10	O2
0844341401	2019-12-05 22:10:30	O3

Table 4.1: OBS ID of all the observations of NGC 3227 analyzed in this work and relative denominations used.

("O"), while two caught it exactly in a "changing" phase, with the beginning of the observation obscured and the end unobscured (and are indicated with "O/U"). During data reduction, U1 resulted to be split in two parts, separated by ~ 15 ks. The light curves are displayed in Fig. 4.2, and the spectra in Fig. 4.3 As evident, O1 and O3 show the source in an extremely low state, with a flux ~ 3 times lower than in the rest of the observations. In order to avoid losing the higher time resolution we would be able to achieve in the majority of the observations, we decided to extract and analyze spectra of different duration: 13.5 ks for O1 and O3, and 5 ks for the rest. These lengths were chosen to guarantee a minimum of 5000 photon in each spectrum, considering the minimum count rate in the band 5 (4.5–12 keV) of the 4XMM-DR11 catalogue, 0.368 ± 0.004 ct s $^{-1}$ and 1.042 ± 0.006 ct s $^{-1}$ for the two flux regimes, respectively. Given the black hole mass of $0.5 \times 10^7 M_{\odot}$ (Bentz and Katz, 2015), the period of a Keplerian orbit at $10 R_g$ is 4.9 ks, $\sim 10 R_g$ being the distance where the most powerful winds are supposed to be launched from Proga (2007). The observational limitation in flux allows us to reach this distance from the SMBH but not to oversample it.

All the spectra are binned using the task `ftgroupppha` with grouping option "optimal" (Kaastra and Bleeker, 2016), the fitting and the blind search are performed using C-statistics (Cash, 1979).

4.1 Fe K α line

To fit the spectra, we use the same baseline model tested for NGC 3783 and described in Sect. 3.1. It consists of a power law, a partially covering neutral

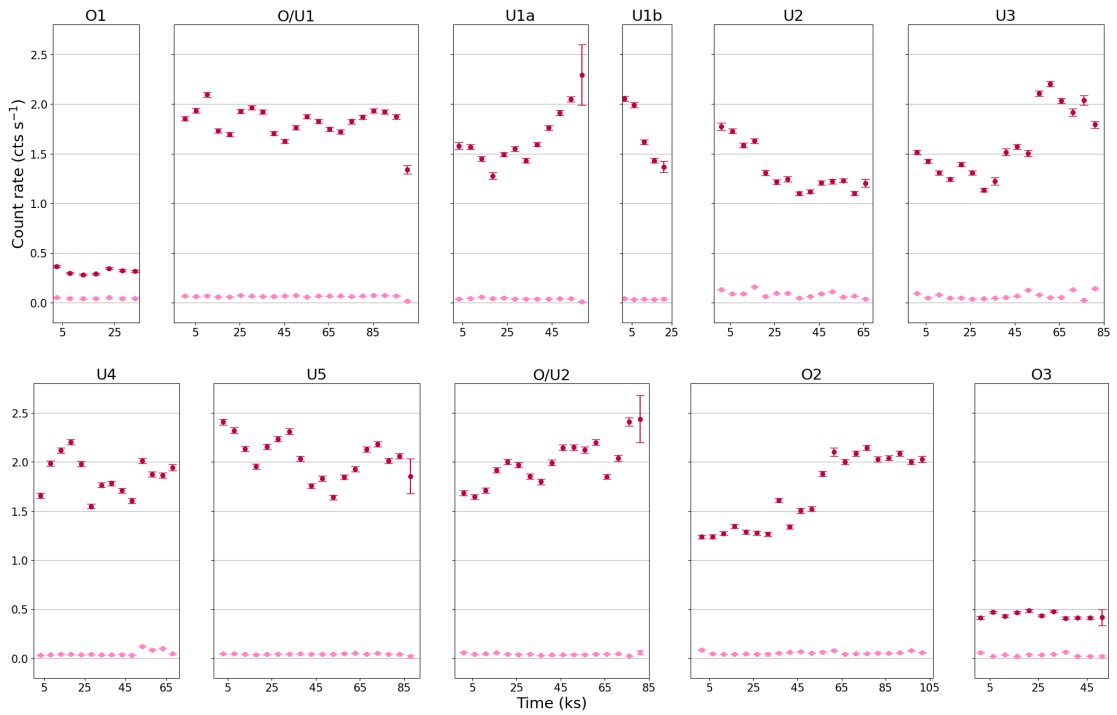


Figure 4.2: Light curves of all the observations of NGC 3227 between 4-10 keV, with time bins of 5 ks.

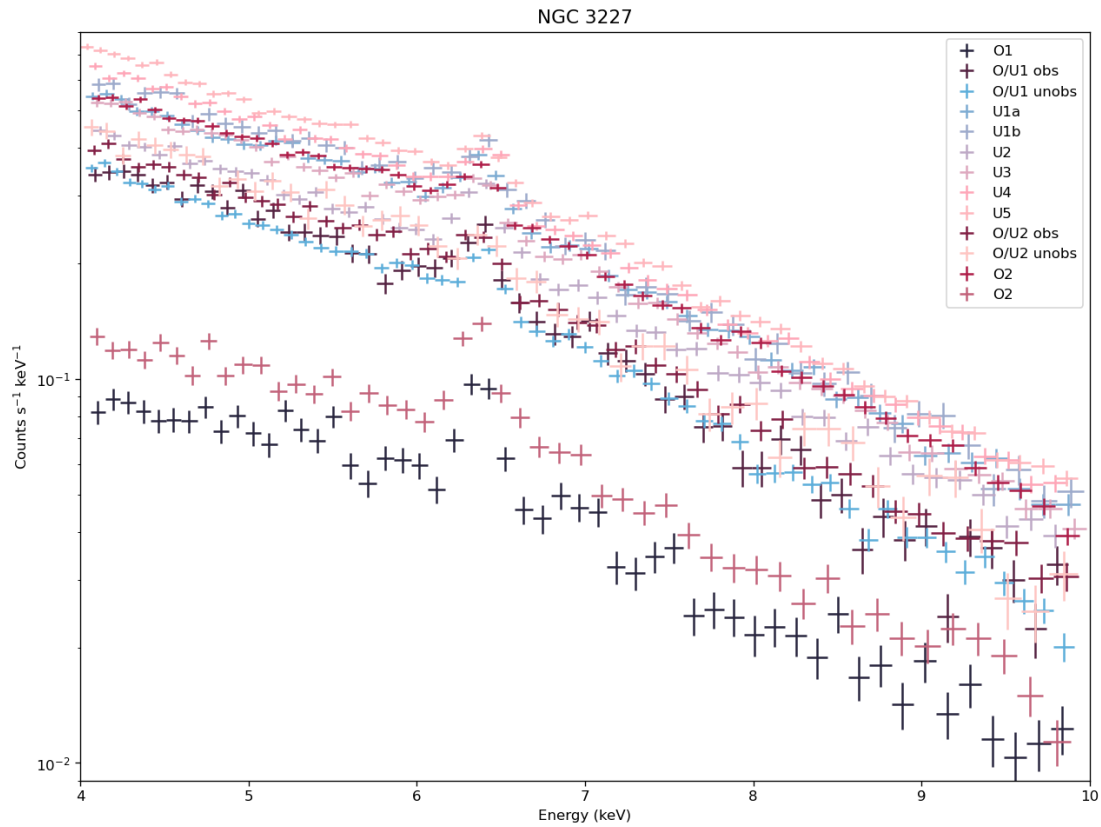


Figure 4.3: Average spectra of all the analyzed observations of NGC 3227. For O/U1 and O/U2, we split the obscured and unobscured parts and show them separately.

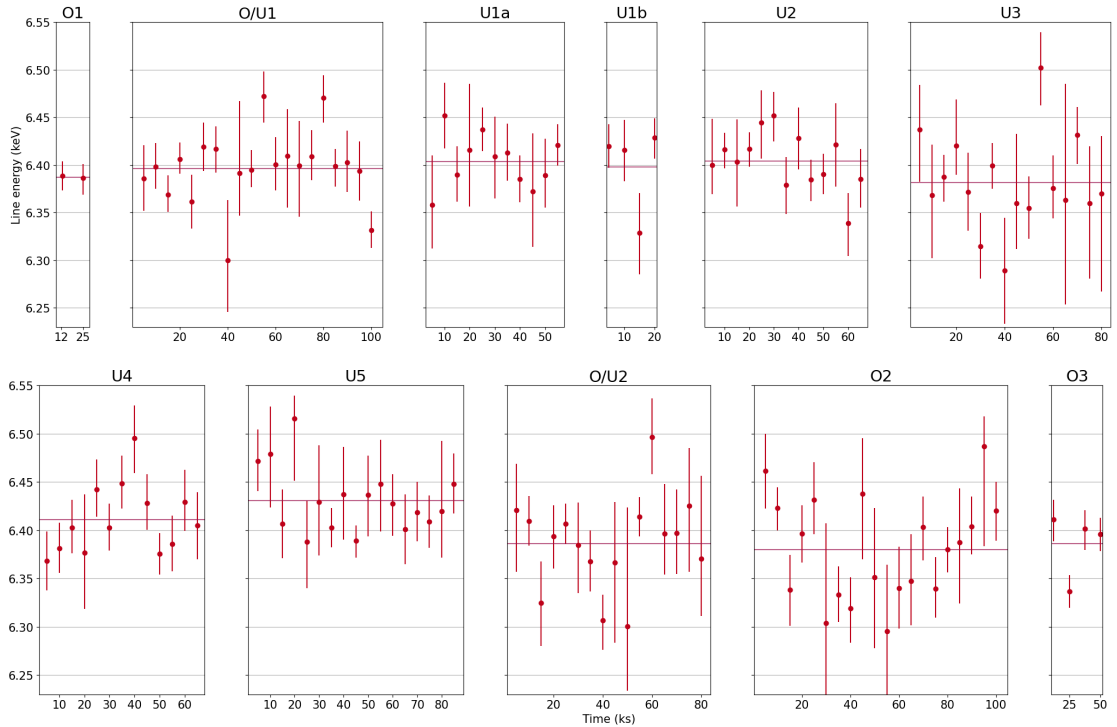


Figure 4.4: Rest-frame energy of the narrow Gaussian emission component accounting for the Fe $K\alpha$. The horizontal line represents the average value within each observations. Errors are reported at 1σ .

absorber and a narrow ($\sigma = 10$ eV) Gaussian emission line to account for the narrow Fe $K\alpha$ component that is present in the spectrum, as reported in literature (e.g. Lobban et al., 2020). In Fig. 4.4, 4.5, and 4.6, we show the best-fit values of the energy, normalization, and EW of the Fe $K\alpha$. Starting from the energy, we see that the average values of each observations (displayed as the horizontal line in Fig. 4.4) are consistent, within the uncertainties, with values spanning from ~ 6.38 to ~ 6.43 keV and 1σ errors of the order of ~ 10 eV on each data-point. As for the short time-scales, we register a few variations on times as short as the time bins (5 ks and 13.5 ks for O1 and O3), for example in O/U1, U1b, U3, and O3. In Fig. 4.5, we display the normalization of the line. Lobban et al. (2020) indicated variations of the order of 20%, ascribed to the variations of the underlying continuum. We confirm these results, not finding episodes of major variability. The same trends visible in the normalization are also present in the EW except for O1 and O3: in these two observations, the equivalent width is a factor ~ 3 higher than in the other pointings, in accordance with the decrease by the same order of the flux visible in Fig. 4.2: this indicates an intrinsic stability of the Fe $K\alpha$ line, placing its origin in a reflector distant from the primary X-ray source, that at these times is

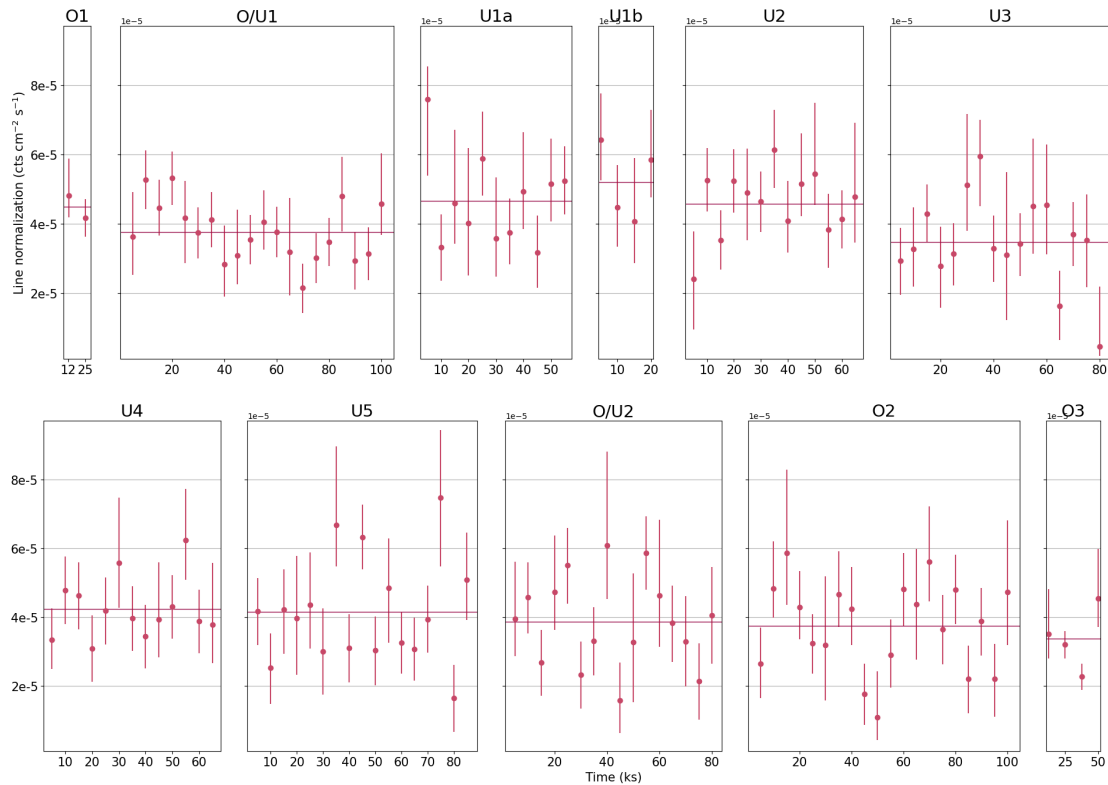


Figure 4.5: Normalization of the Fe $K\alpha$ line. Errors are reported at 1σ .

absorbed by the obscurer, as reported in [Lamer et al. \(2003\)](#) and [Mehdipour et al. \(2021\)](#).

4.2 Blind search and simulations

To search for transient, discrete features, we run a blind search on all the spectra and follow the same procedure described in Sect. 3.2: we add a Gaussian line to the baseline model and, using the `steppar` command on Xspec, we find the combinations of normalization and energy that improve the fit by 11.34, 7.81, 6.25 ΔC , corresponding to a 99%, 95%, 90% significance for 3 Δ d.o.f. (energy, width, normalization of the line). We have a total of 130 spectra of 5 ks, among them 90 correspond to the unobscured state and 40 to the obscured one. As for the observation that caught the change of state, we followed the indications of [Wang et al. \(2022\)](#) and considered for O/U1 the first 20 ks obscured and the rest unobscured (so 4 and 16 spectra, respectively), and for O/U2 the first 60 ks obscured and the rest unobscured (12 and 4 spectra, respectively). We also have 6 spectra of 13.5 ks, extracted from observations O1 and O3 that caught the

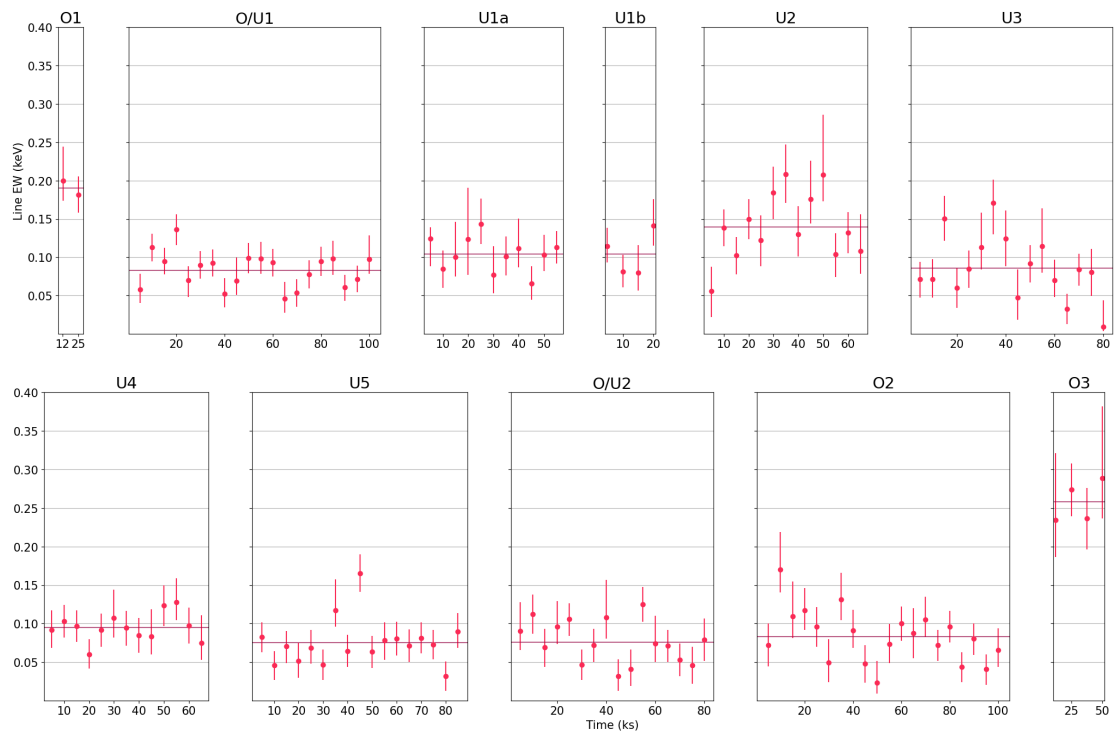


Figure 4.6: Equivalent width of the Fe $K\alpha$ line, with 1σ errors. The drops by a factor ~ 3 in O1 and O3 are due not to an intrinsic variability of the line but to the decrease in flux of the same order, visible in Fig. 4.2.

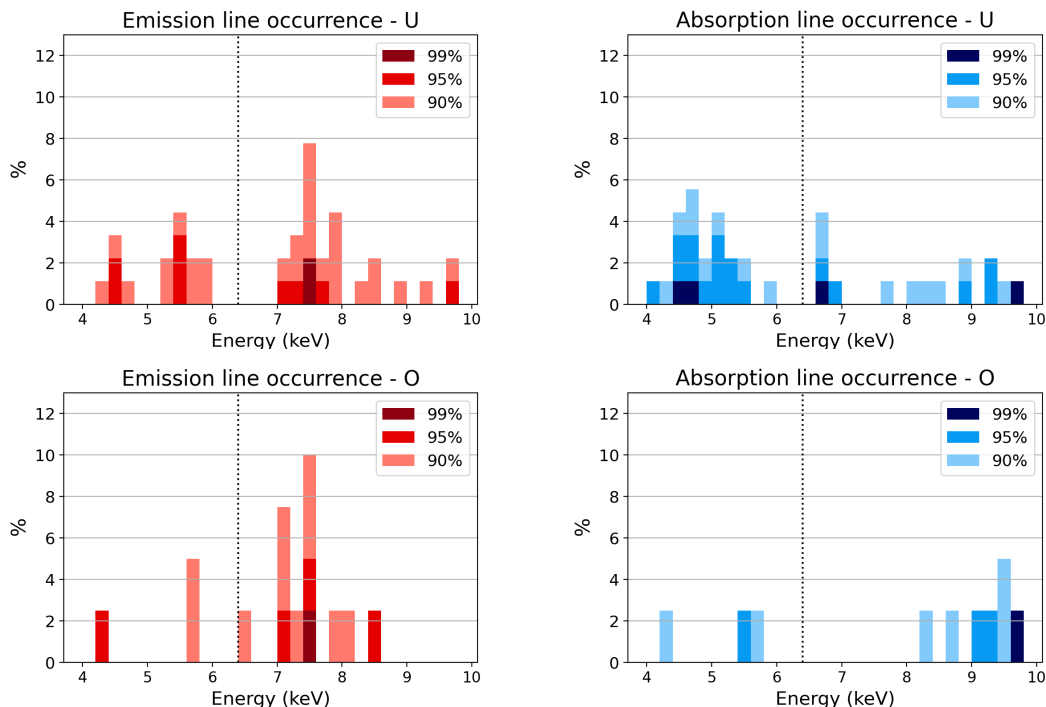


Figure 4.7: Energy distribution of the emission and absorption features detected via the blind search.

source in an exceptionally low state of flux, as displayed in Fig. 4.2. The energy distribution of the lines detected in the 5 ks spectra are reported in Fig. 4.7. We chose to consider separately the low-flux observations because the time scales, and therefore the analyzed corresponding regions around the SMBH, are different. We detected no features in the 4 spectra extracted from O3, and two features are found in the first spectrum extracted from O1: they are reported in Fig. 4.8.

To assess the significance of the single detected features, we ran MonteCarlo (MC) simulations. We considered three flux regimes for both the states of the source, selected by dividing in three equal parts the entire flux range observed. For the unobscured state, the band limits are 1.42–1.97, 1.97–2.53, 2.53–3.08 $\times 10^{-11}$ erg s $^{-1}$ cm $^{-2}$; for the obscured state, they are 1.58–2.01, 2.01–2.43, 2.43–2.86 $\times 10^{-11}$ erg s $^{-1}$ cm $^{-2}$. For each flux band, we found the average best-fit model and carried out 1000 simulations. Then we counted how many features were found with a significance $> 90\%$, meaning with $\Delta C > 6.25$, both in emission and in absorption, for each energy band. The results from the MC simulations are reported in Table 4.2.

Interestingly, for the unobscured spectra we register a significant difference between the results from the simulations for the low-flux regime, that mostly

Energy keV	MC σ_{single}			σ_{group} %
	Low %	Mid %	High %	
Unobscured				
Emission				
4-6	70	92	88	-
6-8	70	92	91	-
8-10	70	90	92	-
Absorption				
4-6	92	92	87	-
6-8	67	92	81	-
8-10	69	87	92	-
Obscured				
Emission				
4-6	89	92	56	-
6-8	92	93	92	≥ 99.7
8-10	89	90	90	-
Absorption				
4-6	94	92	79	-
6-8	-	-	-	-
8-10	91	91	94	≥ 95

Table 4.2: Results of the MC simulations on the significance of the detections at different energy ranges, in different flux regimes. The significance for single detections is higher than the threshold of 90% only for emission features at E=6–8 keV, and absorption features at E> 8 keV, both in the obscured state of the source. For these two cases, we calculated the global significance of the groups of detections with the binomial probability distribution.

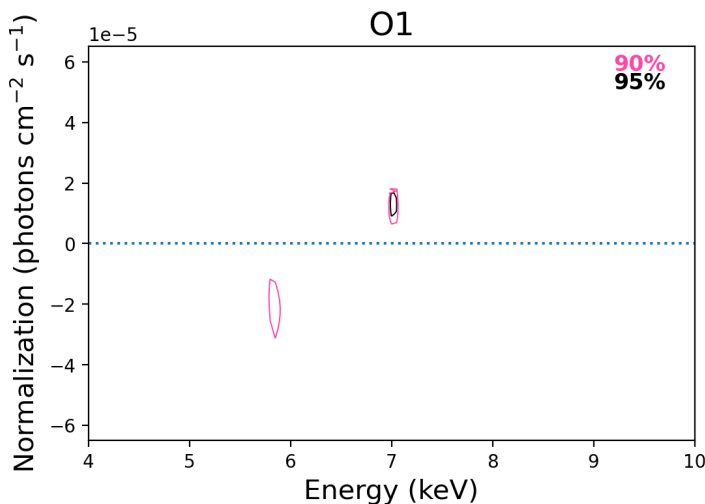


Figure 4.8: Significance contours of the features detected via blind search in the first spectrum of O1.

reach a significance of $\gtrsim 1\sigma$, and for the middle and high regime, where the significance is stable at $\sim 90\%$, therefore consistent with what directly expected from the blind search. As for the obscured spectra, we find two cases in which the detections have a significance $\geq 90\%$ in all flux regimes: the emission lines at 6–8 keV, and the absorption lines at 8–10 keV. The occurrences of these features are 10 in emission with a MC significance larger than 92%, and 7 in absorption with MC significance larger than 91%, considering a total of 40 spectra in the obscured state. We estimate the probability that their repetitions are not casual by using the binomial distribution. Given the total number of trials (40 spectra), the "minimum" significance (92 for the emission lines and 91 for the absorption ones), and the number of successes (i.e. of detections, 10 emission lines and 7 absorption lines) we find a global significance of $\sim 3\sigma$ and $\sim 2\sigma$ respectively.

4.3 Residual maps

We produced the residual maps for all observation analyzed for NGC 3227, shown in Fig. 4.9, by using the same procedure described in Sect. 3.4.1: once we find the best-fit of the baseline model, we remove the **Gauss** component accounting for the Fe $K\alpha$ and plot the residuals normalized by the error without re-fitting, then we put together the residuals of all the spectra within a single observation in the time-energy plane. We use 0.1 keV as energy resolution uniformly throughout the whole map. The time resolution is 5 ks for all plots, except for O1 and O3.

Observing the maps, the most evident feature is, as expected, the Fe $K\alpha$ line.

In the maps it is possible to visualize altogether the energy and the intensity of the line, that are reported separately in Fig. 4.4 and Fig.4.5. We stress here that the maps provide a magnification of the variations, and that they do not provide any form of uncertainties of the displayed values. The residual maps clearly report the variations in energy of the line, for example the shift at lower energy at the end of O/U1 and in the middle of O/U2 and O2. The changes in normalization are shown in the maps as redder points (peaks) or lighter ones (dips). The iron line is presented here as rather uneven: this is particularly evident, for example, towards the end of U3, and in U5, O/U2 and O2. As detailed above in Sect. 4.1 and displayed in Fig. 4.5, some of these variations are indeed significant, for example the ~ 10 ks dip in the middle of O2. Among all the features detected with the blind search, the only ones which have been confirmed with a significance $> 90\%$ using the MC simulations are in the obscured state and are the emission lines at 6-08 keV and the absorption lines at 8-10 keV. We remind here that the first 20 ks (4 spectra) of O/U1 and the first 60 ks (12 spectra) of O/U2 are categorized as obscured (Wang et al., 2022). These features are recognizable in the maps. It is particularly interesting to discuss the origin of the absorption features at high energies. We can interpret them as an effect of the presence of UFOs (Tombesi et al., 2010), therefore Fe resonant absorption lines produced by highly ionized material; considering the energy of the detections ($\sim 8.2 - 9.8$ keV), we find an outflowing velocity $> 0.2c$. We note here that O1 and O/U1 are part of the sample analyzed by Tombesi et al. (2010); while we confirm the absence of UFOs in O1, we have some hints of detection of lines at ~ 9.0 keV and at ~ 9.2 keV in the first and third spectra extracted from O/U1: it is possible that, because of the transient nature of these lines, they were evened out in the analysis of the whole spectrum, and therefore not detected in their work. In particular, we tested if the "strip" of possible absorption lines visible in the residual map of the first/obscured 20 ks of O/U1 are indeed indicating the presence of a highly ionized feature. Fig. 4.10 show the spectra fitted with the baseline model and, in addition, a narrow (10 eV) absorption line, for which the best fit values are $9.17^{+0.04}_{-0.03}$ keV for the energy and $-7 \pm 2 \times 10^{-6}$ cts s $^{-1}$ cm $^{-2}$ for the normalization, with error at 90%. The EW of this line is 0.06 keV and its presence improves the fit by 8.9 for 2 Δ d.o.f. We did not try the same exercise on the O/U2 observations, since the residuals map of this pointing does not show any possible pattern of systematic behaviour of the possible features.

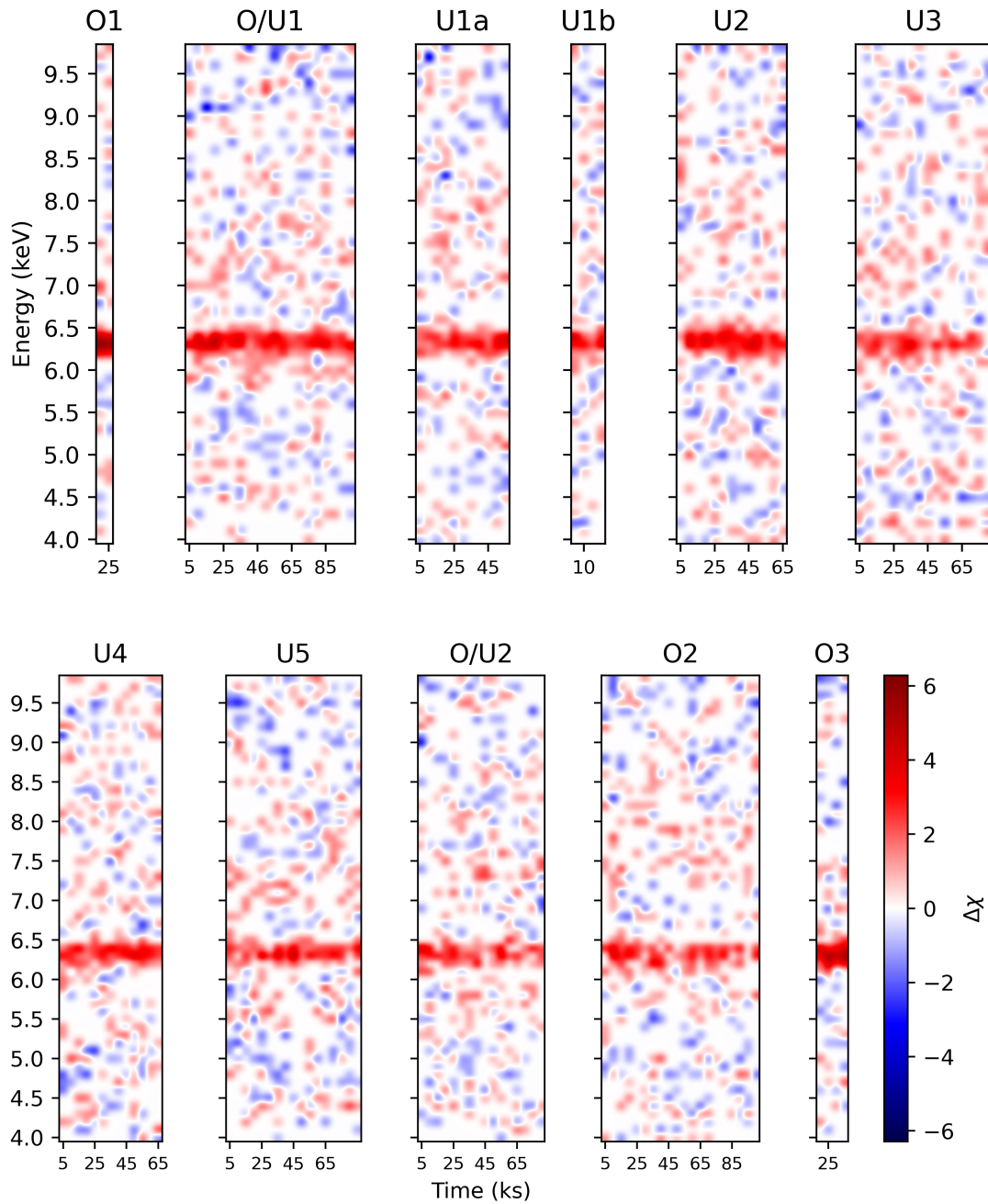


Figure 4.9: Residual maps of the observation of NGC 3227 analyzed. Time bins are 5 ks for all observations except for O1 and O3, where it is 13.5 ks. In the first four spectra O/U1 it is possible to recognize the hint of UFO detection at ~ 9.2 keV, detected at 2σ that disappears in the rest of the observation as the obscuration event ends and is not detectable when only the average spectrum is analyzed.

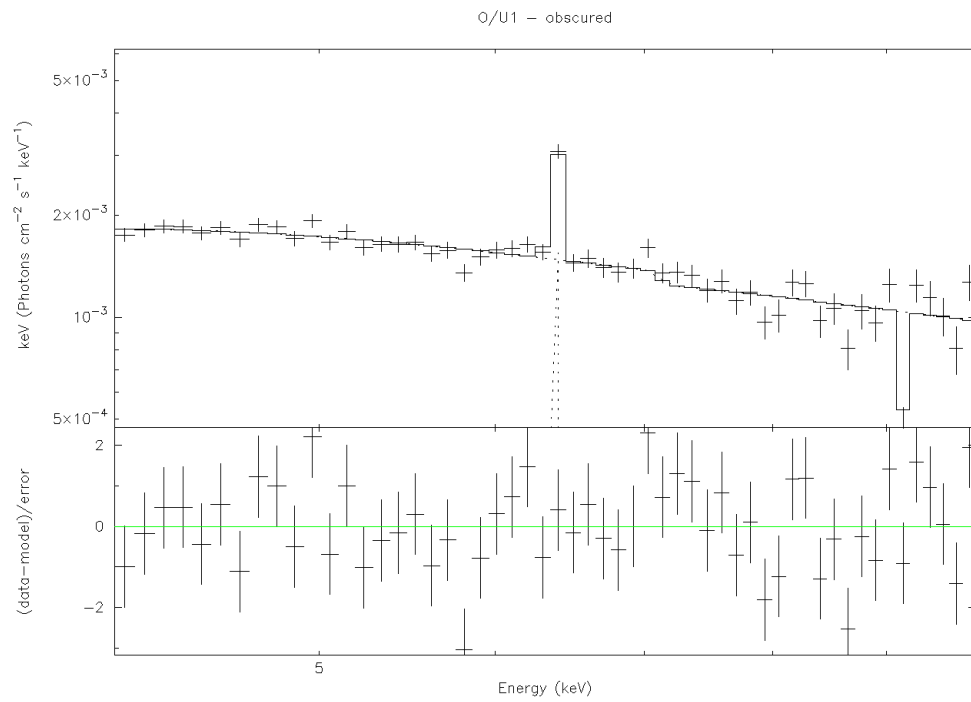


Figure 4.10: Spectrum extracted from the first 20 ks of observation O/U1, during the obscured phase. At ~ 9.2 keV the absorption line produced by the UFO is visible in the model, the significance is 2σ .

Chapter 5

NGC 5548

NGC 5548 ($z=0.017175$, de Vaucouleurs et al. 1991) was part of the original sample of twelve extra-galactic nebulae with high-excitation emission lines in the central area compiled by Seyfert (1943). It was the first source in which the narrow absorption lines produced by the warm absorbers in the X-rays were discovered, using the high-energy resolution of the spectrometers on-board Chandra (Kaastra et al., 2000). A reverberation mapping campaign in 2008 brought an accurate description of the BLR (Pancoast et al., 2014), shaped as a narrow, thick disk with inclination angle $\sigma = 38.8_{-11.4}^{+12.1}$ deg and a mean radius $r=3.31_{-0.61}^{+0.66}$ light days. Until recent years, it was considered an archetypal Seyfert 1 galaxy (Bianchi et al., 2009).

In 2013-2014, it was the target of a multi-wavelength observational campaign that collected over 2.4 Ms of X-ray and 800 ks of optical/UV observation time among different observatories (*XMM-Newton*, *Swift*, NuSTAR, INTEGRAL, *Chandra*, HST COS, Wise Observatory, and Observatorio Cerro Amazonas). At this time, the source was caught in an obscured state, blocking 90% of the soft X-ray emission and simultaneously producing deep, broad absorption features in the UV (Kaastra et al., 2014). The obscuration is ascribed to a clumpy, weakly ionized gas located at 2–7 light days from the center of the system, partially covering the primary X-ray source and the BLR, outflowing with velocities up to 5000 km s^{-1} . A cartoon representing the position of the obscurer is displayed in Fig. 5.1 Archival data from *Swift* show that the obscuration event started somewhere between August 2007 and February 2012.

We analyzed all the available observations present in the XMM-Newton archive, 19 in total; their OBS ID and the denominations used here are reported in Table 5.1. Their lightcurve are shown in Fig. 5.2 and the spectra in Fig. 5.3. Among them, three caught the source in the unobscured state (U1-3) and sixteen in the obscured state (O1-16). The minimum count rate in the band 4.5–12 keV reported in the 4XMM-DR11 catalogue for this source is 0.745 ± 0.005 , therefore in order to have at least 5000 photons in each spectrum, we selected 7 ks as the size of the time bins for the time-resolved spectral analysis: this gives us 17 spectra in the unobscured state and 108 in the obscured one. Considering a mass of $4.8 \times 10^7 M_{\odot}$ for the SMBH (Bentz and Katz, 2015), the orbital period at $10 R_g$ is 47 ks, thus we are able to oversample it and each of our time bins represents a fraction of 0.15 of it. All the spectra are binned using the task `ftgrouppha` with grouping option “optimal” (Kaastra and Bleeker, 2016), the fitting and the blind search are performed using C-statistics (Cash, 1979).

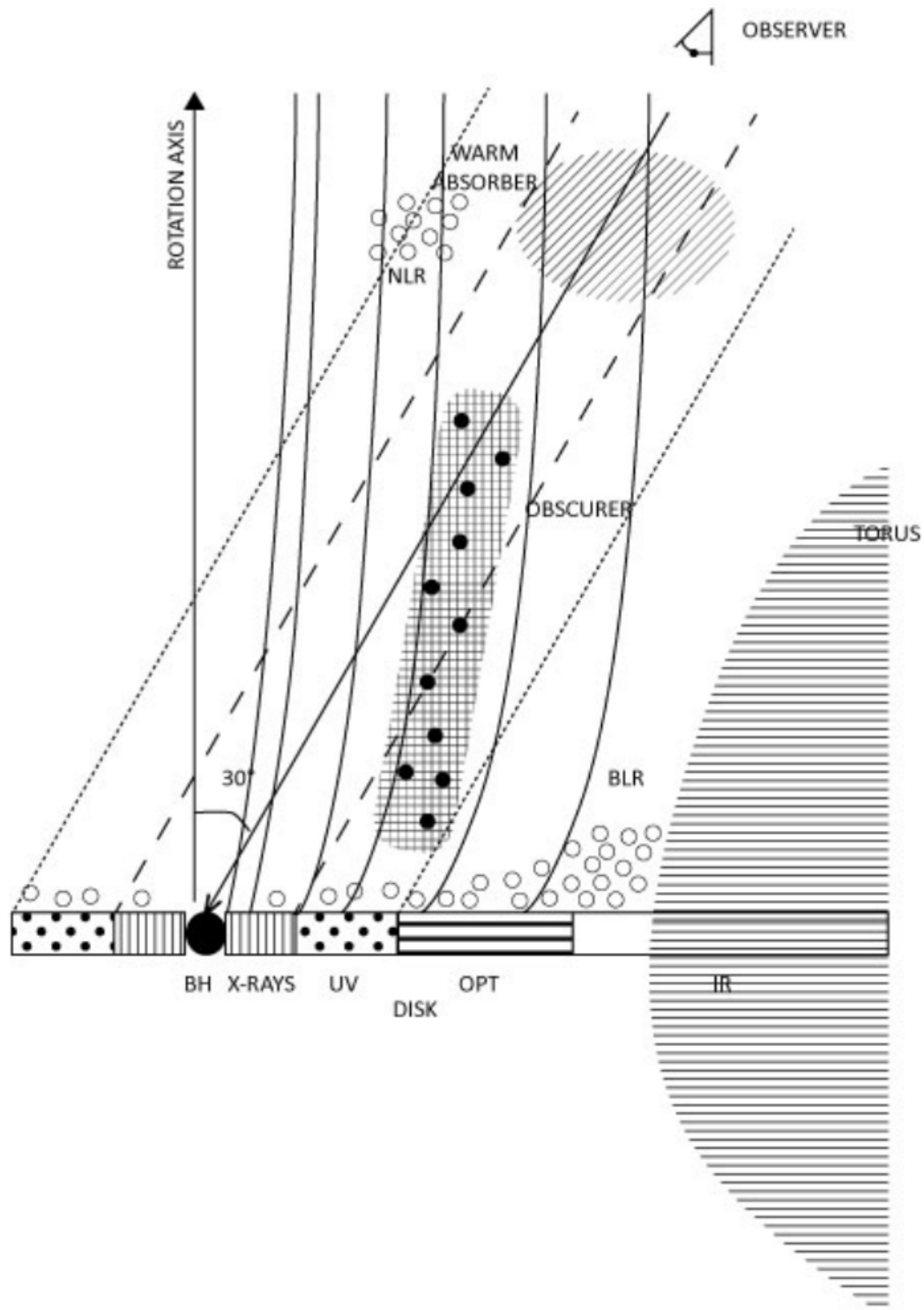


Figure 5.1: Cartoon of the central region of NGC 5548 (not to scale). The obscurer consists of a mixture of ionized gas with embedded colder, denser parts and is close to the inner UV BLR. Credit: [Kaastra et al. 2014](#).

Obs ID	Start date	Label
0109960101	2000-12-24 22:12:11	U1
0089960301	2001-07-09 15:45:59	U2
0089960401	2001-07-12 07:34:56	U3
0720110301	2013-06-22 04:10:29	O1
0720110401	2013-06-29 23:50:30	O2
0720110501	2013-07-07 23:28:42	O3
0720110601	2013-07-11 23:11:43	O4
0720110701	2013-07-15 22:56:29	O5
0720110801	2013-07-19 22:40:42	O6
0720110901	2013-07-21 22:32:18	O7
0720111001	2013-07-23 22:24:17	O8
0720111101	2013-07-25 22:15:00	O9
0720111201	2013-07-27 22:06:35	O10
0720111301	2013-07-29 21:58:06	O11
0720111401	2013-07-31 21:49:48	O12
0720111501	2013-12-20 14:01:39	O13
0720111601	2014-02-04 09:33:43	O14
0771000101	2016-01-14 05:52:27	O15
0771000201	2016-01-16 06:36:31	O16

Table 5.1: OBS ID of all the observations of NGC 5548 analyzed in this work and relative denominations used.

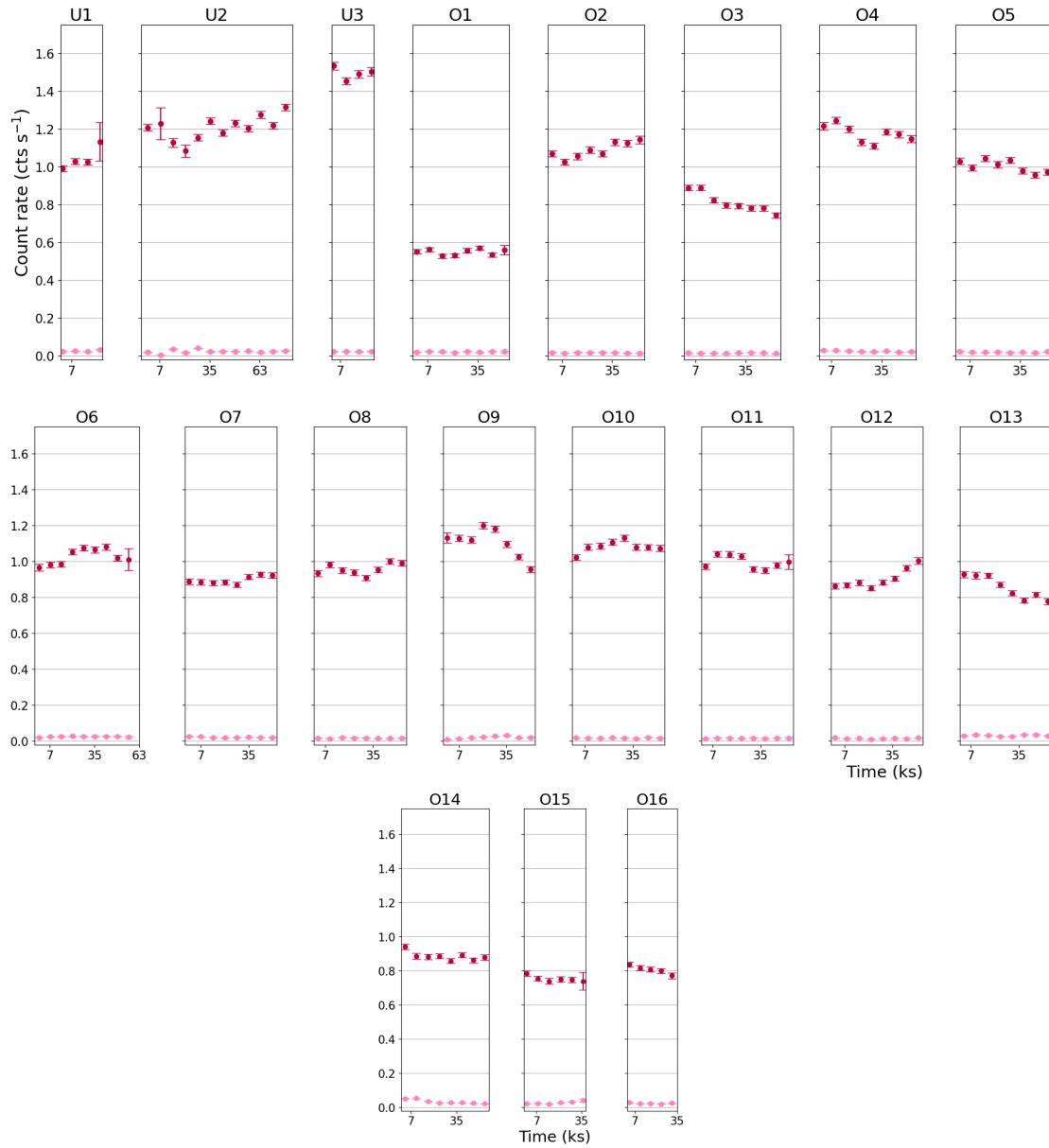


Figure 5.2: Light curves of all observations of NGC 5548 in the 4–10 keV energy range, time bins are 7 ks.

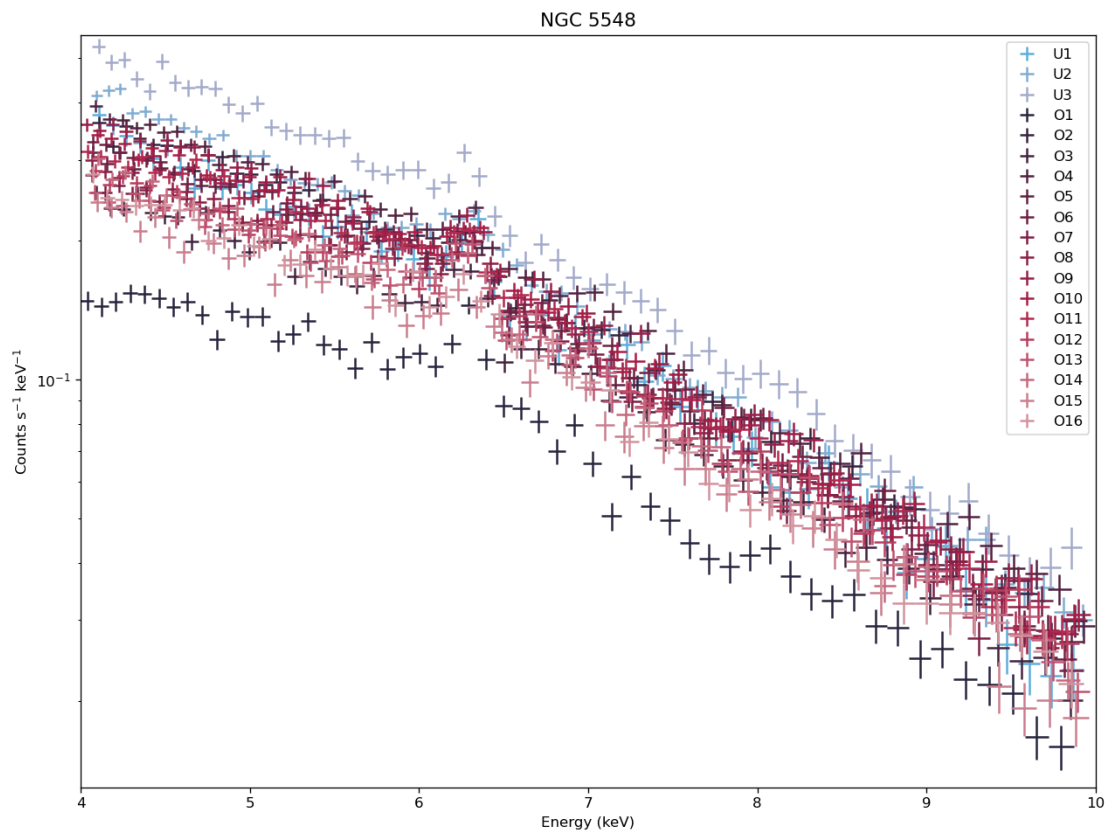


Figure 5.3: Average spectra of all the analyzed NGC 5548 observations.

5.1 Fe K α line

The baseline model used to fit all 125 spectra of NGC 5548 is the same as described in Sect. 3.1, i.e., a partially covering neutral absorber, a power law and a narrow (10 eV) Gaussian line to represent the Fe K α . The trend of the line parameters in time are presented in Fig. 5.4, Fig. 5.5, and Fig. 5.6. In Fig. 5.4 we show the rest-frame energy of the Fe K α , reported with 1σ errors. While the average value remains consistent with the ~ 6.4 keV expected for a line produced by neutral matter across all of the observations (over a time span of almost 16 years), we detect some isolated variations over times as short as our time bins, 7 ks.

The same happens with the line normalization, as displayed in Fig. 5.5: the average values span from $\sim 4 \times 10^{-5}$ to $\sim 6 \times 10^{-5}$ and are overall consistent in time considering we register 1σ errors up to the order of $\sim 20\%$; however, some episodes of variations seem to be present. Considering the energy of this feature, we see that, on average, the line is always consistent at 90% with the average value (see Fig. 5.4). Nonetheless, in O6 and O9 the energy centroid changes with time/spectral slice in an ordered way. The line energy best fit value monotonically moves from 6.48 keV toward the lower value of 6.35 keV and then it increases back to 6.4 keV. Interestingly, the light curve shows a specular behaviour with an almost monotonic increase during the same period in which the line energy displays hints of shifts towards lower energies and a decrease when the line is moving back toward higher energies. During O9, the best fit of the centroid of the line shows a pattern very similar to what observed in O6, but in this observation the source flux has the same behaviour of the line energy. We measured the Spearman coefficient ρ_s for the energy of the lines in these two observations, to assess if the trends we see has some statistical value. We find that, considering all the data-points, the coefficient is $\rho_s = -0.74$, with a significance of $\sim 96\%$ for O6, and $\rho_s = -0.21$, with a significance of $\sim 35\%$ for O9. If in both observations we exclude the last value (i.e, that from the plot appearing to be significantly higher), we find evidence for a significant correlation in both cases: for O6, $\rho_s = -0.96$, with a $\sim 4\sigma$ significance, and similarly for O9, $\rho_s = -0.94$ at $\sim 3\sigma$.

During the other observations we may observe sometimes hints of what is observed in O6 and O9. In O3 and O15 there are hints of variability in the line EW (not observed in O6 and O9) that is following the source flux but, on average, nothing that has the systematic pattern seen in O6 and O9.

5.2 Blind search and simulations

After finding the best fit model for each of the 125 spectra, we run the blind search following the same procedure described in Sect. 3.2. The energy distributions of

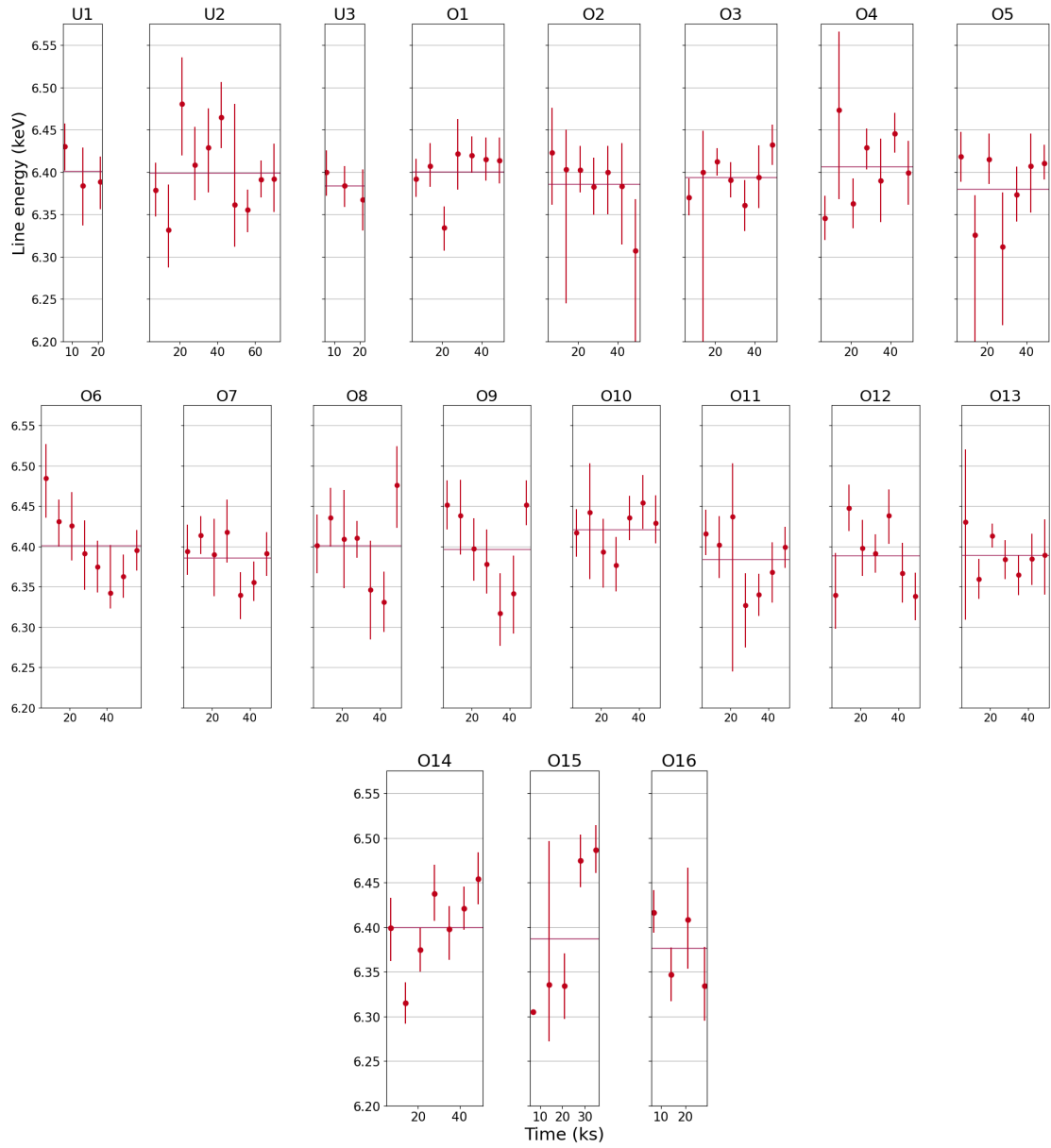


Figure 5.4: Rest-frame energy of the narrow Fe $K\alpha$ emission line.

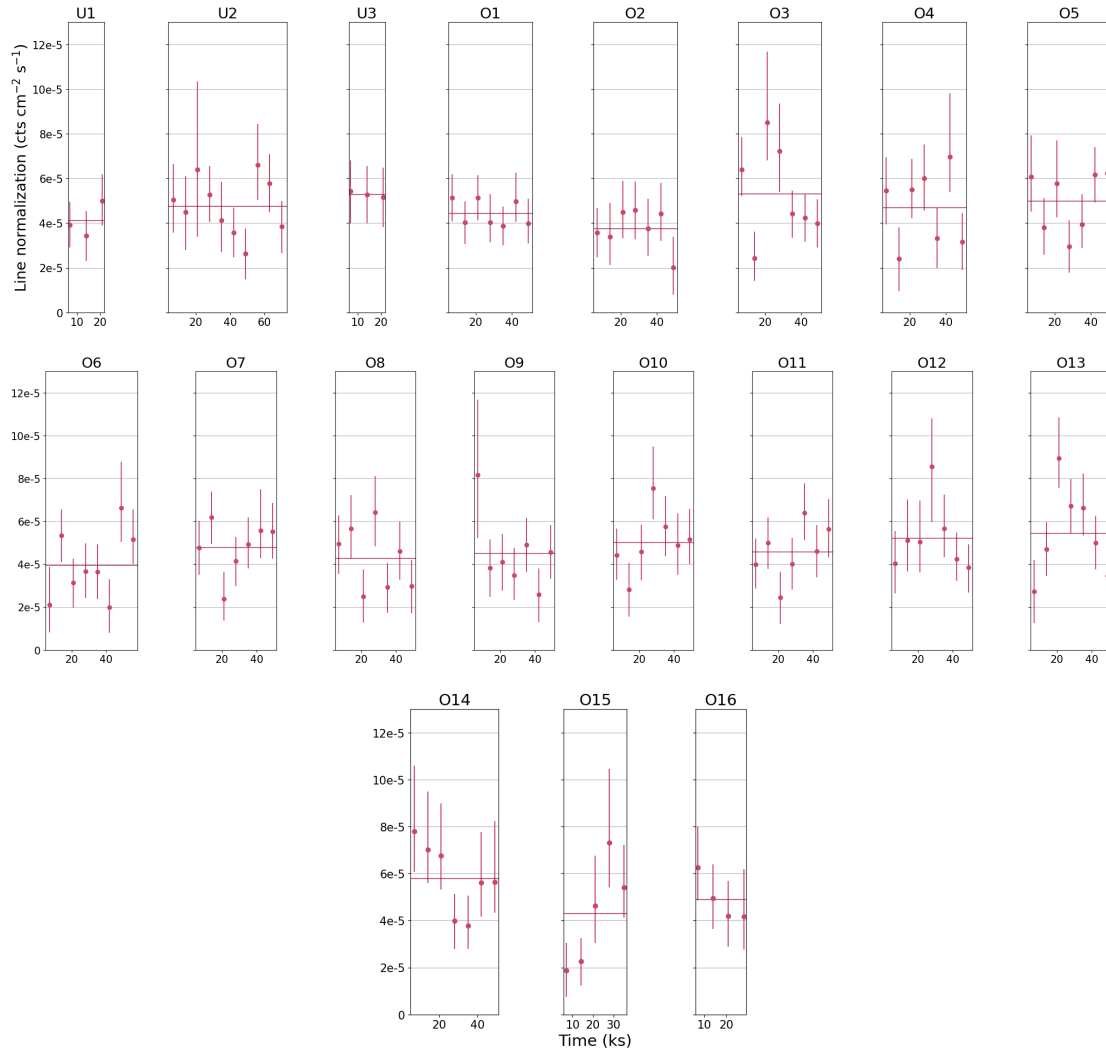


Figure 5.5: Normalization of the narrow Fe $K\alpha$ line.

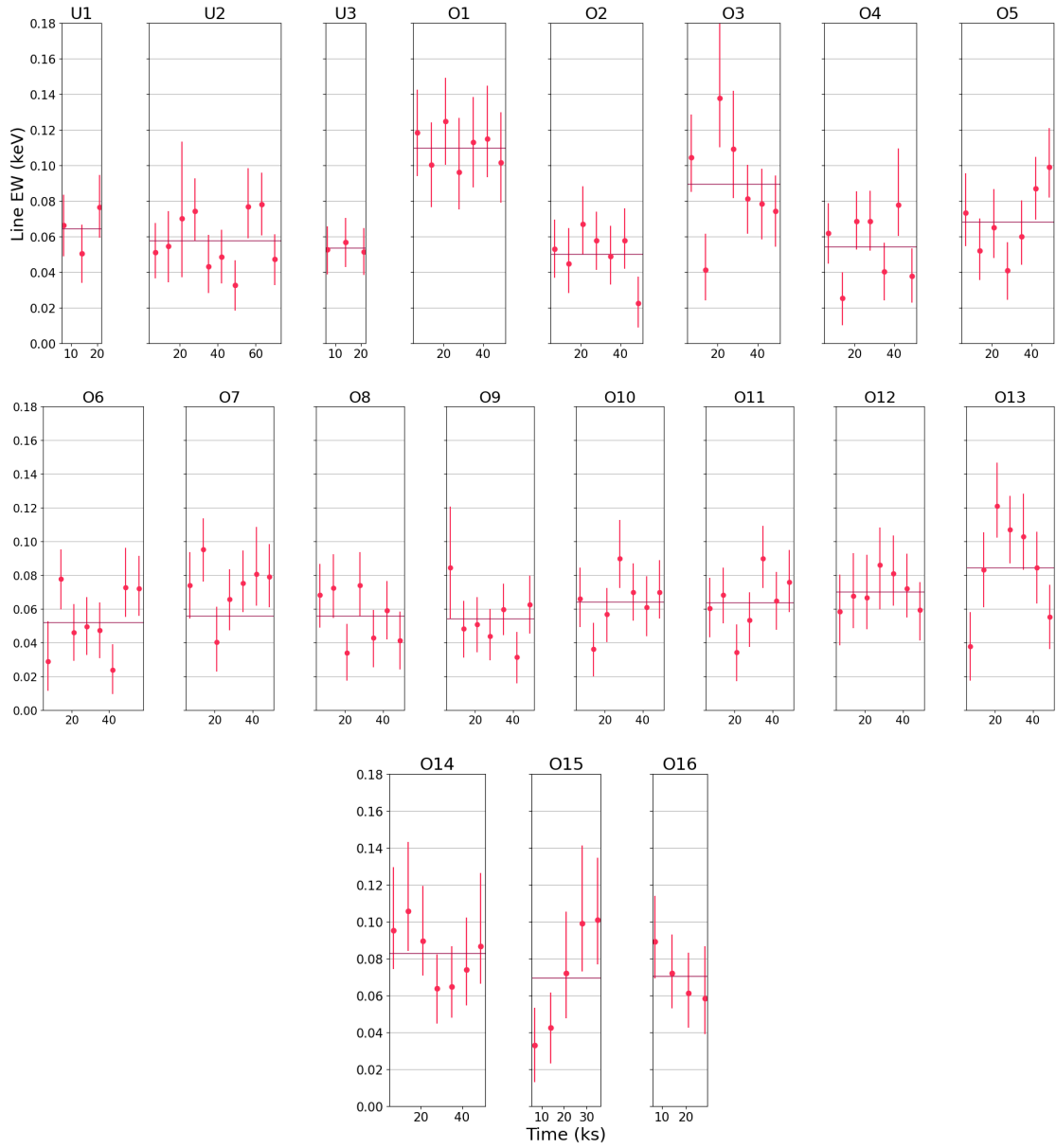


Figure 5.6: Equivalent width of the narrow Fe $K\alpha$ line.

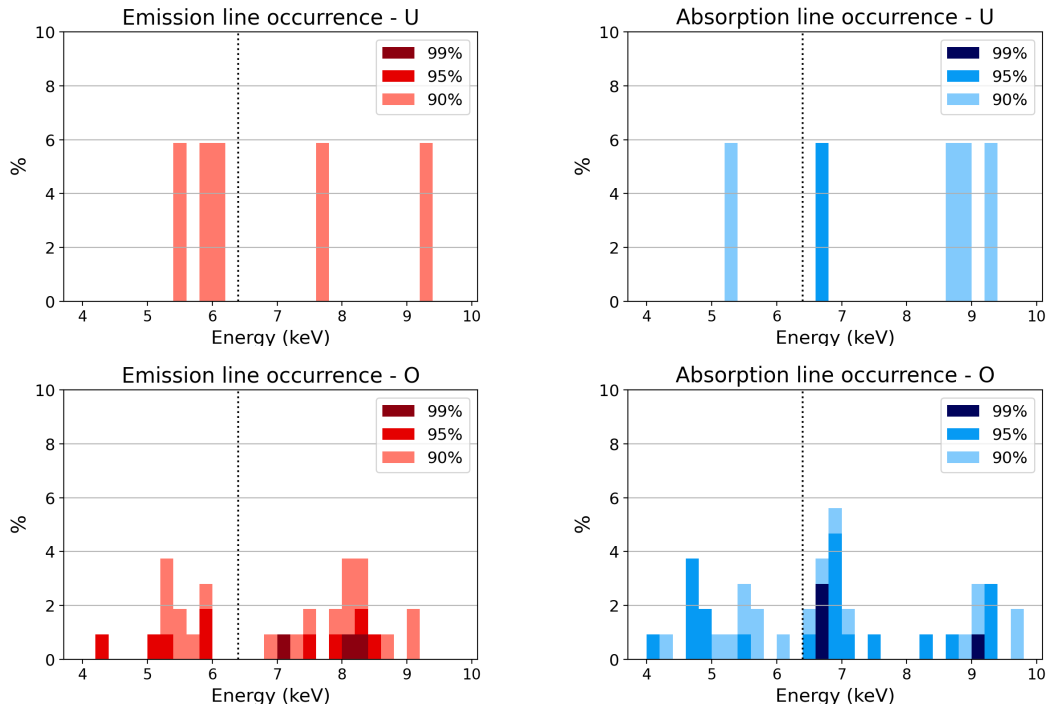


Figure 5.7: Energy distributions of the features detected via the blind search. The size of the energy bins is 0.2 keV and the height of the histograms bars are normalized by the total number of spectra in the two distinct states of the source, 17 for the unobscured (top panels) and 198 for the obscured (bottom panels).

all the detected features are reported in Fig. 5.7, the bin size is 0.2 keV and the height of the bars are normalized by the number of spectra taken into account. Once again we considered separately the unobscured and obscured state, in order to find out whether the presence of the obscurer is linked to the appearance (or disappearance) of discrete features. For this source a comparison is not immediate, as the numbers of spectra in the two phases are significantly different (17 vs 108): the frequency of the detections is always quite low, reaching a maximum of 6% in both cases, and for the unobscured one, in particular, we are dealing with single detections.

To assess the significance of the detections, we used MonteCarlo simulations. For both states, we simulated spectra in three different flux regimes (low, medium, and high) found dividing the flux range during the observations in three equal bands. The band limits for the unobscured observations are 3.5 – 4.1, 4.1 – 4.7, 4.7 – 5.3 $\times 10^{-11}$ erg s $^{-1}$ cm $^{-2}$, and for the obscured ones are 1.9 – 2.7, 2.7 – 3.6, 3.6 – 4.4 $\times 10^{-11}$ erg s $^{-1}$ cm $^{-2}$. For each of these bands, we calculated the average best-fit model, simulated it 1000 times and then counted in how many cases

Energy keV	Low	Mid	High
	%	%	%
Unobscured			
Emission			
4-6	77	88	59
6-8	89	64	64
8-10	86	68	63
Absorption			
4-6	80	85	80
6-8	82	71	64
8-10	84	84	60
Obscured			
Emission			
4-6	85	90	90
6-8	91	93	87
8-10	90	88	89
Absorption			
4-6	89	87	86
6-8	83	86	94
8-10	91	86	88

Table 5.2: Result of the MC simulations on the significance of the detected features. In none of the case the threshold of 90% is reached.

a feature with a $\Delta C > 6.25$ is detected for each energy band. We remind that $\Delta C > 6.25$ is the value set to find the 90% significance contours used in the blind search, considering 3 free parameters (energy, width and normalization of the Gaussian line). The results of the simulations are reported in Table 5.2. In almost all cases, the significance is $\leq 90\%$, and in some is largely reduced, assessing the significance of the detections at a value smaller than 1σ for all emission lines and the absorption lines at energies >6 keV in the unobscured state. The significance of the features never reached the 90% threshold in any of the studied cases.

5.3 Residual maps

The residual maps of all the observations of NGC 5548 analyzed in this work are displayed in Fig. 5.8. They were produced following the procedure described in Sect. 3.4.1. As expected from the the blind search, we do not recognize any specific “cluster” of features: positive and negative residuals appear to be quite evenly distributed and do not reach high values of $|\Delta\chi|$, except for two peaks in the Fe K α in O3 and O13 that are also present in Fig. 5.5. We are not able to recognize any interesting pattern in these maps or any correlation or anti-correlation.

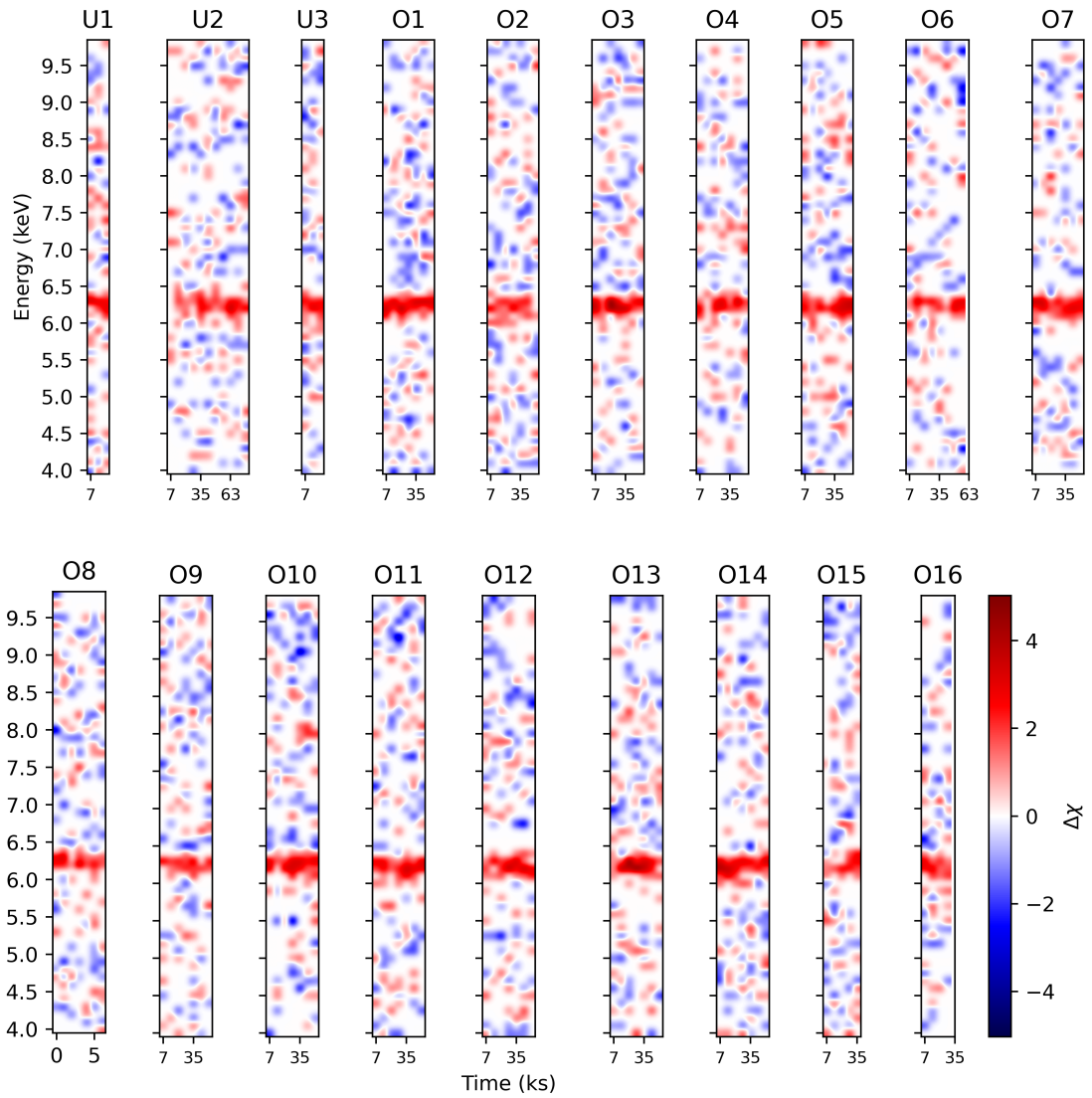


Figure 5.8: Residual maps of NGC 5548. Time bins are 7 ks.

Chapter 6

NGC 985

NGC 985, also known as Mrk 1048, is a Seyfert 1 galaxy at redshift $z=0.0427$ (Fisher et al., 1995). The galaxy presents a ring-like structure, suggesting that is going through a merger (de Vaucouleurs and de Vaucouleurs, 1975). Observations with *ROSAT* suggested the presence of a warm absorber in the X-rays (Brandt et al., 1994), later confirmed by *ASCA* (Nicastrò et al., 1999), and then observed with grating spectra by *Chandra* (Krongold et al., 2005) and *XMM-Newton* (Krongold et al., 2009). In 2013, a *Swift* monitoring caught the source in a low-flux state, which triggered two *XMM-Newton* observations: the drop in flux was ascribed by Parker et al. (2014) to a partially covering cold obscurer, identified as cloud in the BLR at a radius of a few 10^{18} cm. In 2015, the source was observed again by *XMM-Newton*: this time, it appeared to be coming out of the eclipsing event, with the column density of the obscurer diminished by about one order of magnitude, from $\sim 10^{22}$ to $\sim 10^{21}$ cm^{-2} (Ebrero et al., 2016).

Among the observations available in the *XMM-Newton* archive, we excluded two: OBS ID 743830601, because of how badly it is affected by flares, and OBS ID 0690870101, because of its short exposure (21 ks). Among the observations we analyzed, one shows the source in an obscured state (and is therefore indicated as O) and two in an unobscured one (U1, U2). Their light curves are shown in Fig. 6.1 and the spectra in Fig. 6.2. The minimum count rate in the 4.5–12 keV band reported in the 4XMM-DR11 catalogue is 0.373 ± 0.003 ct s^{-1} , thus, to ensure the minimum number of counts of 5000 per spectrum, we set the time resolution as 13.5 ks. The mass of the SMBH of this source is $2 \times 10^8 M_{\odot}$ (Vasudevan et al., 2009); this allows us to get really close to the center of the system with the time-scale we have chosen. Not only we oversample by a factor 100 the orbital period at $10R_g$ (~ 196 ks), but we can get as close as the ISCO even in the case of a maximally rotating BH ($t_{\text{ISCO}} \sim 15$ ks).

Obs ID	Start date	Label
0690870501	2013-08-10 21:00:25	O
0743830501	2015-01-13 09:35:34	U1
0743830601	2015-01-25 08:30:56	U2

Table 6.1: OBS ID of the observations of NGC 985 analyzed in this work and relative denominations used.

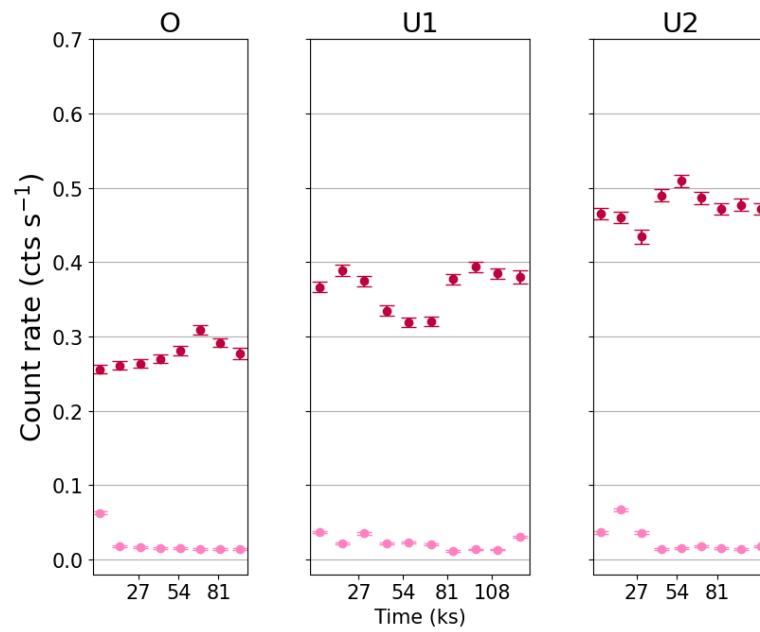


Figure 6.1: Light curves of the analyzed NGC 985 observations. Time bins are 13.5 ks.

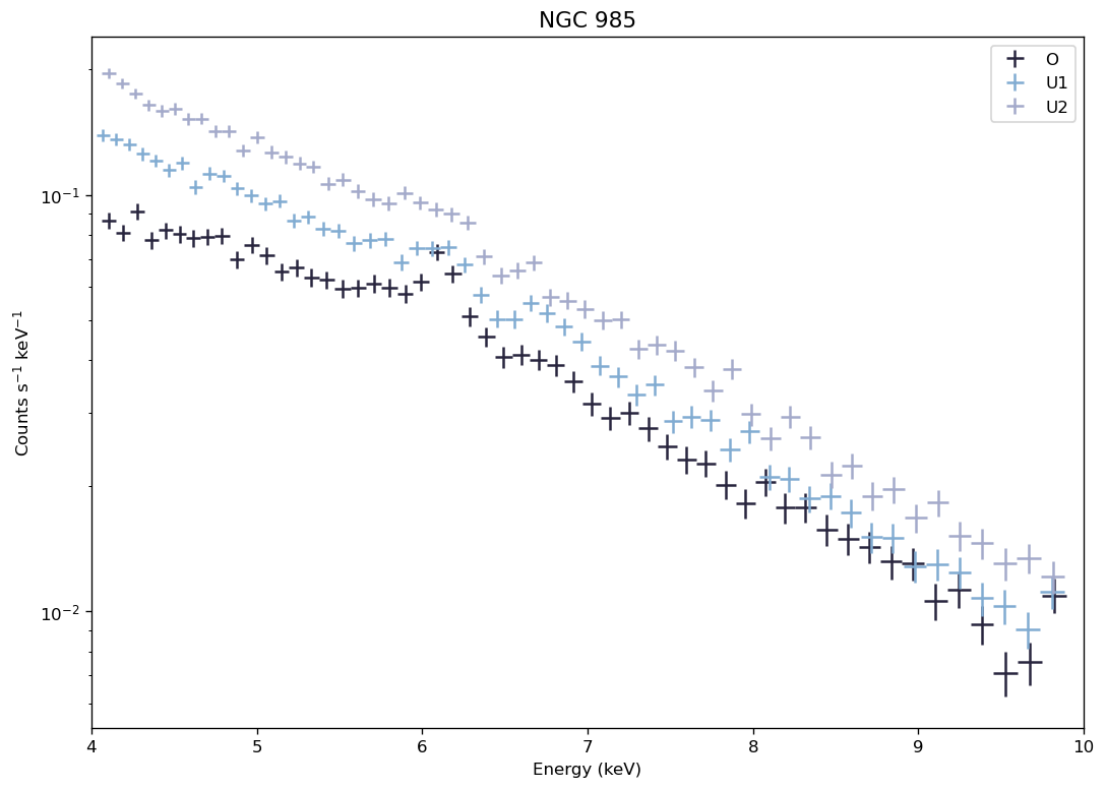


Figure 6.2: Average spectra of the analyzed observations of NGC 985.

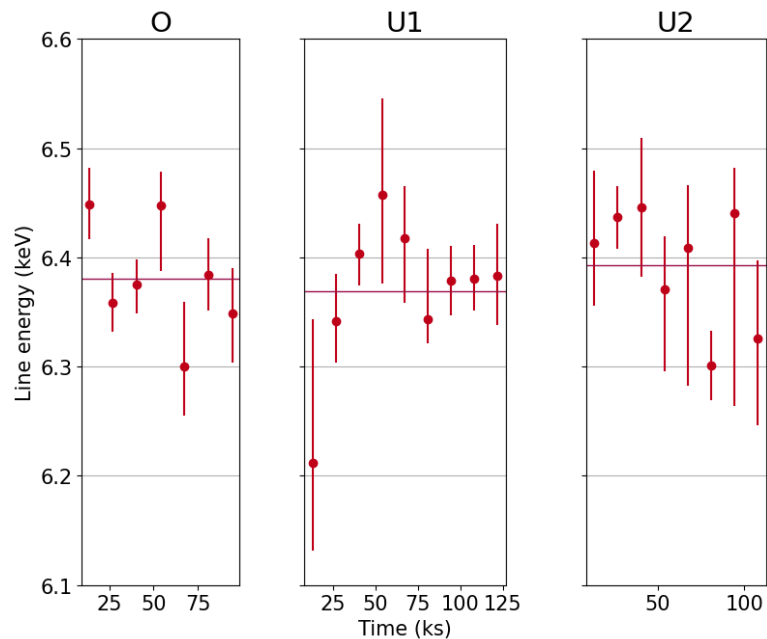


Figure 6.3: Rest-frame energy of the Fe K α line.

6.1 Fe K α line

To model the 24 spectra extracted from the three observations, we use the model described in Sect. 3.1, consisting in a power law, a narrow Gaussian emission line to account for the Fe K α and a partially covering cold absorber. Observing the energy of the line in Fig. 6.3, we detect some minor variations on short time scales, with the rest-frame value spanning from ~ 6.2 keV to ~ 6.45 keV within the same observations. The average value remains consistent. As for the normalization, shown in Fig. 6.4, we see a slight decrease in the average value among O and U1-U2, but the values remain consistent considering the uncertainties. The EW, displayed in Fig. 6.5, follows the same trends of the normalization on short time scales. A variation from ~ 100 eV to ~ 50 eV is observed between the obscured and unobscured state, consistent with the rising of the flux. This places the origin of the line far from the primary X-ray source.

6.2 Blind search and simulations

We ran a blind search on the 24 spectra of NGC 985, once again using the procedure detailed in Sect. 3.2, i.e., adding a Gauss component with all the parameters free to vary and selecting the combinations of normalization and energy that im-

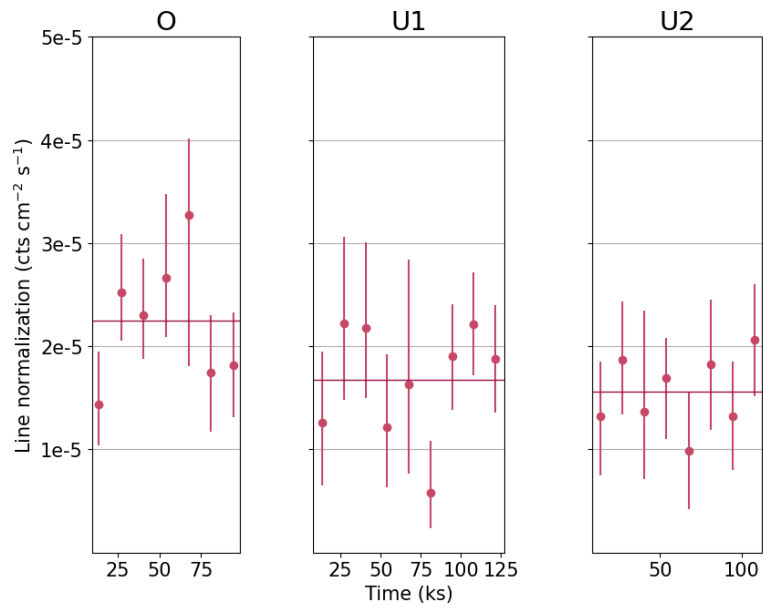


Figure 6.4: Normalization of the Fe K α line.

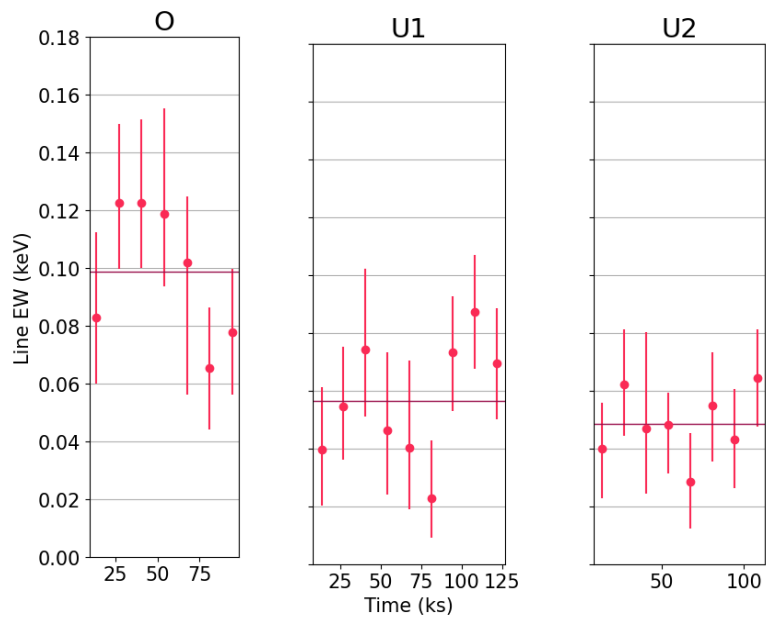


Figure 6.5: EW of the Fe K α line. Errors are at 1σ .

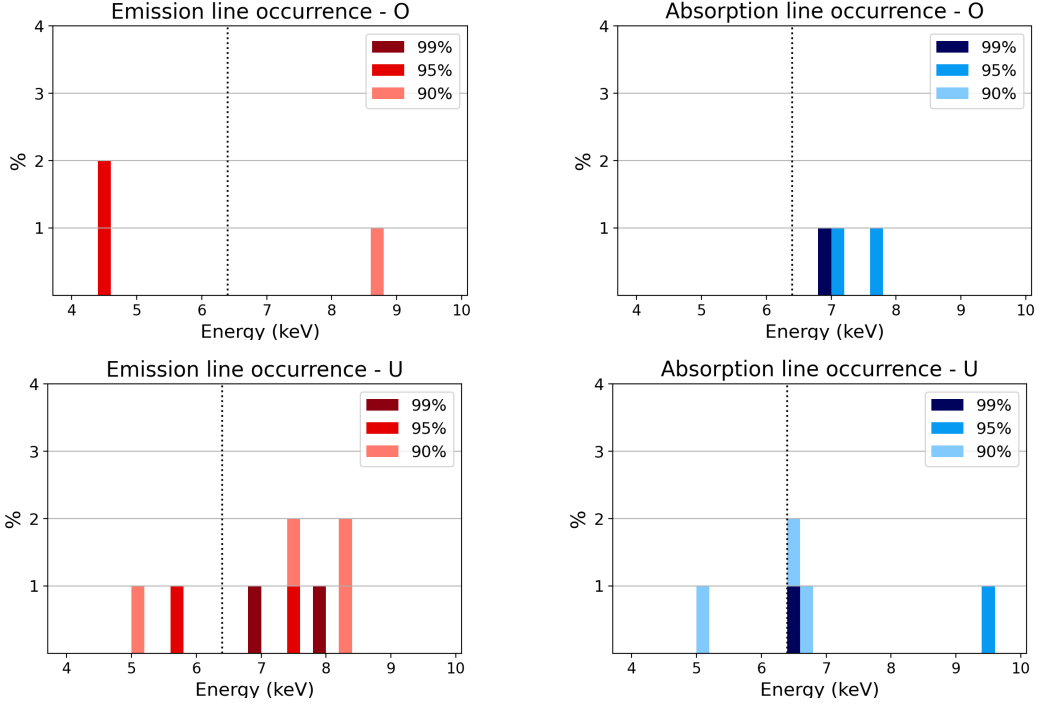


Figure 6.6: Energy distribution of the detections in the obscured and unobscured phases of NGC 985. Energy bins are 0.2 keV.

prove the fit by 90%, 95% and 99%. The results of this procedure are shown in the histograms in Fig. 6.6, where we plot the distribution in energy of the detected features. To assess the significance of the detections, we use MonteCarlo simulations. For the unobscured state we consider three different regimes for the flux, $1.08 - 1.30$, $1.30 - 1.51$, $1.51 - 1.73 \times 10^{-11} \text{ erg cm}^{-2} \text{ s}^{-1}$; for each regime, we calculate the average model and simulate it 1000 times. Conversely, for the obscured state, since it consists of a singular observation with flux variations $< 10\%$, we did not make such distinction and simulated the average of all best-fit models of the 7 extracted spectra. The results of the simulations are reported in Table 6.2: the only case where we reach a 90% significance is for the emission line detected at 8.8 keV in the obscured state. The presence of such features have already been observed and attributed to a Cu instrumental feature (Parker et al., 2014; Ebrero et al., 2016). It is interesting to see that, while they are found to be not statistically significant from the results of the MC simulations, the hints of absorption lines detected in both states of the source between 6.7 and 6.9 keV would be consistent with being produced by the high ionization ($\log \xi \sim 2.8$) component described by Ebrero et al. (2016).

Unobscured			
Energy keV	MC σ_{single}		
	Low %	Mid %	High %
Emission			
4-6	86	84	88
6-8	92	90	87
8-10	88	90	90
Absorption			
4-6	87	88	88
6-8	85	89	87
8-10	89	88	82
Obscured			
Energy keV	MC σ_{single}		
	%		
Emission			
4-6	85		
8-10	90		
Absorption			
6-8	84		

Table 6.2: Results of the MC simulations on the significance of the detection. The only case where the significance reaches the threshold of 90% is for emission lines at $E > 8$ keV in the obscured state of the source, with a single detection. The origin of this feature is most likely instrumental (Parker et al., 2014).

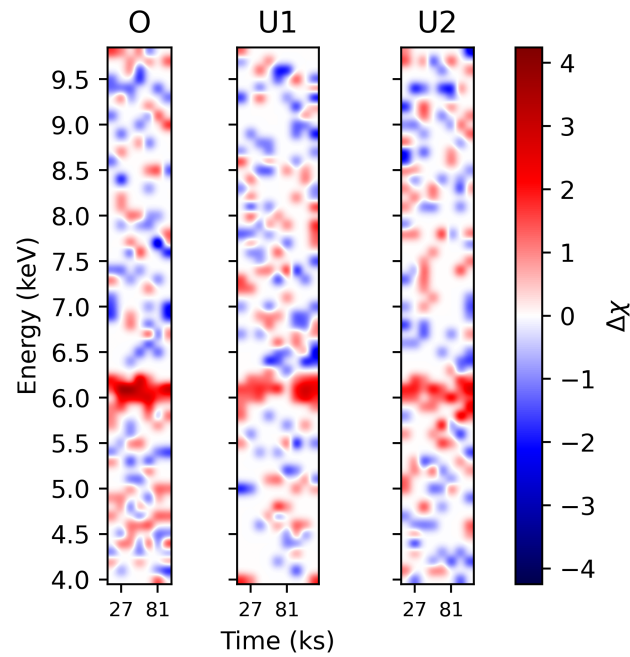


Figure 6.7: Residual maps of NGC 985.

6.3 Residual maps

We produced the residual maps of the three analyzed observations of NGC 985 following the steps detailed in Sect. 3.4.1. They are displayed in Fig. 6.7. As expected from the results of the blind search, we do not find any significant feature and/or pattern. Observing the red part of the Fe $K\alpha$ line residuals, we observe the same trends seen in Fig. 6.4: the peak in O and the dip in the middle of U1 here appear particularly evident.

Chapter 7

Conclusions

In this work, we have analyzed via time-resolved spectral analysis four bright Seyfert galaxies that underwent obscuration events observed by *XMM-Newton*: NGC 3783, NGC 3227, NGC 5548 and NGC 985.

The aim of our analysis consists in searching for possible emission and/or absorption lines in short-duration spectra extracted from the entire observations, in order to explore regions as close as the SMBH as the statistics allow for, and possibly catch transient phenomena occurring in the innermost regions (a few R_g) around the black hole, that could be evened out in averaged spectra.

We started our analysis from NGC 3783 and used it as a test-case, as in the past it had been already studied with an approach similar to ours; we used this source to have a direct comparison with literature and test our methodology. On this source we tested a baseline model and verified that, for the scope of our analysis, the best modelization consists in a power law and a narrow Gaussian emission line associated with the Fe $K\alpha$, absorbed by a partially covering neutral medium. The choice of this absorber is guided by the necessity of reproducing as much correctly as possible the curvature of the spectrum, without adding any absorption line, as it would happen if we tried to use a more "physical" ionized absorber. In fact, a "smooth" model is necessary for the subsequent step of our analysis, i.e., the blind search for features. This procedure is carried out by adding to the model a line and then finding the combinations of its parameters that significantly improve the fit by scanning the whole parameters space, for each spectrum. In this way, we detect all the lines with a minimum significance of 90%, that corresponds to $6.25 \Delta C$ (we adopted the Cash statistics) for 3 degrees of freedom of difference. After this, the significance of the detections is assessed by an extensive set of MonteCarlo simulations, that take into account the variations in flux registered among the spectra and the energy of the detected lines. A study of the energy distributions of the detections give indications about which features could possibly share a common origin; hence assuming that "clusters" of detections at certain

energy represent the re-occurrences of the same features, we measured a global significance for them by adopting the binomial distribution.

Once the significance of transient/variable features is assessed, we use the residual maps to actually trace the variations in time and energy. The residual maps are produced by taking all the residuals from the baseline model and visualizing them in the time and energy plane. They represent a renewed version of the *excess maps*, that have been extensively used in the past years to study the variations of emission lines (e.g. Iwasawa et al., 2004; De Marco et al., 2009). The major update we introduced is to display simultaneously positive and negative deviations from the model, thus allowing us to search for possible correlations in the behaviour of emission and absorption lines. In NGC 3783, the residual maps enabled us to ascribe variations in the normalization of the Fe K α to resonant absorption lines at the same energy due to clumps in the obscuring medium, whose presence is detected at $> 3\sigma$ significance according to the blind search, and to determine the dimensions of the clumps.

The same procedure – blind search on each time-resolved spectrum and production of residual maps – is applied to the other sources of the sample. In NGC 3227 we detected at the $\sim 2\sigma$ significance level an ultra-fast outflow, with velocity $\sim 0.2c$, appearing only in the first part of an observation at the end of a temporary obscuration event. This feature was not detected in the past, when only the averaged spectrum of the whole pointing was analyzed, thus possibly diluting its sign. In NGC 5548 and NGC 985 we did not detect any significant feature, either in the obscured or unobscured phases of these sources.

7.1 General properties of the sample

In the previous chapters, we have investigated the presence of discrete features in emission and/or absorption in the individual sources. A natural step forward would be to investigate whether some possible signal is present if we consider the objects altogether to be representative of a more general behaviour typical of Seyfert galaxies. As such, the study of the average results could be assumed to be representative of the class of objects.

We may think at different approaches to this kind of study. One of the most commonly used method consists the averaging of the spectra of the different sources/observations. This “stacking” technique is often used to investigate the spectral properties of faint sources in surveys. It relies on the assumption that, at the real core, every AGN, in X-rays, is well described by the same intrinsic model. The adoption of this technique in this context is hampered by the clear differences that we observe in both time-averaged and time-resolved spectra presented above. We know that this is true not only for the different sources but also for the

individual objects even within the same pointing.

Nonetheless, in order to understand whether what we observed is a general property of AGN, we can simply consider all the sliced spectra analyzed here as if all of them were obtained from a single source.

This assumption is somehow corroborated by the results that we obtain by averaging the obtained values of the continuum. Table 7.1 reports the average values for the spectral photon index and Fe $K\alpha$ emission line. The average value of the spectral photon index obtained for the 373 spectra investigated here is $\Gamma = 1.8 \pm 0.2$, perfectly in agreement with what obtained in studies of samples of AGN (e.g. Dadina, 2008). For comparison, the CAIXA sample assembled by Bianchi et al. 2009 is a set of the brightest 156 radio-quiet AGN observed by *XMM-Newton*; using a baseline model that includes only basic cold absorption, they obtained for the photon index a value of 1.73 ± 0.49 .

Considering only the flux in the 4–10 keV energy band, we do not observe a clear “softer when brighter” behaviour (as typically observed in AGN) between the measured photon index and the flux, as shown in Fig. 7.2.

We find the same accordance also on the properties of the Fe $K\alpha$ emission line, which is found to be at $E = 6.40 \pm 0.04$ keV, i.e. exactly at the expected energy for a component emitted from cold material. This strongly suggests that at least the bulk of this feature is produced from matter quite distant from the central SMBH. Further evidence for this is provided by the EW increase in states of low flux, e.g. in both the obscured observations of NGC 3783 (lower row of Fig. 3.2), in observations O1 and O3 of NGC 3227 (Fig. 4.6), and in observation O of NGC 985 (Fig. 6.5). Because of the definition of the equivalent width, its anti-correlation with the primary X-ray source flux indicates that the line itself is steady and does not respond immediately to continuum flux variations.

Obviously, the same kind of test does not hold for the absorbing column density: in fact, the sources were selected because they are known to show occultation events, so we expect a somewhat erratic value for the N_H value and for the covering fraction. Moreover, the limited band adopted to perform the analysis is hampering a robust measurement of this parameter. The average value obtained, $N_H \sim 24 \times 10^{22} \text{ cm}^{-2}$, is somehow in between what measured as average values for type I and type II objects, but the uncertainties are large (Table 7.1).

All these findings somehow support the idea that the AGN studied here are intrinsically powered by the same mechanisms and, thus, that we may use the entire sample of 373 spectra extracted for the four sources analyzed here to possibly obtain more general results, also on the occurrence of transient absorption/emission features. The basic idea is that the simple counting of the detections among all the slices could give us some insights on the real significance of the recorded transient features. In doing so, we must be aware that we may be introducing a series of

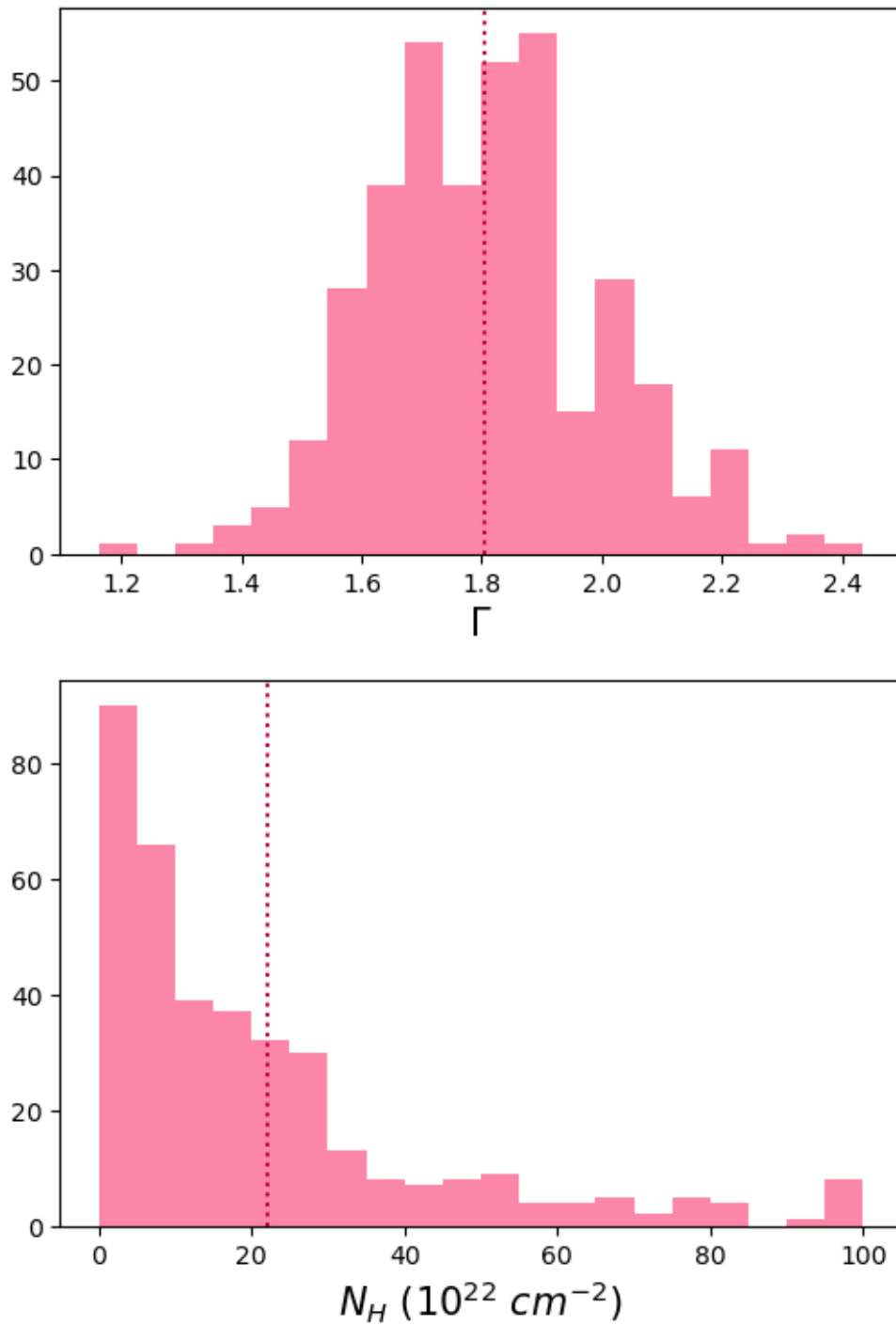


Figure 7.1: Distributions of the photon index Γ (upper panel) and column density of the absorber N_H (lower panel) from the best-fit models of the 373 spectrum analyzed in total. The dotted vertical lines represent the average values.

Γ	1.8 ± 0.2
N_{H}	$24 \pm 22 \text{ } 10^{22} \text{ cm}^{-2}$
Covering Fraction	0.7 ± 0.3
Fe $K\alpha$ energy	$6.40 \pm 0.04 \text{ keV}$

Table 7.1: Average values of the baseline model parameters considering the best fit of all 373 sliced spectra analyzed in this work.

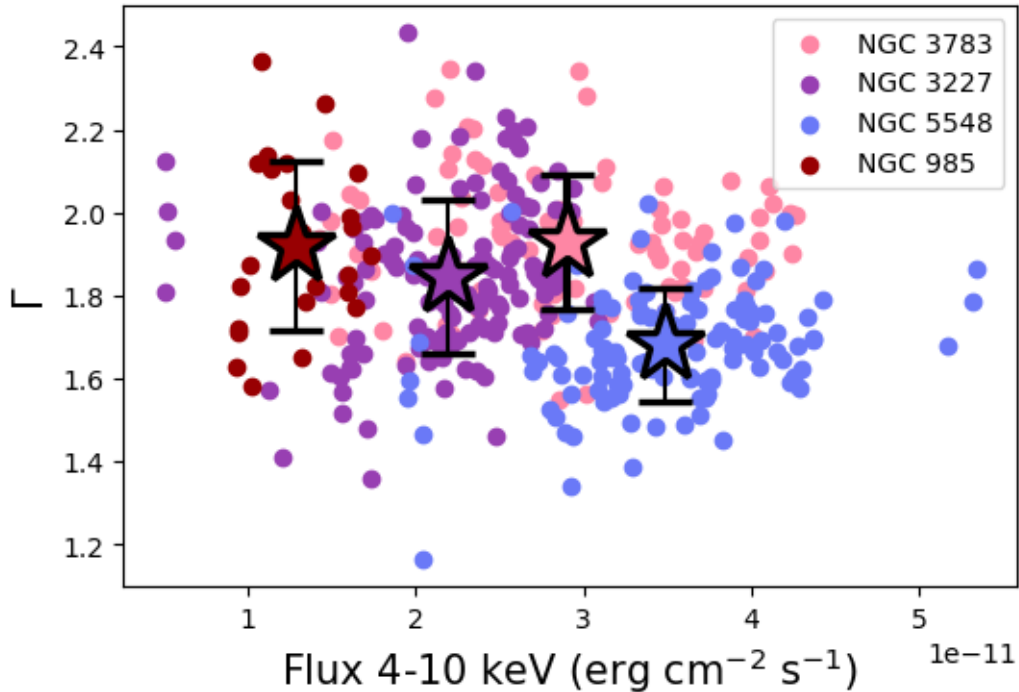


Figure 7.2: Photon index Γ vs 4–10 keV flux for the 373 spectra of the four Seyfert galaxies analyzed in this work. The stars represent the mean value of Γ and flux for each source, with the standard deviation of the measured Γ as error.

	Obscured	Unobscured
Spectra	193	180
Energy band keV	Occurrences	
	Emission	
4-6	7	11
6-8	13	13
8-10	2	-
	Absorption	
4-6	3	-
6-8	12	-
8-10	9	-

Table 7.2: Occurrences of the detections of features with a significance $\geq 90\%$ among all objects.

issues, as described below. As discussed for the individual sources, the duration of the time slices had to be tailored on both the available statistics and the sizes of the regions around SMBH to be tested. This problem was faced, for example, in NGC 3227, where we needed to change the time resolution among observations to collect enough photons for a meaningful analysis at the cost of probing regions further from the SMBH. Here, the same issues is also present, coupled with the fact that the sources have different SMBH masses and thus we are testing different regions (see Table 2.2 in Chapter 2.2).

Most importantly, however, we observe that transient features are observed only in two objects if we apply a filter on their statistical significance, i.e., if we only take into account the detections at $\geq 90\%$. Table 7.2 reports the total number of detections obtained for our small sample of objects.

The emission and absorption lines presented here are related only to two sources, NGC 3783 and NGC 3227, as NGC 985 and NGC 5548 turned out to not have any significant detections. This leads to a global decrease of the detection significance, when all the sliced spectra are considered together. In this case, in fact, we obtain that the number of detections is always below the 10% of the number of spectra considered in this analysis.

It is clear from the numbers presented here that the sum of the results obtained from the individual sources indicate that the detection of UFOs may not be considered as a “general” feature, i.e., UFOs are not always present in X-ray spectra of Seyfert galaxies. The only possible UFO, according to our results, has been marginally ($\sim 2\sigma$) detected in NGC 3227. We would like to point out that

Source	$L_{2-10\text{keV}}$ erg s ⁻¹	L_{bol} erg s ⁻¹	λ_{Edd}
NGC 3783	10 ⁴³	1.6-2.5 10 ⁴⁴	0.037-0.059
NGC 3227	1.6 10 ⁴²	1.6-3.2 10 ⁴³	0.020-0.039
NGC 5548	2 10 ⁴³	2.5-3.2 10 ⁴⁴	0.021-0.027
NGC 985	5 10 ⁴³	1.6 10 ⁴⁵	0.058/0.051

Table 7.3: Values from Vasudevan et al. 2010.

the four sources in our small sample are characterized by low Eddington ratio (a few per cent), and NGC 3227 is, along with NGC 5548, the source with the lowest value of $\lambda_{Edd} \sim 0.02 - 0.04$, as shown in Table 7.3 (Vasudevan et al., 2010).

Besides, NGC 3783 is the only source that shows a clear component in outflow from dense, ionized material; in this work we have confirmed the result found from the analysis of the time-averaged spectra by Reeves et al. (2004). This source is characterized by a λ_{Edd} comparable with that of NGC 985, that shows no hints of powerful outflows in the energy bands analyzed here.

These two results suggest that the Eddington ratio is probably not a discriminant factor for the characteristics of the outflows in the four objects. Something else, likely geometrical and/or AGN duty cycle effects, may be determining what we are observing.

The selection of the four sources in this sample were based primarily on the detection of occultation events. These has been found to be strongly related with the detection of outflows in optical/UV (e.g. Kaastra et al., 2014), with velocities of the order of a few 10³ km s⁻¹. In X-rays, the occultation is clearly imprinting the low-energy cut-off due to absorption, as evident from the spectra shown in Fig. 4.3, 5.3 and 6.2. Yet the detection of discrete outflowing components is not straightforwardly following it and/or does not appear to be a “general” property. On the one hand, we find that all the absorption lines detected at more than 90% confidence level occur during the obscured phases (Table 7.2); on the other hand, we have only one – statistically speaking – strong feature, i.e. the one detected in NGC 3783.

7.2 Comparison among the individual sources

The fact that we are finding significant detections of features only in one of the four sources analyzed is most probably only marginally influenced by the difference in statistics among the different sources, since we are dealing with datasets that are essentially comparable from this point of view. The analyzed datasets, in fact, have

been sliced so as to have approximately the same minimum number of counts. Our time-resolved analysis has been able to strongly confirm the outflow found in the time-averaged spectra of NGC 3783 but has been unable to find clear evidences for winds in the other sources, except for – as previously reported – a $\sim 2\sigma$ indication of outflow in NGC 3227. The uniformity in terms of counts per spectra of our sample suggests that our non-detections are not only possibly ascribed (at least in part) to a scarcity of photons, but to an intrinsic lack of strong features.

We are left to assume that what we observed must be due to one or a combination of the following effects.

- These occultation events could produce transient and weak discrete features in the X-ray spectra of Seyfert galaxies, but they are below the detection threshold tested here. In this scenario, NGC 3783 is representing a particular case with lines sufficiently strong to be detected. In particular, the column density of the medium is what mainly influences the intensity of the absorption line; this could imply that in the sources where we did not detect features the eventual outflow should have a column density lower than the value of $\sim 10^{23} \text{ cm}^{-2}$ measured in NGC 3783.
- The differences observed here are due to intrinsic differences among the sources, seemingly not related to the Eddington ratio. This means that the variety of physical conditions observed in the winds, that manifest themselves through multi-component outflows, are not strictly related to the accretion rate. Therefore, these sources can have similar accretion but different ejection.
- Since the occultation clearly has the highest impact in the soft energy band, these phases are mostly characterized by cold, outflowing gas that is not expected to produce features in the 4–10 keV band, where only highly ionized matter is expected to show transitions. In this case, the presence of a more ionized component is not strictly related with the obscurer, so even if all the sources underwent a similar obscuration event, the presence of the wind producing the discrete absorption features would be unrelated to it.

The study of the average spectra of the sources in this sample contain at least part of the possible explanation. NGC 3783 exhibits the larger and most ionized absorber ($\log\xi \sim 3$, $N_{\text{H}} \sim 10^{22} \text{ cm}^{-2}$ for the unobscured state, [Reeves et al. 2004](#); $\log\xi \sim 3.7$, $N_{\text{H}} \sim 10^{23} \text{ cm}^{-2}$ for the obscured state, [Mehdipour et al. 2017](#)) a combination of characteristics that certainly facilitates the detections of the features due to the outflowing component in the 4–10 keV band considered here, as they are found to produce more intense lines. In this respect, it is interesting to notice an increase in value on both the ionization parameter and the column density

during the obscuration event: in NGC 3227, the ionized matter which is present in the unobscured epoch gets de-ionized by the shadowing effect of the obscurer (Mehdipour et al., 2021), while in NGC 3783 the opposite occurs. This could lead us to think that in NGC 3783 the most extreme component is located internally with respect to the obscurer, and that the same launching mechanism that accelerates the less ionized obscurer is responsible for the raise from the disk of an inner, hotter component that gets summed up with, or replaces, a pre-existing wind. It would be interesting to verify whether, at the end of the obscuration event that lasted few weeks, the high-ionization component of the outflow returned to its pre-obscured condition and if it is still present at all: this, in fact, would help us to differentiate somehow the origin of the outflows in this source.

In the other sources, the average properties of the absorbing material are less extreme than in NGC 3783, both in the obscured and unobscured phases. In NGC 3227, Wang et al. (2022) found 4 distinct WA components at different ionization states, $\log\xi \sim 3, 2.7, 1.8$ and -1.8 , respectively, with column densities of the order of $\sim 10^{21} \text{ cm}^{-2}$ for the unobscured and partially obscured observations. As stated above, Mehdipour et al. (2021) finds them de-ionized in the obscured state, with the new ionization parameters being $\log\xi \sim 2.4, 2.1, 1.2$ and -2.4 and, in addition, the new obscurer has a column density of the order of $\sim 10^{22} \text{ cm}^{-2}$ and $\log\xi = 1$. In NGC 5548, Cappi et al. (2016) reported two absorption components in both states. The unobscured states comprise a first component with $\log\xi \sim 1$ and $N_{\text{H}} \sim 10^{21} \text{ cm}^{-2}$ and a second component with $\log\xi \sim 2.7$ and $N_{\text{H}} \sim 10^{22} \text{ cm}^{-2}$. For the obscured state, instead, they measured $\log\xi \leq 0.7$ with $N_{\text{H}} \sim 10^{22} \text{ cm}^{-2}$, and the obscurer is in the form of a colder component with $\log\xi = -1$ and $N_{\text{H}} \sim 10^{23} \text{ cm}^{-2}$. Finally, in NGC 985 Ebrero et al. (2016) found multiple ionized components with $\log\xi$ spanning from ~ 1.8 to ~ 2.8 and N_{H} from $\sim 10^{22} \text{ cm}^{-2}$ to $\sim 10^{21} \text{ cm}^{-2}$, respectively, quite steady despite the change of column density in the obscurer between the two states. In the condition of these sources, the detection of absorption features is harder than in NGC 3783: in fact, the depth of the lines is determined in the first place by the column density of the medium and then, at the second order, by the ionization parameter, that influences mostly the energy of the feature. We could argue that, similarly to the discussion related to NGC 3783, the material observed in all the other sources could produce some absorption at energies comparable with that of the Fe $K\alpha$ considering its ionization state and that at least part of the small variations of the emission line could be the effect of a variable absorption superimposed on a steady emission line. Currently, it is not possible to disentangle these effects: in fact, the EW of the resonant absorption features would be comparable to the uncertainties that we register for the EW of the emission line. A higher column density would produce deeper lines and therefore significant detections.

7.3 Future perspectives

In the next years, we expect to face significant improvements in the energy resolution that we will be able to achieve and in the collecting area, thanks to the launch of *XRISM* (XRISM Science Team, 2020) and *ATHENA* (Nandra et al., 2013). These telescopes have been designed with the purposes to investigate the matter in extreme conditions. In particular, the science themes for which *ATHENA* was selected is the study of the "hot and energetic universe". Among the multiple topics that will be investigated, the physics of AGN-driven winds is one of the most important for both missions.

XRISM (X-Ray Imaging and Spectroscopy Mission) is expected to be launched in the Japanese fiscal year 2022. Its spectrometer, *Resolve*, will have an effective area smaller than that of the EPIC-pn, but thanks to the micro-calorimeter detector, the energy resolution will be ≤ 7 eV at 6 keV, to be compared with the ~ 100 eV of *XMM-Newton* at the same energy.

ATHENA (Advanced Telescope for High ENergy Astrophysics), set to be launched in 2034, will also have an X-ray spectrometer based on micro-calorimeters: the *X-IFU* (X-ray Integral Field Unit, Barret et al. 2018). This instrument will have an energetic resolution ≤ 3 eV at energies up to 7 keV and a highly improved effective area, $\sim 3 - 6$ times larger than *XRISM* at 7 keV and up to 45 times larger at 1 keV, and overall 6-15 times large than that of the *XMM-Newton* EPIC-pn.

It is worth considering, however, that a comparison with the EPIC-pn is only marginally correct if we want to have a first insight on the real capabilities that will be opened by the new instruments in doing time-resolved analysis as performed in this thesis work. The energy resolution of *X-IFU* and *Resolve*, in fact, are more similar to those of the grating spectrometers on board *Chandra* and *XMM-Newton*, thus a fairer comparison would be with the collecting areas of the latter instruments (HETG and RGS, respectively), as shown in Fig. 7.3.

An example of the capabilities of the X-IFU is shown in Fig. 7.4, taken from an upcoming paper by Fukumura et al. (in prep.) The upper panel shows (green color) the theoretical model of a bright AGN ($F_{2-10 \text{ keV}} = 2 \times 10^{-11} \text{ erg s}^{-1} \text{ cm}^{-2}$), with the power law absorbed by four different components, the Galactic absorption and three distinct WA and, in addition, an UFO with a velocity of 0.01 c, launched by magneto hydro-dynamics (MHD) mechanisms, whose model is convolved with those of the absorbers. In the lower panel, the black points represent the simulated X-IFU spectrum with an exposure of 10 ks. All the components of the model here are clearly resolved, whereas a spectrum extracted from an *XMM-Newton* observation would only report broad troughs.

In Fig. 7.5 (also from Fukumura et al., in prep.), we show a direct comparison of a simulated 100 ks spectra taken with *Resolve* (upper three panels) and of 10 ks taken with *X-IFU* (lower three panels), both plotted with the model described

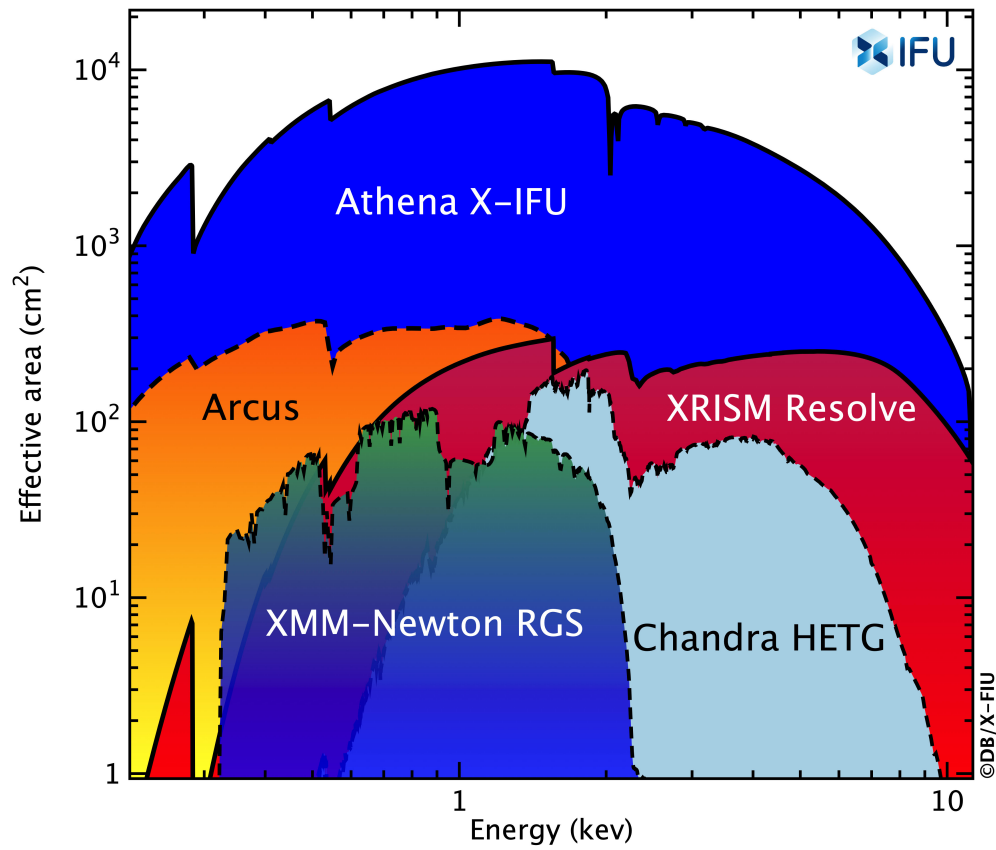


Figure 7.3: Comparison among the effective areas of present and future instruments with high energy resolution. Credit: [Smith and Arcus Collaboration 2018](#).

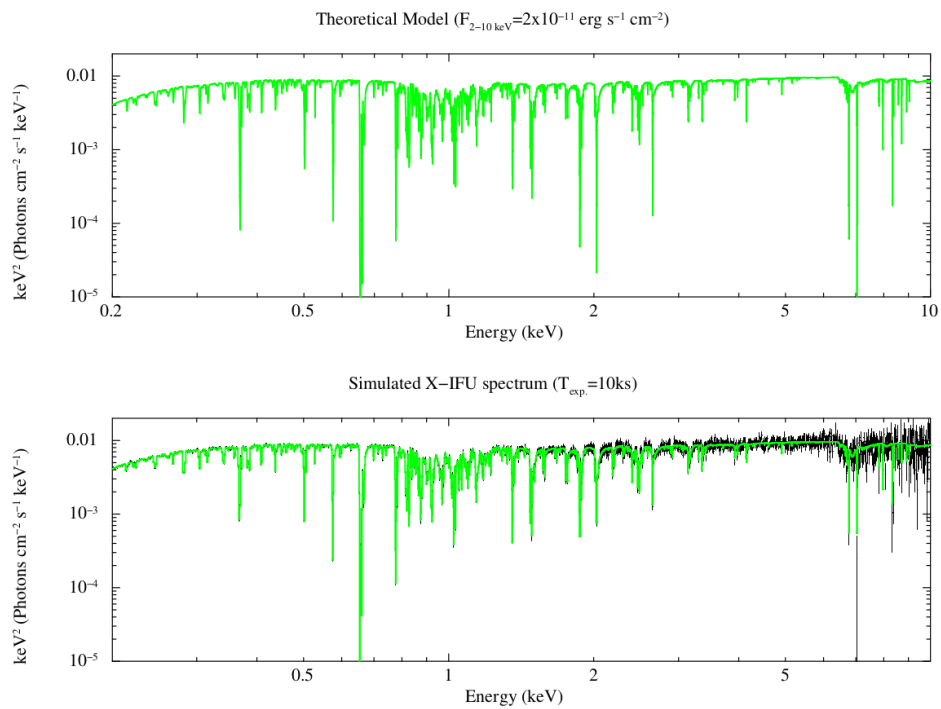


Figure 7.4: In the upper panel: theoretical model for the spectrum of an AGN with absorption features produced by three distinct WA components and an UFO, launched by magneto hydro-dynamics mechanisms. In the lower panel, the same model and the simulated spectra from a 10 ks exposure taken with the *X-IFU* are shown. Credit: Fukumura et al., in prep.

CHAPTER 7. CONCLUSIONS

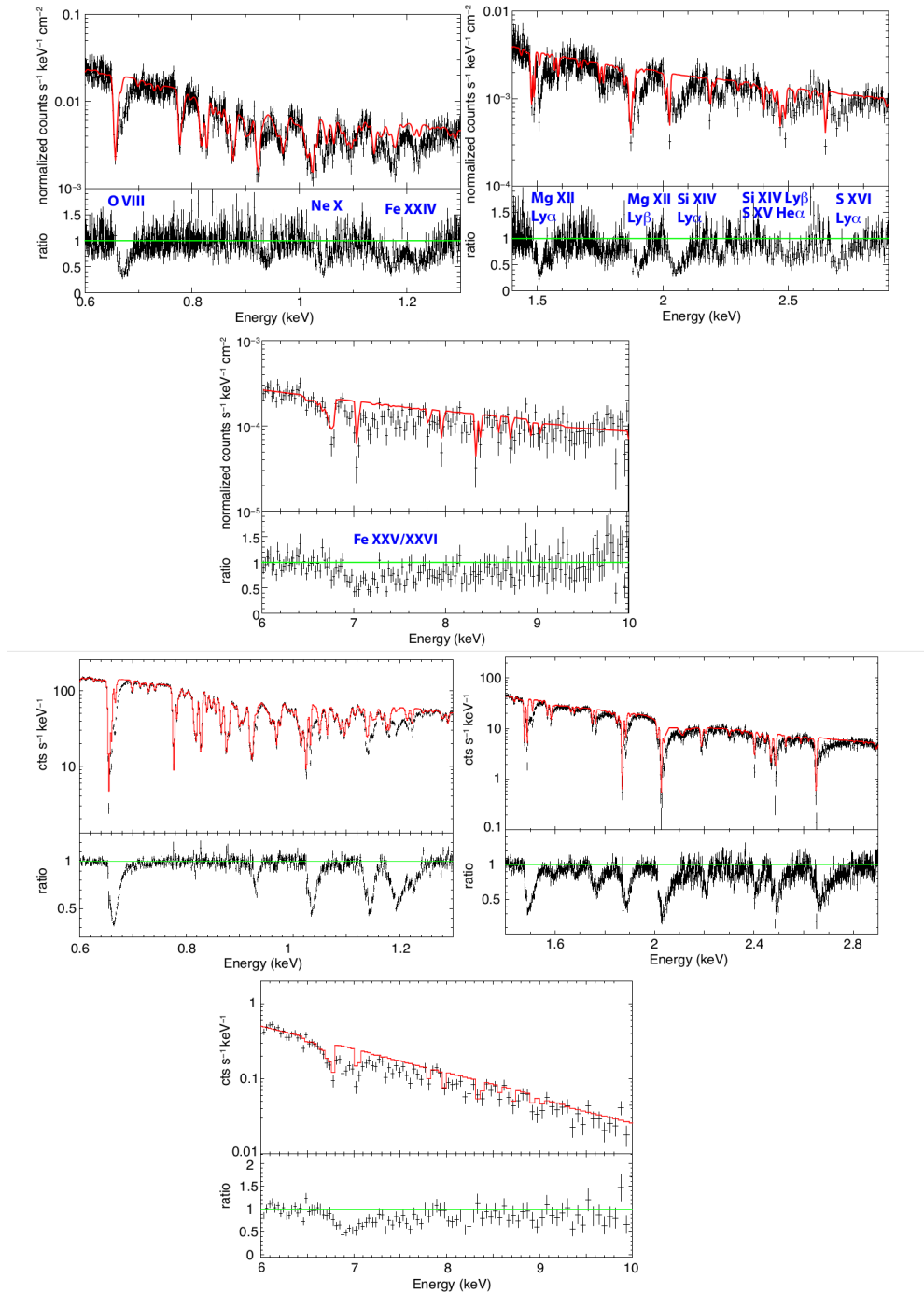


Figure 7.5: Zoom on three energy ranges of the model of the spectrum of an AGN with absorption features produced by three distinct WA components and an UFO, launched by magneto hydro-dynamics mechanisms, represented with a 100 ks simulated spectrum of *XRISM/Resolve* in the upper three panels, and with a 10 ks simulated spectrum of *Athena/X-IFU* in the lower three panels. Credit: Fukumura et al., in prep.

above, but this time with the MHD component being removed (in red). From the observation of the spectra and the residuals, it is clear that, despite the 10 times shorter exposure, the *X-IFU* is less noisy and allows for more significant detection of the features, as the absorption lines are extremely clear in all the energy bands shown in Fig. 7.5. Moreover, the *X-IFU* will allow us to resolve in more detail the shape of the lines and, therefore, distinguish the physical process that produced them. The simulation used here represents an AGN with a flux of the same order of the source analyzed in this thesis work, and its duration is comparable with the time resolution we used for the time-resolved spectral analysis. Having all these conditions in mind, we think that the *X-IFU* should be considered the real instrument of the future for time-resolved deep spectral investigation of AGN, since it will allow us to collect enough photons on short time scales to produce good-quality spectra. By this instrument, it will be possible to achieve more statistically sound results on objects as bright as those analyzed in this work, but also to perform time-resolved analysis on weaker objects, in order to derive more general properties of AGN.

Bibliography

- Bardeen, J. M., Press, W. H. and Teukolsky, S. A. (1972), ‘Rotating Black Holes: Locally Nonrotating Frames, Energy Extraction, and Scalar Synchrotron Radiation’, *ApJ* **178**, 347–370.
- Barret, D., Lam Trong, T., den Herder, J.-W., Piro, L., Cappi, M., Houvelin, J., Kelley, R., Mas-Hesse, J. M., Mitsuda, K., Paltani, S., Rauw, G., Rozanska, A., Wilms, J., Bandler, S., Barbera, M., Barcons, X., Bozzo, E., Ceballos, M. T., Charles, I., Costantini, E., Decourchelle, A., den Hartog, R., Duband, L., Duval, J.-M., Fiore, F., Gatti, F., Goldwurm, A., Jackson, B., Jonker, P., Kilbourne, C., Macculi, C., Mendez, M., Molendi, S., Orleanski, P., Pajot, F., Pointecouteau, E., Porter, F., Pratt, G. W., Prêle, D., Ravera, L., Sato, K., Schaye, J., Shinozaki, K., Thibert, T., Valenziano, L., Valette, V., Vink, J., Webb, N., Wise, M., Yamasaki, N., Douchin, F., Mesnager, J.-M., Pontet, B., Pradines, A., Branduardi-Raymont, G., Bulbul, E., Dadina, M., Etori, S., Finoguenov, A., Fukazawa, Y., Janiuk, A., Kaastra, J., Mazzotta, P., Miller, J., Miniutti, G., Naze, Y., Nicastro, F., Scioritino, S., Simionescu, A., Torrejon, J. M., Frezouls, B., Geoffray, H., Peille, P., Aicardi, C., André, J., Daniel, C., Clénet, A., Etcheverry, C., Gloaguen, E., Hervet, G., Jolly, A., Ledot, A., Paillet, I., Schmisser, R., Vella, B., Damery, J.-C., Boyce, K., Dipirro, M., Lotti, S., Schwander, D., Smith, S., Van Leeuwen, B.-J., van Weers, H., Clerc, N., Cobo, B., Dauser, T., Kirsch, C., Cucchetti, E., Eckart, M., Ferrando, P. and Natalucci, L. (2018), The ATHENA X-ray Integral Field Unit (X-IFU), *in* J.-W. A. den Herder, S. Nikzad and K. Nakazawa, eds, ‘Space Telescopes and Instrumentation 2018: Ultraviolet to Gamma Ray’, Vol. 10699 of *Society of Photo-Optical Instrumentation Engineers (SPIE) Conference Series*, p. 106991G.
- Beckmann, V. and Shrader, C. (2013), *Active Galactic Nuclei*, Physics textbook, Wiley.
URL: <http://books.google.co.uk/books?id=QmwfxlZJM4sC>
- Bentz, M. C. and Katz, S. (2015), ‘The AGN Black Hole Mass Database’, *Publication of the Astronomical Society of the Pacific* **127**(947), 67.

- Bianchi, S., Guainazzi, M., Matt, G., Fonseca Bonilla, N. and Ponti, G. (2009), ‘CAIXA: a catalogue of AGN in the XMM-Newton archive. I. Spectral analysis’, *A & A* **495**(2), 421–430.
- Blustin, A. J., Page, M. J., Fuerst, S. V., Branduardi-Raymont, G. and Ashton, C. E. (2005), ‘The nature and origin of Seyfert warm absorbers’, *A & A* **431**, 111–125.
- Brandt, W. N., Fabian, A. C., Nandra, K., Reynolds, C. S. and Brinkmann, W. (1994), ‘ROSAT PSPC observations of the Seyfert 1 galaxies Ark 564, NGC 985, KAZ 163, MRK 79 and RX J2256.6+0525.’, *MNRAS* **271**, 958–966.
- Cappi, M. (2006), ‘Relativistic blue- and red-shifted absorption lines in AGNs’, *Astronomische Nachrichten* **327**, 1012.
- Cappi, M., De Marco, B., Ponti, G., Ursini, F., Petrucci, P. O., Bianchi, S., Kaastra, J. S., Kriss, G. A., Mehdipour, M., Whewell, M., Arav, N., Behar, E., Boissay, R., Branduardi-Raymont, G., Costantini, E., Ebrero, J., Di Gesu, L., Harrison, F. A., Kaspi, S., Matt, G., Paltani, S., Peterson, B. M., Steenbrugge, K. C. and Walton, D. J. (2016), ‘Anatomy of the AGN in NGC 5548. VIII. XMM-Newton’s EPIC detailed view of an unexpected variable multilayer absorber’, *A & A* **592**, A27.
- Cash, W. (1979), ‘Parameter estimation in astronomy through application of the likelihood ratio.’, *ApJ* **228**, 939–947.
- Chartas, G., Kochanek, C. S., Dai, X., Poindexter, S. and Garmire, G. (2009), ‘X-Ray Microlensing in RXJ1131-1231 and HE1104-1805’, *ApJ* **693**(1), 174–185.
- Dadina, M. (2008), ‘Seyfert galaxies in the local Universe ($z \leq 0.1$): the average X-ray spectrum as seen by BeppoSAX’, *A & A* **485**(2), 417–424.
- Dadina, M., Cappi, M., Malaguti, G., Ponti, G. and de Rosa, A. (2005), ‘X-ray absorption lines suggest matter infalling onto the central black-hole of Mrk 509’, *A & A* **442**, 461–468.
- De Marco, B., Adhikari, T. P., Ponti, G., Bianchi, S., Kriss, G. A., Arav, N., Behar, E., Branduardi-Raymont, G., Cappi, M., Costantini, E., Costanzo, D., di Gesu, L., Ebrero, J., Kaastra, J. S., Kaspi, S., Mao, J., Markowitz, A., Matt, G., Mehdipour, M., Middei, R., Paltani, S., Petrucci, P. O., Pinto, C., Róžańska, A. and Walton, D. J. (2020), ‘Incoherent fast variability of X-ray obscurers. The case of NGC 3783’, *A & A* **634**, A65.

BIBLIOGRAPHY

- De Marco, B., Iwasawa, K., Cappi, M., Dadina, M., Tombesi, F., Ponti, G., Celotti, A. and Miniutti, G. (2009), ‘Probing variability patterns of the Fe K line complex in bright nearby AGNs’, *A & A* **507**, 159–169.
- de Vaucouleurs, G. and de Vaucouleurs, A. (1975), ‘An improbable coincidence in NGC 985: a ring galaxy with a Seyfert nucleus.’, *ApJL* **197**, L1–L4.
- de Vaucouleurs, G., de Vaucouleurs, A., Corwin, Herold G., J., Buta, R. J., Paturel, G. and Fouque, P. (1991), *Third Reference Catalogue of Bright Galaxies*.
- Dehghanian, M., Ferland, G. J., Kriss, G. A., Peterson, B. M., Korista, K. T., Goad, M. R., Chatzikos, M., Guzmán, F., De Rosa, G., Mehdipour, M., Kaastra, J., Mathur, S., Vestergaard, M., Proga, D., Waters, T., Bentz, M. C., Bisogni, S., Brandt, W. N., Dalla Bontà, E., Fausnaugh, M. M., Gelbord, J. M., Horne, K., McHardy, I. M., Pogge, R. W. and Starkey, D. A. (2020), ‘Space Telescope and Optical Reverberation Mapping Project. XI. Disk-wind Characteristics and Contributions to the Very Broad Emission Lines of NGC 5548’, *ApJ* **898**(2), 141.
- Ebrero, J., Kriss, G. A., Kaastra, J. S. and Ely, J. C. (2016), ‘Discovery of a fast, broad, transient outflow in NGC 985’, *A & A* **586**, A72.
- Fabian, A. C., Iwasawa, K., Reynolds, C. S. and Young, A. J. (2000), ‘Broad Iron Lines in Active Galactic Nuclei’, *Publication of the Astronomical Society of the Pacific* **112**, 1145–1161.
- Fisher, K. B., Huchra, J. P., Strauss, M. A., Davis, M., Yahil, A. and Schlegel, D. (1995), ‘The IRAS 1.2 Jy Survey: Redshift Data’, *ApJS* **100**, 69.
- Fukumura, K., Tombesi, F., Kazanas, D., Shrader, C., Behar, E. and Contopoulos, I. (2015), ‘Magnetically Driven Accretion Disk Winds and Ultra-fast Outflows in PG 1211+143’, *ApJ* **805**(1), 17.
- Giustini, M. and Proga, D. (2019), ‘A global view of the inner accretion and ejection flow around super massive black holes. Radiation-driven accretion disk winds in a physical context’, *A & A* **630**, A94.
- Gofford, J., Reeves, J. N., Tombesi, F., Braitto, V., Turner, T. J., Miller, L. and Cappi, M. (2013), ‘The Suzaku view of highly ionized outflows in AGN - I. Statistical detection and global absorber properties’, *MNRAS* **430**(1), 60–80.
- Haardt, F. and Maraschi, L. (1991), ‘A two-phase model for the X-ray emission from Seyfert galaxies’, *ApJL* **380**, L51–L54.
- Haardt, F. and Maraschi, L. (1993), ‘X-ray spectra from two-phase accretion disks’, *ApJ* **413**, 507–517.

- Håring, N. and Rix, H.-W. (2004), ‘On the Black Hole Mass-Bulge Mass Relation’, *ApJL* **604**(2), L89–L92.
- Hopkins, P. F. and Elvis, M. (2010), ‘Quasar feedback: more bang for your buck’, *MNRAS* **401**(1), 7–14.
- Igo, Z., Parker, M. L., Matzeu, G. A., Alston, W., Alvarez Crespo, N., Fürst, F., Buisson, D. J. K., Lobban, A., Joyce, A. M., Mallick, L., Schartel, N. and Santos-Lleó, M. (2020), ‘Searching for ultra-fast outflows in AGN using variability spectra’, *MNRAS* **493**(1), 1088–1108.
- Iso, N., Ebisawa, K., Sameshima, H., Mizumoto, M., Miyakawa, T., Inoue, H. and Yamasaki, H. (2016), ‘Origin of the broad iron line feature and the soft X-ray variation in Seyfert galaxies’, *Publications of the Astronomical Society of Japan* **68**, S27.
- Iwasawa, K., Miniutti, G. and Fabian, A. C. (2004), ‘Flux and energy modulation of redshifted iron emission in NGC 3516: implications for the black hole mass’, *MNRAS* **355**, 1073–1079.
- Kaastra, J. S. and Bleeker, J. A. M. (2016), ‘Optimal binning of X-ray spectra and response matrix design’, *A & A* **587**, A151.
- Kaastra, J. S., Kriss, G. A., Cappi, M., Mehdipour, M., Petrucci, P. O., Steenbrugge, K. C., Arav, N., Behar, E., Bianchi, S., Boissay, R., Branduardi-Raymont, G., Chamberlain, C., Costantini, E., Ely, J. C., Ebrero, J., Di Gesu, L., Harrison, F. A., Kaspi, S., Malzac, J., De Marco, B., Matt, G., Nandra, K., Paltani, S., Person, R., Peterson, B. M., Pinto, C., Ponti, G., Nuñez, F. P., De Rosa, A., Seta, H., Ursini, F., de Vries, C. P., Walton, D. J. and Whewell, M. (2014), ‘A fast and long-lived outflow from the supermassive black hole in NGC 5548’, *Science* **345**(6192), 64–68.
- Kaastra, J. S., Mehdipour, M., Behar, E., Bianchi, S., Branduardi-Raymont, G., Brenneman, L., Cappi, M., Costantini, E., De Marco, B., di Gesu, L., Ebrero, J., Kriss, G. A., Mao, J., Peretz, U., Petrucci, P. O., Ponti, G. and Walton, D. (2018), ‘Recurring obscuration in NGC 3783’, *A & A* **619**, A112.
- Kaastra, J. S., Mewe, R., Liedahl, D. A., Komossa, S. and Brinkman, A. C. (2000), ‘X-ray absorption lines in the Seyfert 1 galaxy NGC 5548 discovered with Chandra-LETGS’, *A & A* **354**, L83–L86.
- Kallman, T. R., Palmeri, P., Bautista, M. A., Mendoza, C. and Krolik, J. H. (2004), ‘Photoionization Modeling and the K Lines of Iron’, *ApJS* **155**(2), 675–701.

BIBLIOGRAPHY

- Kara, E., Alston, W. N., Fabian, A. C., Cackett, E. M., Uttley, P., Reynolds, C. S. and Zoghbi, A. (2016), ‘A global look at X-ray time lags in Seyfert galaxies’, *MNRAS* **462**(1), 511–531.
- King, A. and Pounds, K. (2015), ‘Powerful Outflows and Feedback from Active Galactic Nuclei’, *ARAA* **53**, 115–154.
- Kormendy, J. and Ho, L. C. (2013), ‘Coevolution (Or Not) of Supermassive Black Holes and Host Galaxies’, *ARAA* **51**(1), 511–653.
- Krolik, J. H. and Kriss, G. A. (2001), ‘Warm Absorbers in Active Galactic Nuclei: A Multitemperature Wind’, *ApJ* **561**(2), 684–690.
- Krongold, Y., Jiménez-Bailón, E., Santos-Lleo, M., Nicastro, F., Elvis, M., Brickhouse, N., Andrade-Velazquez, M., Binette, L. and Mathur, S. (2009), ‘XMM-Newton View of the Multiphase Warm Absorber in Seyfert 1 Galaxy NGC 985’, *ApJ* **690**(1), 773–782.
- Krongold, Y., Nicastro, F., Elvis, M., Brickhouse, N. S., Mathur, S. and Zezas, A. (2005), ‘The Ionized Nuclear Environment in NGC 985 as seen by Chandra and BeppoSAX’, *ApJ* **620**(1), 165–182.
- Laha, S., Guainazzi, M., Dewangan, G. C., Chakravorty, S. and Kembhavi, A. K. (2014), ‘Warm absorbers in X-rays (WAX), a comprehensive high-resolution grating spectral study of a sample of Seyfert galaxies - I. A global view and frequency of occurrence of warm absorbers.’, *MNRAS* **441**(3), 2613–2643.
- Lamer, G., Uttley, P. and McHardy, I. M. (2003), ‘An absorption event in the X-ray light curve of NGC 3227’, *MNRAS* **342**(3), L41–L45.
- Laor, A. (1991), ‘Line Profiles from a Disk around a Rotating Black Hole’, *ApJ* **376**, 90.
- Lobban, A. P., Turner, T. J., Reeves, J. N., Braito, V. and Miller, L. (2020), ‘X-ray variability analysis of a large series of XMM-Newton +NuSTAR observations of NGC 3227’, *MNRAS* **494**(4), 5056–5074.
- Mao, J., Mehdipour, M., Kaastra, J. S., Costantini, E., Pinto, C., Branduardi-Raymont, G., Behar, E., Peretz, U., Bianchi, S., Kriss, G. A., Ponti, G., De Marco, B., Petrucci, P. O., Di Gesu, L., Middei, R., Ebrero, J. and Arav, N. (2019), ‘Photoionized emission and absorption features in the high-resolution X-ray spectra of NGC 3783’, *A & A* **621**, A99.

- Marinucci, A., Bianchi, S., Braitto, V., De Marco, B., Matt, G., Middei, R., Nardini, E. and Reeves, J. N. (2020), ‘The lively accretion disc in NGC 2992 - I. Transient iron K emission lines in the high-flux state’, *MNRAS* **496**(3), 3412–3423.
- Markowitz, A. G., Krumpe, M. and Nikutta, R. (2014), ‘First X-ray-based statistical tests for clumpy-torus models: eclipse events from 230 years of monitoring of Seyfert AGN’, *MNRAS* **439**(2), 1403–1458.
- Mehdipour, M., Kaastra, J. S., Kriss, G. A., Arav, N., Behar, E., Bianchi, S., Branduardi-Raymont, G., Cappi, M., Costantini, E., Ebrero, J., Di Gesu, L., Kaspi, S., Mao, J., De Marco, B., Matt, G., Paltani, S., Peretz, U., Peterson, B. M., Petrucci, P.-O., Pinto, C., Ponti, G., Ursini, F., de Vries, C. P. and Walton, D. J. (2017), ‘Chasing obscuration in type-I AGN: discovery of an eclipsing clumpy wind at the outer broad-line region of NGC 3783’, *A & A* **607**, A28.
- Mehdipour, M., Kaastra, J. S., Kriss, G. A., Cappi, M., Petrucci, P. O., Steenbrugge, K. C., Arav, N., Behar, E., Bianchi, S., Boissay, R., Branduardi-Raymont, G., Costantini, E., Ebrero, J., Di Gesu, L., Harrison, F. A., Kaspi, S., De Marco, B., Matt, G., Paltani, S., Peterson, B. M., Ponti, G., Pozo Nuñez, F., De Rosa, A., Ursini, F., de Vries, C. P., Walton, D. J. and Whewell, M. (2015), ‘Anatomy of the AGN in NGC 5548. I. A global model for the broadband spectral energy distribution’, *A & A* **575**, A22.
- Mehdipour, M., Kriss, G. A., Kaastra, J. S., Wang, Y., Mao, J., Costantini, E., Arav, N., Behar, E., Bianchi, S., Branduardi-Raymont, G., Brotherton, M., Cappi, M., De Marco, B., Di Gesu, L., Ebrero, J., Grafton-Waters, S., Kaspi, S., Matt, G., Paltani, S., Petrucci, P. O., Pinto, C., Ponti, G., Ursini, F. and Walton, D. J. (2021), ‘Transient obscuration event captured in NGC 3227. I. Continuum model for the broadband spectral energy distribution’, *A & A* **652**, A150.
- Miniutti, G. and Fabian, A. C. (2004), ‘A light bending model for the X-ray temporal and spectral properties of accreting black holes’, *MNRAS* **349**(4), 1435–1448.
- Molendi, S., Bianchi, S. and Matt, G. (2003), ‘Iron and nickel line properties in the X-ray-reflecting region of the Circinus galaxy’, *MNRAS* **343**(1), L1–L4.
- Mushotzky, R. F., Done, C. and Pounds, K. A. (1993), ‘X-ray spectra and time variability of active galactic nuclei’, *ARAA* **31**, 717–761.
- Nandra, K., Barret, D., Barcons, X., Fabian, A., den Herder, J.-W., Piro, L., Watson, M., Adami, C., Aird, J., Afonso, J. M., Alexander, D., Argiroffi, C., Amati, L., Arnaud, M., Atteia, J.-L., Audard, M., Badenes, C., Ballet, J., Ballo,

BIBLIOGRAPHY

L., Bamba, A., Bhardwaj, A., Stefano Battistelli, E., Becker, W., De Becker, M., Behar, E., Bianchi, S., Biffi, V., Bîrzan, L., Bocchino, F., Bogdanov, S., Boirin, L., Boller, T., Borgani, S., Borm, K., Bouché, N., Bourdin, H., Bower, R., Braitto, V., Branchini, E., Branduardi-Raymont, G., Bregman, J., Brenneman, L., Brightman, M., Brüggen, M., Buchner, J., Bulbul, E., Brusa, M., Bursa, M., Caccianiga, A., Cackett, E., Campana, S., Cappelluti, N., Cappi, M., Carrera, F., Ceballos, M., Christensen, F., Chu, Y.-H., Churazov, E., Clerc, N., Corbel, S., Corral, A., Comastri, A., Costantini, E., Croston, J., Dadina, M., D’Ai, A., Decourchelle, A., Della Ceca, R., Dennerl, K., Dolag, K., Done, C., Dovciak, M., Drake, J., Eckert, D., Edge, A., Ettori, S., Ezoe, Y., Feigelson, E., Fender, R., Feruglio, C., Finoguenov, A., Fiore, F., Galeazzi, M., Gallagher, S., Gandhi, P., Gaspari, M., Gastaldello, F., Georgakakis, A., Georgantopoulos, I., Gilfanov, M., Gitti, M., Gladstone, R., Goosmann, R., Gosset, E., Grosso, N., Guedel, M., Guerrero, M., Haberl, F., Hardcastle, M., Heinz, S., Alonso Herrero, A., Hervé, A., Holmstrom, M., Iwasawa, K., Jonker, P., Kaastra, J., Kara, E., Karas, V., Kastner, J., King, A., Kosenko, D., Koutroumpa, D., Kraft, R., Kreykenbohm, I., Lallement, R., Lanzuisi, G., Lee, J., Lemoine-Goumard, M., Lobban, A., Lodato, G., Lovisari, L., Lotti, S., McCharthy, I., McNamara, B., Maggio, A., Maiolino, R., De Marco, B., de Martino, D., Mateos, S., Matt, G., Maughan, B., Mazzotta, P., Mendez, M., Merloni, A., Micela, G., Miceli, M., Mignani, R., Miller, J., Miniutti, G., Molendi, S., Montez, R., Moretti, A., Motch, C., Nazé, Y., Nevalainen, J., Nicastro, F., Nulsen, P., Ohashi, T., O’Brien, P., Osborne, J., Oskinova, L., Pacaud, F., Paerels, F., Page, M., Papadakis, I., Pareschi, G., Petre, R., Petrucci, P.-O., Piconcelli, E., Pillitteri, I., Pinto, C., de Plaa, J., Pointecouteau, E., Ponman, T., Ponti, G., Porquet, D., Pounds, K., Pratt, G., Predehl, P., Proga, D., Psaltis, D., Rafferty, D., Ramos-Ceja, M., Ranalli, P., Rasia, E., Rau, A., Rauw, G., Rea, N., Read, A., Reeves, J., Reiprich, T., Renaud, M., Reynolds, C., Risaliti, G., Rodriguez, J., Rodriguez Hidalgo, P., Roncarelli, M., Rosario, D., Rossetti, M., Rozanska, A., Rovilos, E., Salvaterra, R., Salvato, M., Di Salvo, T., Sanders, J., Sanz-Forcada, J., Schawinski, K., Schaye, J., Schwobe, A., Sciortino, S., Severgnini, P., Shankar, F., Sijacki, D., Sim, S., Schmid, C., Smith, R., Steiner, A., Stelzer, B., Stewart, G., Strohmayer, T., Strüder, L., Sun, M., Takei, Y., Tatischeff, V., Tiengo, A., Tombesi, F., Trinchieri, G., Tsuru, T. G., Ud-Doula, A., Ursino, E., Valencic, L., Vanzella, E., Vaughan, S., Vignali, C., Vink, J., Vito, F., Volonteri, M., Wang, D., Webb, N., Willingale, R., Wilms, J., Wise, M., Worrall, D., Young, A., Zampieri, L., In’t Zand, J., Zane, S., Zezas, A., Zhang, Y. and Zhuravleva, I. (2013), ‘The Hot and Energetic Universe: A White Paper presenting the science theme motivating the Athena+ mission’, *arXiv e-prints* p. arXiv:1306.2307.

Nardini, E., Porquet, D., Reeves, J. N., Braitto, V., Lobban, A. and Matt, G.

- (2016), ‘A Deep X-Ray View of the Bare AGN Ark 120. II. Evidence for Fe K Emission Transients’, *The Astrophysical Journal* **832**(1), 45.
- Netzer, H. (2015), ‘Revisiting the Unified Model of Active Galactic Nuclei’, *ARAAS* **53**, 365–408.
- Nicastro, F., Fiore, F., Brandt, N. and Reynolds, C. S. (1999), ‘A resonant absorption line in the ASCA spectrum of NGC 985?’, *Nuclear Physics B Proceedings Supplements* **69**(1-3), 501–504.
- Padovani, P., Alexander, D. M., Assef, R. J., De Marco, B., Giommi, P., Hickox, R. C., Richards, G. T., Smolčić, V., Hatziminaoglou, E., Mainieri, V. and Salvato, M. (2017), ‘Active galactic nuclei: what’s in a name?’, *The Astronomy and Astrophysics Review* **25**, 2.
- Pancoast, A., Brewer, B. J., Treu, T., Park, D., Barth, A. J., Bentz, M. C. and Woo, J.-H. (2014), ‘Modelling reverberation mapping data - II. Dynamical modelling of the Lick AGN Monitoring Project 2008 data set’, *MNRAS* **445**(3), 3073–3091.
- Parker, M. L., Schartel, N., Komossa, S., Grupe, D., Santos-Lleó, M., Fabian, A. C. and Mathur, S. (2014), ‘A partial eclipse of the heart: the absorbed X-ray low state in Mrk 1048’, *MNRAS* **445**(1), 1039–1047.
- Peterson, B. (1997), *An Introduction to Active Galactic Nuclei*, Cambridge University Press.
- Peterson, B. M., Ferrarese, L., Gilbert, K. M., Kaspi, S., Malkan, M. A., Maoz, D., Merritt, D., Netzer, H., Onken, C. A., Pogge, R. W., Vestergaard, M. and Wandel, A. (2004), ‘Central Masses and Broad-Line Region Sizes of Active Galactic Nuclei. II. A Homogeneous Analysis of a Large Reverberation-Mapping Database’, *ApJ* **613**, 682–699.
- Petrucci, P. O., Ursini, F., De Rosa, A., Bianchi, S., Cappi, M., Matt, G., Dadina, M. and Malzac, J. (2018), ‘Testing warm Comptonization models for the origin of the soft X-ray excess in AGNs’, *A & A* **611**, A59.
- Ponti, G., Cappi, M., Costantini, E., Bianchi, S., Kaastra, J. S., De Marco, B., Fender, R. P., Petrucci, P. O., Kriss, G. A., Steenbrugge, K. C., Arav, N., Behar, E., Branduardi-Raymont, G., Dadina, M., Ebrero, J., Lubiński, P., Mehdipour, M., Paltani, S., Pinto, C. and Tombesi, F. (2013), ‘Multiwavelength campaign on Mrk 509. XI. Reverberation of the Fe K α line’, *A & A* **549**, A72.

BIBLIOGRAPHY

- Proga, D. (2007), Theory of Winds in AGNs, *in* L. C. Ho and J. W. Wang, eds, ‘The Central Engine of Active Galactic Nuclei’, Vol. 373 of *Astronomical Society of the Pacific Conference Series*, p. 267.
- Protassov, R., van Dyk, D. A., Connors, A., Kashyap, V. L. and Siemiginowska, A. (2002), ‘Statistics, Handle with Care: Detecting Multiple Model Components with the Likelihood Ratio Test’, *ApJ* **571**(1), 545–559.
- Ptak, A., Yaqoob, T., Serlemitsos, P. J., Mushotzky, R. and Otani, C. (1994), ‘Rapid X-Ray Spectral Variability in NGC 3227’, *ApJL* **436**, L31.
- Reeves, J. N., Nandra, K., George, I. M., Pounds, K. A., Turner, T. J. and Yaqoob, T. (2004), ‘The XMM-Newton Iron Line Profile of NGC 3783’, *ApJ* **602**, 648–658.
- Reynolds, C. S. (1997), ‘An X-ray spectral study of 24 type 1 active galactic nuclei’, *MNRAS* **286**(3), 513–537.
- Risaliti, G., Miniutti, G., Elvis, M., Fabbiano, G., Salvati, M., Baldi, A., Braito, V., Bianchi, S., Matt, G., Reeves, J., Soria, R. and Zezas, A. (2009), ‘Variable Partial Covering and A Relativistic Iron Line in NGC 1365’, *ApJ* **696**(1), 160–171.
- Serafinelli, R., Tombesi, F., Vagnetti, F., Piconcelli, E., Gaspari, M. and Saturni, F. G. (2019), ‘Multiphase quasar-driven outflows in PG 1114+445. I. Entrained ultra-fast outflows’, *A & A* **627**, A121.
- Seyfert, C. K. (1943), ‘Nuclear Emission in Spiral Nebulae.’, *ApJ* **97**, 28.
- Shakura, N. I. and Sunyaev, R. A. (1973), ‘Reprint of 1973A&A....24..337S. Black holes in binary systems. Observational appearance.’, *A & A* **500**, 33–51.
- Smith, R. and Arcus Collaboration (2018), Arcus: An Overview of the Soft X-ray Grating Explorer, *in* ‘American Astronomical Society Meeting Abstracts #231’, Vol. 231 of *American Astronomical Society Meeting Abstracts*, p. 237.18.
- Snowden, S., Valencic, L., Perry, B., Arida, M. and Kuntz, K. D. (2004), ‘The XMM-Newton ABC Guide: An Introduction to XMM-Newton Data Analysis’, The XMM-Newton ABC Guide: An Introduction to XMM-Newton Data Analysis. With contributions by: Ilana Harrus.
- Tennant, A. F. and Mushotzky, R. F. (1983), ‘The absence of rapid X-ray variability in active galaxies.’, *ApJ* **264**, 92–104.

- Theureau, G., Bottinelli, L., Coudreau-Durand, N., Gouguenheim, L., Hallet, N., Loulergue, M., Paturel, G. and Teerikorpi, P. (1998), ‘Kinematics of the local universe. VII. New 21-cm line measurements of 2112 galaxies’, *AAPS* **130**, 333–339.
- Tombesi, F., Cappi, M., Reeves, J. N., Nemmen, R. S., Braitto, V., Gaspari, M. and Reynolds, C. S. (2013), ‘Unification of X-ray winds in Seyfert galaxies: from ultra-fast outflows to warm absorbers’, *MNRAS* **430**(2), 1102–1117.
- Tombesi, F., Cappi, M., Reeves, J. N., Palumbo, G. G. C., Yaqoob, T., Braitto, V. and Dadina, M. (2010), ‘Evidence for ultra-fast outflows in radio-quiet AGNs. I. Detection and statistical incidence of Fe K-shell absorption lines’, *A & A* **521**, A57.
- Tombesi, F., de Marco, B., Iwasawa, K., Cappi, M., Dadina, M., Ponti, G., Miniutti, G. and Palumbo, G. G. C. (2007), ‘Correlated modulation between the redshifted Fe K α line and the continuum emission in NGC 3783’, *A & A* **467**, 1057–1063.
- Turner, T. J., Miller, L., George, I. M. and Reeves, J. N. (2006), ‘Evidence for orbital motion of material close to the central black hole of Mrk 766’, *A & A* **445**, 59–67.
- Turner, T. J. and Pounds, K. A. (1989), ‘The EXOSAT spectral survey of AGN.’, *MNRAS* **240**, 833–880.
- Turner, T. J., Reeves, J. N., Braitto, V., Lobban, A., Kraemer, S. and Miller, L. (2018), ‘A rapid occultation event in NGC 3227’, *MNRAS* **481**(2), 2470–2478.
- Uttley, P. and McHardy, I. M. (2005), ‘X-ray variability of NGC 3227 and 5506 and the nature of active galactic nucleus ‘states’’, *MNRAS* **363**(2), 586–596.
- Vasudevan, R. V., Fabian, A. C., Gandhi, P., Winter, L. M. and Mushotzky, R. F. (2010), ‘The power output of local obscured and unobscured AGN: crossing the absorption barrier with Swift/BAT and IRAS’, *MNRAS* **402**(2), 1081–1098.
- Vasudevan, R. V., Mushotzky, R. F., Winter, L. M. and Fabian, A. C. (2009), ‘Optical-to-X-ray emission in low-absorption AGN: results from the Swift-BAT 9-month catalogue’, *MNRAS* **399**(3), 1553–1575.
- Vaughan, S. and Uttley, P. (2008), ‘On the evidence for narrow, relativistically shifted X-ray lines’, *MNRAS* **390**(1), 421–428.

BIBLIOGRAPHY

- Wang, Y., Kaastra, J., Mehdipour, M., Mao, J., Costantini, E., Kriss, G. A., Pinto, C., Ponti, G., Behar, E., Bianchi, S., Branduardi-Raymont, G., De Marco, B., Grafton-Waters, S., Petrucci, P.-O., Ebrero, J., Walton, D. J., Kaspi, S., Xue, Y., Paltani, S., di Gesu, L. and He, Z. (2022), ‘Transient obscuration event captured in NGC 3227. II. Warm absorbers and obscuration events in archival XMM-Newton and NuSTAR observations’, *A & A* **657**, A77.
- Webb, N. A., Coriat, M., Traulsen, I., Ballet, J., Motch, C., Carrera, F. J., Koliopanos, F., Authier, J., de la Calle, I., Ceballos, M. T., Colomo, E., Chuard, D., Freyberg, M., Garcia, T., Kolehmainen, M., Lamer, G., Lin, D., Maggi, P., Michel, L., Page, C. G., Page, M. J., Perea-Calderon, J. V., Pineau, F. X., Rodriguez, P., Rosen, S. R., Santos Lleo, M., Saxton, R. D., Schwope, A., Tomás, L., Watson, M. G. and Zakardjian, A. (2020), ‘The XMM-Newton serendipitous survey. IX. The fourth XMM-Newton serendipitous source catalogue’, *A & A* **641**, A136.
- Wenger, M., Ochsenbein, F., Egret, D., Dubois, P., Bonnarel, F., Borde, S., Genova, F., Jasniewicz, G., Laloë, S., Lesteven, S. and Monier, R. (2000), ‘The SIMBAD astronomical database. The CDS reference database for astronomical objects’, *AAPS* **143**, 9–22.
- XRISM Science Team (2020), ‘Science with the X-ray Imaging and Spectroscopy Mission (XRISM)’, *arXiv e-prints* p. arXiv:2003.04962.
- Yaqoob, T., Reeves, J. N., Markowitz, A., Serlemitsos, P. J. and Padmanabhan, U. (2005), ‘Chandra High-Resolution X-Ray Spectroscopy of the Fe K Line in the Seyfert 1 Galaxy NGC 3783’, *ApJ* **627**(1), 156–165.
- Zoghbi, A., Miller, J. M. and Cackett, E. (2019), ‘Revisiting the Spectral and Timing Properties of NGC 4151’, *ApJ* **884**(1), 26.